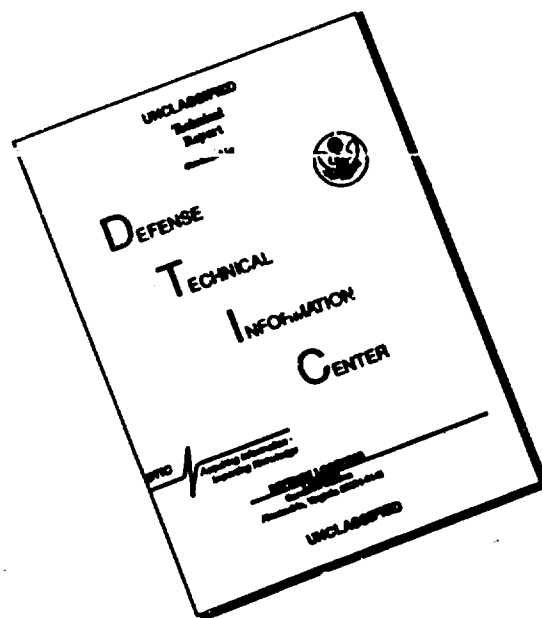


DISCLAIMER NOTICE



THIS DOCUMENT IS BEST QUALITY AVAILABLE. THE COPY FURNISHED TO DTIC CONTAINED A SIGNIFICANT NUMBER OF PAGES WHICH DO NOT REPRODUCE LEGIBLY.

THREE-DIMENSIONAL TURBULENT BOUNDARY LAYERS

By

O. Sendstad and P. Moin

Prepared with the support of the
Air Force Office of Scientific Research
under Grants 87-0285 and 91-0174

DTIC QUALITY INSPECTED B

Report No. TF-57

Thermosciences Division
Department of Mechanical Engineering
Stanford University
Stanford, California 94305

December 1992

Accession For	
NTIS CRA&I	<input checked="" type="checkbox"/>
DTIC TAB	<input type="checkbox"/>
Unannounced	<input type="checkbox"/>
Justification	
By _____	
Distribution/ _____	
Availability Codes	
Dist	Avail and/or Special
A-1	

93 6 28 00 1

93-14809



ABSTRACT

The near wall mechanics of three-dimensional turbulent boundary layers were studied using direct numerical simulation. A fully developed turbulent channel flow was suddenly subjected to a transverse pressure gradient. An explanation for the reduction in the Reynolds stresses, observed in experiments, was provided in terms of the dynamics of near wall streamwise vortices. A mechanism for the generation of near-wall streamwise vortices in turbulent boundary layers was described. It was shown that the effect of three-dimensionality is to change the trajectory of fluid particles in the vicinity of these vortices, and how this change leads to reductions of turbulence stresses. The proposed mechanisms are consistent with numerous statistical data and correlations which are presented.

ACKNOWLEDGEMENTS

This work was supported by the United States Air Force Office of Scientific Research under Grants 87-0285 and 91-0174, with Dr. James McMichael as the technical monitor. Computer time was provided by NASA-Ames Research Center. We are grateful to Professor Javier Jimenez for numerous stimulating discussions, and to Professors Peter Bradshaw and John Eaton for useful discussions and helpful comments on a draft of this report.

CONTENTS

	<i>Page</i>
Abstract	iv
Acknowledgments	v
Contents	vi
Nomenclature	viii
 <i>Chapter</i>	
1 Introduction	1
1.1 Motivation	1
1.2 Objectives	2
1.3 Approach	2
1.4 Three-dimensional turbulent boundary layers	3
1.4.1 Definition	3
1.4.2 Mechanisms for generation of 3D TBLs	3
1.4.3 Review of previous results	5
1.4.4 Structural "theories" for the observed 3D effects	11
2 Numerical and analytical considerations	15
2.1 Geometry and coordinates	15
2.2 Numerical method	16
2.3 Parameters and grid	16
2.4 The minimal flow unit	17
2.5 Preliminary considerations for the 3D turbulent channel flow	18
2.6 3D channel flow vs 3D boundary layers	20
2.7 Methods of identifying the mechanics underlying the 3D effects	21
3 Near-wall turbulence structures in 2D boundary layers	25
3.1 Quasi-streamwise vortices	25
3.1.1 Average size and location	26
3.1.2 Detection of vortices	26
3.1.3 Dynamics of quasi-streamwise vortices in TBLs	27
3.2 High- and low-speed streaks	28
3.3 Near-wall shear layers	30
4 Results and discussions	43
4.1 Reynolds stresses during the initial period	44
4.1.1 Probability density functions, octant- and quadrant analysis	45
4.2.2 The companion flows method	47
4.2 Reynolds stresses during the later period of three-dimensionality	50
4.2.1 Changes in the Reynolds stresses	50
4.2.2 Identification of the most affected events in the late period	51
4.2.3 Underlying mechanisms in the late period	53
4.3 Mean velocities	55

<i>Chapter</i>	<i>Page</i>
4.4 Vorticity intensities	56
4.5 Two-point correlations and energy spectra	57
4.6 Comparison with previously suggested mechanisms	58
5 Conclusions	113
References	115

NOMENCLATURE

Roman Symbols

a_1	$\sqrt{\overline{u'v'^2} + \overline{v'w'^2}} / (\overline{u'^2} + \overline{v'^2} + \overline{w'^2})$ (structure parameter).
f_z	z -component external forces.
k_x, k_z	Components of wave vector.
l	shift of the structures in the spanwise direction.
L_x, L_y, L_z	Dimensions of the computational domain in the x , y and z direction.
N_x, N_y, N_z	Number of grid-points in the x , y and z direction.
p, P	Pressure and averaged pressure.
Re	Reynolds number. $Re = \frac{u_{\tau 2D} \delta}{\nu}$.
Re_L	Reynolds number. $Re_L = \frac{U_L \delta}{\nu}$.
R_{ij}	Two-point velocity correlation tensor.
t	Time.
t^+	$t\nu / u_{\tau 2D}^2$.
u_{τ}	Wall shear velocity $\sqrt{\nu \frac{\partial U}{\partial y} / \rho}$.
$\tilde{u}(x, z)$	$u(x, z + l)$.
u_1, u_2, u_3	u, v, w .
$u_{\tau 2D}$	Wall shear velocity in 2D.
u, v, w	Velocity components in the x -, y - and z -direction.
U_1, U_2, U_3	U, V, W .
U_{∞}	Free-stream mean velocity in x -direction.
U_L	Centerline velocity of the laminar flow with the same mass flux.
U, V, W	Mean velocity components in the x -, y - and z -direction.
w_y, W_y	$\frac{\partial w}{\partial y}$ and $\frac{\partial W}{\partial y}$.
w_{∞}	w in the free-stream.
\hat{w}	$w - w_{\infty}$.
W_s	Wall motion in the z -direction.
W_{∞}	Free-stream mean velocity in z -direction.
x	Axis in the initial mean flow direction.

y	Axis normal to the wall.
y^+	$u_{\tau}y/\nu$.
y_{zD}^+	$u_{\tau zD}y/\nu$.
z	Axis normal to x and y .
\hat{z}	$z + \frac{1}{2} \frac{\partial P}{\partial z} t^2$.

Greek Symbols

α	$\tan(\theta_R)$.
γ_i	Angle of maximum streamwise intensity, see eqn. 2.1d.
γ_g	Mean velocity gradient angle, see eqn. 2.1c.
γ_s	Mean velocity angle, see eqn. 2.1a.
γ_{τ}	Reynolds shear stress angle, see eqn. 2.1b.
ν	Kinematic viscosity.
∇^2	$\frac{\partial^2}{\partial x^2} + \frac{\partial^2}{\partial y^2} + \frac{\partial^2}{\partial z^2}$.
δ	Channel half width.
$\omega_x, \omega_y, \omega_z$	vorticity components in the x -, y - and z -direction.
Ω_x	Mean ω_x .
θ_R	Angle of maximum auto-correlation.
$\delta x, \delta y, \delta z$	Grid dimensions.

Special Symbols

$()_*$	quantity in rotated coordinates.
$\overline{()}$	ensemble-averaged quantity.
$()'$	fluctuating quantity.

CHAPTER 1

INTRODUCTION

1.1 Motivation

Turbulent boundary layers (TBLs) of practical interest often have a three-dimensional (3D) mean velocity profile. This is usually the case when the geometry is complex, but there are also many important simple geometries with a 3D TBL. Examples of the latter are the flow over a swept wing and the cooling of a vertical wall by a non-vertical flow along the wall. The number of detailed experiments on 3D TBLs is still far lower than in two dimensional (2D) boundary layers, in part because of the difficulties in predicting 2D turbulent flows, which are presumed to be simpler. Despite the dearth of experimental results several common features of 3D TBLs, some unexpected, are reported in several experiments (see the reviews by Johnston 1976, Cebeci, 1984). These features are outlined below:

First, the eddy-viscosity differs for the streamwise and the spanwise component of the Reynolds shear stress, which undermines the use of models based on a scalar eddy viscosity. Second, when a 2D TBL is turned into a 3D TBL by action of, say, a transverse pressure gradient, the total Reynolds shear stress, $\sqrt{\overline{u'v'}^2 + \overline{v'w'}^2}$, is lower than in a 2D TBL with a similar streamwise pressure gradient. This is counter-intuitive because the addition of a spanwise mean velocity gradient will generate spanwise shear stress, $-\overline{v'w'}$. Finally, there is usually a drop in the ratio of the total Reynolds shear stress to twice the turbulent kinetic energy, called the structure parameter a_1 . This quantity has a near-constant value of about 0.15 in the outer part of many 2D TBLs and has therefore been used in turbulence modelling.

The present turbulence models have difficulty predicting 3D TBLs; features such as the reduction in the Reynolds shear stress are not predicted. Therefore, an improved understanding of these phenomena would be very useful in the development of better models. Since a_1 and the total Reynolds shear stress are invariant with respect to a coordinate rotation in the plane of the wall, the reduction must be due to changes in the structure of the turbulence rather than simple rotation of the stress tensor.

In the near-wall region of TBLs, well known contributors to the Reynolds shear stress and turbulent kinetic energy are the quasi-streamwise vortices, pumping high-speed fluid toward the wall and low-speed fluid away from the wall (Moin, 1987, Robinson, 1991). It is therefore believed that this process may have been altered in 3D flows, and the mechanism of this alteration can be found through a study of the turbulence structures in 3D TBLs. Such a study may also contribute to increased understanding of the role of these structures in 2D TBLs as well.

1.2 Objectives

The objective of this study is to examine the mechanics underlying the observed 3D phenomena described above, using direct numerical simulation. Turbulence statistics will be accumulated in order to see how they are affected by the three-dimensionality. Then, the effects of three-dimensionality on the turbulence structures will be examined to understand the mechanisms leading to the observed changes in the turbulence statistics.

The advantage of direct numerical simulation is that all essential scales are resolved so that modelling is not necessary. It is possible to study the unsteady three-dimensional turbulence structures directly, as well as using conditional averaging and other techniques.

1.3 Approach

The computed flow that is the subject of this study is a 2D fully developed, pressure-driven, turbulent channel flow which is turned by a suddenly imposed spanwise pressure gradient. A schematic of the channel with the coordinate system is shown in Figure 1.1. The x - and z -axes are in the directions of the initial mean flow and the initial spanwise direction respectively, and the y -axis is perpendicular to the walls. In this flow all effects due to three-dimensionality will grow outward from the wall. It therefore differs from spatially developing TBLs, such as that on a swept wing, where three-dimensionality is generated in the outer part as well (see §1.4.2). This work is therefore a study of the effects of three-dimensionality on the near-wall turbulence. Although the presently simulated flow is a channel flow, the results are relevant to turbulent boundary layers because the near-wall features of both flows are known to be nearly identical.

1.4 Three-dimensional turbulent boundary layers

1.4.1 Definition

A turbulent boundary layer is three-dimensional when, in coordinates fixed to the wall, the directions of the projections of the mean velocity vectors onto planes parallel to the wall vary with the distance from the wall. It follows that in 3D TBLs the velocity gradient angle, $\gamma_y \equiv \tan^{-1}(\frac{\partial W}{\partial y} / \frac{\partial U}{\partial y})$, varies with the distance from the wall. U and W are the streamwise and spanwise mean velocity components in planes parallel to the wall. The maximum change in the velocity gradient angle across the TBL can be used as an indicator of the degree of three-dimensionality and is invariant with respect to coordinate rotation in the plane parallel to the wall. Note that the mean velocity profiles in the streamwise and the spanwise directions can have different thickness; this is the case for the present channel flow.

1.4.2 Mechanisms for generation of 3D TBLs

Since the mean velocity gradient angle is non-zero in 3D TBLs, the governing equation for $\frac{\partial W}{\partial y}$ can be used to identify the different conditions that lead to three-dimensionality. When the boundary layer approximations apply, $\Omega_x \approx \frac{\partial W}{\partial y}$ and the better known transport equation for the mean streamwise vorticity can be used instead (Bradshaw, 1987). We have chosen not to make this approximation. Differentiating the Navier Stokes equation for W results in,

$$\frac{DW_y}{Dt} = \frac{\partial U}{\partial x} W_y + \nu \nabla^2 W_y - \frac{1}{\rho} \frac{\partial^2 P}{\partial y \partial z} - \frac{\partial W}{\partial x} \frac{\partial U}{\partial y} - \frac{\partial^2 \overline{u'w'}}{\partial y \partial x} - \frac{\partial^2 \overline{v'w'}}{\partial y^2} - \frac{\partial^2 \overline{w'^2}}{\partial y \partial z} + \frac{\partial f_z}{\partial y} \quad (1.4.1)$$

where $W_y \equiv \frac{\partial W}{\partial y}$, x and z are the coordinates in planes parallel to the wall, y is normal to the wall, and f_z is the z -component of the external forces. (U, V, W) and (u', v', w') are the mean and fluctuating velocities in the (x, y, z) directions respectively. The normal derivative of W_y at the wall is given by the Navier Stokes equation for W ,

$$\frac{\partial W_y}{\partial y} = \frac{1}{\nu} \left[\frac{1}{\rho} \frac{\partial P}{\partial z} + \frac{DW}{Dt} - f_z \right] - \frac{\partial^2 W}{\partial x^2} - \frac{\partial^2 W}{\partial z^2}. \quad (1.4.2)$$

A term-by-term study identifies the following sources for three-dimensionality :

- 1) A spanwise pressure gradient, $\frac{\partial P}{\partial z}$, will generate a continuous flux of W_y at the wall, causing three-dimensionality to grow outward from the wall. $\frac{\partial P}{\partial z}$ can also

generate three-dimensionality inside the flow directly, which will make the entire TBL three-dimensional much faster. This occurs when the spanwise pressure gradient varies in x , which would generate $\frac{\partial W_\infty}{\partial x}$. The term $\frac{\partial W}{\partial x} \frac{\partial U}{\partial y}$ in eqn. (1.4.1) will then be non-zero across the TBL. This effect is often called "inviscid skewing" since it corresponds to a generation of mean streamwise vorticity by skewing the mean spanwise vorticity, Ω_z , through the tilting term $\Omega_z \frac{\partial U}{\partial z}$. For steady flows, the ensuing spanwise mean velocity gradient angle is often well approximated with the Squire-Winter-Hawthorne equation, $\frac{\partial}{\partial x} \left(\frac{\partial W / \partial y}{\partial U / \partial y} \right) = - \frac{\partial}{\partial x} \left(\frac{W}{U} \right)$, where U is the mean velocity in the streamwise direction and W is the corresponding spanwise component. This is a linearized approximation for low turning angles, but experiments have shown that it is often valid for larger angles as well. The resulting Johnston- or hodograph-plot, where W is plotted against U in coordinates aligned with the local free-stream direction, will then be almost triangular in shape. The term $\frac{\partial^2 P}{\partial y \partial z}$ is negligible for thin TBLs, but may play a role when the TBL is thick.

- 2) If the flow encounters a wall moving in a direction different from the local mean velocity gradient direction, three-dimensionality is generated at the wall and will grow outward. These flows are called shear-driven 3D TBLs. In the case of a constant wall velocity, the only sources of W_y are the horizontal viscous forces between the moving and the non-moving part of the wall (last two terms in eqn. (1.4.2)). If the spanwise wall velocity varies in time, a continuous flux of W_y is generated at the moving wall through the term $\frac{\partial W}{\partial t}$. Note that this term generates a flux of W_y at the wall in the same manner as a spanwise pressure gradient. A channel flow turned by a constant spanwise pressure gradient is equivalent to a channel flow turned by a wall accelerating in the spanwise direction at a constant rate (see §2.5).
- 3) Body forces can generate 3D TBLs. Gravity is usually not important unless there is a large temperature difference across the boundary layer which would generate a buoyancy force. This force can turn a TBL on a non-horizontal wall by generating W_y across the TBL (Siebers, 1983). The Coriolis force due to Earth's rotation causes Earth's TBL to be three-dimensional (Coleman *et al.*, 1990).
- 4) For certain geometries, like non-circular ducts, the Reynolds stress terms in the transport equation for W_y generate weak three-dimensionality.
- 5) W_y can enter through the outer edge, notably when a boundary layer interacts with a longitudinal vortex (Bradshaw, 1987).

These five ways in which three-dimensionality is imposed on a boundary layer may affect different regions of the boundary layer and with different intensities. They may therefore lead to different 3D effects because the turbulence structures are different near the wall and in the outer layer. Additional effects may appear when the turning is strong. Another important distinction is between equilibrium and non-equilibrium 3D turbulent boundary layers. In non-equilibrium 3D TBLs, a flow which is initially 2D or nearly so, is turned by a transverse force and the observed 3D-phenomena occur while the turbulence adjusts to the new flow direction. When the 3D TBL is in equilibrium, the turbulence has had sufficient time to adjust. An example of the latter is the flow on an infinitely large rotating disk (Littell & Eaton, 1992).

1.4.3 Review of previous results

Results from pressure-driven and shear-driven 3D TBLs will be discussed below. Three-dimensionality generated in other ways is not included.

Pressure – driven flows

Pressure-driven flows are of great practical interest. Important examples are the flow over a swept wing and flow around buildings and other obstacles.

In the flow over a swept wing, the incoming flow is turned by a pressure gradient which is roughly perpendicular to the leading edge in plan view. Except at the very front of the wing, the pressure gradient is adverse and will bend the flow away from the body of the aeroplane. In order to reduce the number of degrees of freedom, swept wing experiments are set up to approximate an infinitely long constant-cord wing, such that the flow is homogeneous in the direction of the leading edge.

Reynolds stress data for a 3D TBL were first reported by Bradshaw & Terrell (1969). This was a flow recovering on a flat plate behind a 45° swept wing. The three-dimensionality was weak with a maximum angle of 9° between the tunnel axis and the surface streamline. The only observed 3D effect was a lag between the stress angle $\tan^{-1}(\frac{\overline{v'w'}}{u'v'})$ and the mean velocity gradient angle $\tan^{-1}(\frac{\partial W}{\partial y} / \frac{\partial U}{\partial y})$. A practical consequence of this is that the eddy-viscosity is not a scalar. This prevents a simple extension of eddy-viscosity turbulence models to apply to 3D flows.

Experiments in a duct shaped to simulate a swept wing were done at the National Aerospace Laboratory (NLR) in the Netherlands as a response to the need for more

data to test and develop 3D turbulence models. The turbulence statistics were reported by van den Berg & Elsenaar (1972), Elsenaar & Boelsma (1974) and van den Berg, Elsenaar, Lindhout & Wesseling (1975). As in the experiment of Bradshaw and Terrell, the stress angle lagged behind the mean velocity gradient angle. A new finding was that the structure parameter $a_1 = \sqrt{\overline{u'^2} + \overline{v'^2} + \overline{w'^2}} / (\overline{u'^2} + \overline{v'^2} + \overline{w'^2})$, dropped below the commonly reported value of 0.15 in 2D flows. The drop in a_1 in the outer part of the TBL occurred before the changes near the wall had sufficient time to diffuse outward. This indicated that the inviscid skewing mechanism described earlier played a role in these flows.

In a Euromech meeting in Trondheim, Norway, (Fanneløp & Krogstad, 1975) the existing turbulence models were applied to 3D TBLs for which experimental data existed. During this meeting, known as the "Trondheim-trials", it became clear that the turbulence models did not perform well for 3D flows like the NLR "wing".

Bradshaw & Pontikos (1985) performed an experiment with a similar geometry to the NLR experiments except that the adverse pressure gradient was milder to avoid separation. They were able to confirm the 3D effects found at NLR. The stress angle lagged behind the mean velocity gradient angle, though never more than 8° , and the structure parameter dropped below 0.15 across the TBL.

When the flow is turned by an obstacle, the adverse pressure gradient is often stronger and the turning more rapid than for swept wings. This will usually make the flow separate earlier and measurements must be made over a shorter range in the streamwise direction. The measured turbulence statistics may therefore not have had sufficient time to be altered except near the wall.

Johnston (1970) investigated the flow over a 45° swept rectangular step with a very strong adverse pressure gradient. The vertical pressure gradient may have affected the three-dimensionality in this flow through the term $\frac{\partial^2 P}{\partial y \partial z}$ in eqn. (1.4.1). Because of the strong pressure gradients, the flow turned as much as 35° over a streamwise distance of only five boundary layer thicknesses. As with the earlier experiments of Terrell and Bradshaw, the Reynolds shear stress angle lagged behind the mean velocity gradient angle. The difference in angle was as high as 20° , much larger than what is found for swept wings.

Anderson & Eaton (1987, 1989) investigated the TBL around a wedge that was attached to the wall and pointed in the upstream direction. Two wedge angles were investigated, 90° and 60° . As with Johnston's experiment, the 3D effects were much

larger than in the swept wing experiments and were largest for the largest wedge angle. Values of the structure parameter a_1 were as low as 0.03 and the ratio of the spanwise to streamwise eddy viscosity, in coordinates aligned with the local mean flow, was as low as 0.2. The streamwise evolution of a_1 was dominated by the outward diffusion of near-wall effects to a larger extent than in swept-wing experiments. A comparison of existing 3D data led to the conclusion that the eddy-viscosity ratio decreases with increasing rate of boundary layer turning, defined as the ratio of boundary layer thickness to free-stream streamline curvature radius, while being independent of the difference in mean velocity gradient angle between the wall and the free-stream. However, the structure parameter was found to depend on both. A significant drop in a_1 and a low eddy-viscosity ratio was also found by Dechow & Felsch (1977), who investigated the flow around a wing-shaped obstacle.

Moin, Shih, Driver & Mansour (1990) investigated the statistical evolution of a fully developed 2D channel flow subjected to a sudden spanwise pressure gradient. The structure of this flow was investigated in the present work. This flow is different from the previously described flows in that all three dimensionality grows outward from the wall with no possibility of inviscid skewing. The flow is well suited for the study of near-wall three-dimensionality because the change in turbulence statistics from their initial profiles to the final steady state profiles is gradual enough for the three-dimensional effects on the statistics to be easily observed. The channel flow displays a drop in the total Reynolds shear stress, the turbulent kinetic energy and the structure parameter a_1 . Since the magnitude of the total Reynolds shear stress and the turbulent kinetic energy (normalized with the initial shear velocity and channel half width) increase with the Reynolds number, they will have higher values in the final steady state than initially. The reductions must therefore be due to the subtle effects of three-dimensionality. From the Reynolds stress budgets, they found that the decrease in $-\overline{u'v'}$ and $\overline{u'^2}$ were due to reduced respective productions, while the pressure-velocity term $-\overline{v' \frac{\partial p'}{\partial y}}$ caused the reduction in $\overline{v'^2}$. The Reynolds stress angle lagged behind the mean velocity gradient angle, with the largest difference at the wall. The mean velocity, when scaled with the total wall shear velocity, shows a log-region with a slope lower than the value of 2.4 usually found for 2D flows. Note that this flow is nominally different from a flow with an impulsively started wall motion which would be more closely related to experimentally studied flows along a spinning cylinder (see below).

Shear – driven flows

Experimental and computational investigations of flows where wall-motion generates three-dimensionality will now be discussed. In the absence of additional sources for three-dimensionality all 3D effects will grow outward from the wall.

There have been several experiments in zero pressure gradient flows along a cylinder with a rotating part. Three-dimensionality is generated by circumferential viscous forces at the wall between the stationary and the rotating parts. If the rotating part is long enough, the flow, in coordinates moving in the spanwise direction with the speed of cylinder surface, W_s , will become 2D with an angle $\tan^{-1}(W_s/U_\infty)$ with respect to the cylinder axis. The flow is then said to be collateral. However, the Reynolds stresses and the axial wall stress, normalized with U_∞ , are higher in the collateral flow due to higher effective free-stream velocity, $\sqrt{U_\infty^2 + W_s^2}$, and the radial pressure gradient (Driver & Johnston, 1990). Therefore, when the flow enters or leaves the rotating part, an adjustment toward the new 2D profiles will grow outward as the flow progresses downstream. Results from three cylinder-experiments are described below.

Bissonnette and Mellor (1973) performed measurements on a cylinder with fixed forebody and rotating afterbody. They found that the flow remained collateral near the wall when the flow entered the rotating part, while further out the flow was 3D and the Reynolds shear stress angle lagged behind the mean velocity gradient angle. The eddy-viscosity in the spanwise direction was in most cases between 0.5 and 0.8 times the streamwise (axial) eddy-viscosity. Using scaling arguments, they argued that this was at least in part due to curvature effects. They also investigated the law-of-the-wall for this flow. Following a suggestion by Clauser, they chose a coordinate system that moved in the spanwise direction with the wall and aligned with the free stream velocity $\sqrt{U_\infty^2 + W_s^2}$. The slope in the log-region was considerably lower than in 2D flows. Again scaling arguments were used and it was found that the curvature contributed to this result. The spanwise wall stress increased “instantly” as the flow entered the rotating part and decayed downstream, while the streamwise wall stress increased slightly in the axial direction.

Lohmann (1976) investigated the same geometry, but with a stronger surface to free-stream velocity ratio. The spanwise TBL did not grow to the same thickness as the streamwise TBL within the region measured, causing the streamwise boundary layer thickness, δ , to be unaffected by the spanwise wall movement. When the surface

velocity was increased, the growth of the spanwise TBL increased slightly and the shape of the spanwise mean velocity profile outside $y/\delta = 0.05$ was altered. As in the experiment of Bissonette and Mellor, the TBL was collateral near the wall and three-dimensional further out, with the stress angle lagging the mean velocity gradient angle. The Reynolds stresses increased rapidly near the wall when the flow entered the rotating part and the increase diffused outward as the flow progressed downstream. Any weakening of the Reynolds stresses due to 3D effects were therefore difficult to detect. However, for $W_s/U_\infty=1.45$, the axial wall stress decreased slightly after the rapid initial increase and then continued to increase toward a new steady state, and for $W_s/U_\infty=2.2$, it remained constant for a while after the immediate increase, and then increased further to a higher 2D value. This indicates that the 3D effects tend to reduce the axial wall stress.

Driver & Johnston (1990) reported on a similar flow. In their experiment, a collateral TBL on a spinning forebody became three-dimensional as the flow entered the stationary afterbody. This makes measurements easier, but it creates the additional effect that the initial 2D TBL is not aligned with the axial direction. As the flow enters the stationary cylinder section, the Reynolds stresses reduce to their new steady state. However, unlike the normal intensities, the axial Reynolds shear stress, $-\overline{u'v'}$, fell below its final steady state value and then recovered. The reduction is due to 3D effects which also caused the structure parameter a_1 to fall below its steady state value and then recover. Surprisingly, a_1 was as high as 0.17 on the rotating part. The mean velocity gradient angle relaxed toward zero more rapidly than the Reynolds shear stress angle.

The main purpose of Driver and Johnston's work was to study the cylinder flow in an adverse axial pressure gradient. Since there was no spanwise pressure gradient, a mechanism for three-dimensionality did not exist in the outer part of the TBL. Their objective was to investigate properties of the outward-growing three-dimensionality in a TBL with an adverse pressure gradient. Earlier experiments on this flow (except that the flow progressed from the stationary part to the rotating part) were performed by Furuya *et al.* (1977) and Driver & Hebbbar (1989). They found the effect of the axial pressure gradient to be minimal. In the absence of cylinder rotation, the adverse axial pressure gradient tends to weaken the Reynolds stresses near the wall and increase them further out. Driver and Johnston found that when the flow is three-dimensional, the increase in the outer region is less pronounced. Along a stationary cylinder with

an axial pressure gradient, a_1 was weakened across the TBL, but its radial gradient remained close to zero outside the near-wall region. In the 3D TBL, a_1 did not drop near the wall, but further out it dropped increasingly with increasing distance from the cylinder.

Shear – driven flows in equilibrium

Some studies have been performed in the so-called equilibrium flows, where the turbulence experiences the three-dimensionality over a long time and has had time to adjust to it. One of the reasons for studying these flows is that they often have fewer degrees of freedom. The relevance of these flows to the non-equilibrium 3D flows is not yet clear, but they show some non-equilibrium characteristics. Three studies are described below.

The first of these is the direct numerical simulation of a horizontally homogeneous flow with the free-stream velocity vector rotating about a vertical axis at a constant rate and a fixed magnitude (Spalart, 1989). In coordinates rotating with the free-stream, the flow is statistically steady. When the magnitude and rotation rate of the free-stream vector is used for normalization, the Reynolds number and the distance from the wall are the only independent variables. The a_1 parameter, when plotted against y^+ , is reduced and the amount of reduction increased with increasing Re. However, the difference between the Reynolds shear stress angle and the mean velocity gradient angle was small and changed sign several times across the TBL.

The Ekman layer, the prototype of planetary boundary layers, was simulated by Coleman *et al.* (1990). In the free stream, the pressure gradient is perpendicular to the flow direction and is balanced by the Coriolis force. The structure parameter profile varied greatly, but was mostly below 0.15. It did not seem to have any region with a constant value. The difference between the Reynolds shear stress direction and the mean velocity gradient direction was small in this flow as well.

Littell and Eaton (1992) investigated a 3D TBL on a spinning disk. Profiles of the Reynolds stresses, normalized with the wall shear velocity, collapsed well when plotted against the distance from the wall, normalized with the momentum thickness, for different values of rotation rate and radius. Again, the lag between the turbulent shear stress direction and the mean velocity direction was very small. The structure parameter had a surprising profile with a peak near the wall and a near-linear drop further out. Conditional averaged two-point correlations were computed and based

on these it was suggested that a vortex generates weaker sweep-motion ($u' > 0, v' < 0$ and $-u'v' > 2\sqrt{u'^2 v'^2}$) in a 3D TBL if its sign of rotation is opposite to the mean streamwise vorticity at the wall and weaker ejections ($u' < 0, v' > 0$ and $-u'v' > 2\sqrt{u'^2 v'^2}$) if its sign of rotation is the same.

1.4.4 Structural "theories" for the observed 3D effects

It is known that quasi-streamwise vortical structures play an important role in TBLs. The weakening of the total Reynolds shear stress and other 3D effects are therefore believed to reflect the effect of three-dimensionality on these eddies.

In the spinning cylinder flow, Lohmann (1976) found an increased contribution from small scales and a reduced contribution from large scales in the energy spectrum. He therefore suggested that the transverse shearing motion broke up the large eddies into smaller eddies and that recovery represented the build-up of large eddies. The increase in small scales may in part be an artifact of the coordinate system, since the 2D flow has more small and medium size scales in the spanwise direction.

Bradshaw & Pontikos (1985) suggested that the eddies are tilted over in the spanwise direction by the spanwise strain. Since the eddies near the wall have a low angle relative to the wall, while further out they appear with high inclination, the outer eddies are most likely to be toppled. Robinson (1991) described the dominant vortical structure in the outer part of 2D TBLs, as consisting of an arch-shaped front with high inclination angle and one or two legs with lower angle closer to the wall. The strongest ejections in the outer part were found inside the arch. These ejections would be affected if the arch is convected further in the spanwise direction than the legs.

Anderson & Eaton (1989) suggested that near the wall the mean streamwise vorticity will destroy the streamwise vortices with opposite sign of rotation and roll up into vortices with the same sign of rotation. Vortices with one sign would dominate, which could reduce the contribution from strong mixing motion between two vortices of opposite sign.

Simpson & Devenport (1990) suggested that fluid swept toward the wall will in 3D TBLs displace most low-speed fluid in one spanwise direction. This fluid, when ejected, would generate positive $\overline{u'w'}$. However, they pointed out that the fluid need not eject outward to the same level as in a 2D TBL, because the flow "has a third dimension of spatial freedom". It is not clear what kind of mechanism this refers to

since 2D and 3D flow terminology refers to the mean flow only and all turbulent flows are three-dimensional.

Eaton (1992) suggested that the behavior of an imbedded vortex in 3D TBLs could cast light on the behavior of naturally occurring near-wall vortices. The latter are much smaller, but are often single-legged with a low inclination angle. Shizawa & Eaton (1990) introduced a single, large, longitudinal vortex of either sign into the 3D wedge-flow of Anderson & Eaton (1989) and found that vortices of both signs decayed quicker than they would in a 2D TBL. In addition, the ejection-mechanism depended strongly on the sign of the embedded vortex. If the vortex induced secondary flow near the wall in the same direction as the spanwise pressure gradient, no secondary flow separation took place and no low-speed streaks were generated. Vortices of opposite sign induced motion opposing the 3D TBL and a strong outward motion took place. Eaton (1992), based on the idea that ejections take place as a result of streaks becoming unstable, suggested that the reduced number of streaks generated less ejections and therefore less Reynolds shear stress.

It should be noted that these suggestions are not mutually exclusive. The key mechanism may depend on the distance from the wall, the turning rate and other quantities.

In Chapter 4 the results of our study of the three-dimensional channel flow will be described in detail. The mechanisms underlying the reduced Reynolds shear stress will be presented and compared with the previously suggested mechanisms described above.

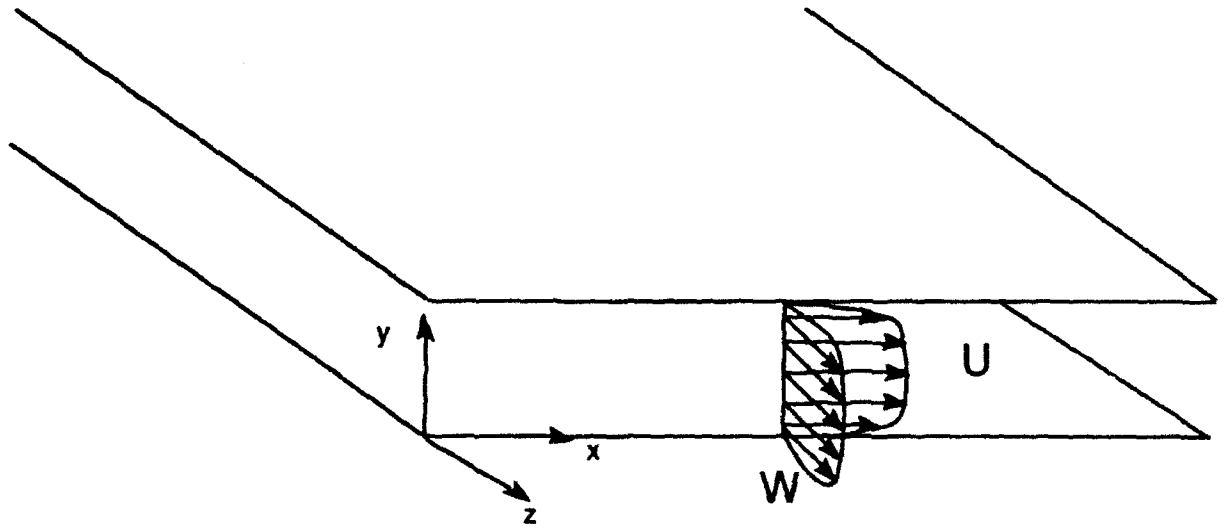


FIGURE 1.1. Schematics showing the channel flow geometry.

CHAPTER 2

NUMERICAL AND ANALYTICAL CONSIDERATIONS

In this chapter a description of the geometry, the numerical method and physical and numerical parameters are presented. In addition, the tools used for the analysis and postprocessing of the simulation data are described.

2.1 Geometry and coordinates

The simulated flow is initially a fully developed turbulent Poiseuille flow. This is a pressure-driven flow between two infinitely large, parallel, horizontal walls with a steady mean velocity, $(U(y), 0, 0)$. A constant spanwise pressure gradient is suddenly imposed which causes a transient, three dimensional evolution of the flow. The perturbed flow eventually becomes 2D and statistically steady in a new direction. It is the transient behavior which is of interest in this study. The geometry and the coordinates for the simulated flow are shown in Figure 1.1. The x -axis is aligned with the initial mean flow direction, the y -axis is normal to the walls, and the z -axis is in the initial spanwise direction. The velocity components in the (x, y, z) directions will be denoted by (u, v, w) , or (u_1, u_2, u_3) respectively.

One of the difficulties in studying three-dimensional turbulent boundary layers is the choice of coordinates. In rotated coordinates the velocity components will be denoted as (u_*, v, w_*) . There are several characteristic angles, and those used in the current work are listed below. They will be called the mean velocity angle, the mean velocity gradient angle, the Reynolds shear stress angle and the intensity angle, respectively

$$\gamma_s = \tan^{-1}[W/U] \quad (2.1a)$$

$$\gamma_r = \tan^{-1}[\overline{v'w'}/\overline{u'v'}] \quad (2.1b)$$

$$\gamma_g = \tan^{-1}\left[\frac{\partial W}{\partial y} / \frac{\partial U}{\partial y}\right] \quad (2.1c)$$

$$\gamma_i = 0.5 \tan^{-1}[2\overline{u'w'}/(\overline{u'^2} - \overline{w'^2})] \quad (2.1d)$$

The latter is the angle of maximum streamwise intensity.

2.2 Numerical method

The 2D turbulent channel flow was computed by Kim, Moin and Moser (1987). They used direct numerical simulation technique which resolves all the essential scales and no modelling is needed. The same computer code is used here in the simulation of the 3D channel. Several stored velocity fields of Kim *et al.* were used as initial conditions for different realizations of the 3D flow. A brief description of the numerical method is given below. For a detailed description, refer to Kim *et al.* (1987).

The numerical method is a spectral method with pressure eliminated from the equations. Fourier expansions are used for computation of the horizontal spatial derivatives and the Chebychev expansion is used for vertical derivatives. The viscous terms are time-advanced using the Crank-Nicholson method, while the Adams-Bashforth method is used for the non-linear terms. The discretized equations are Fourier transformed in the horizontal plane and then solved using the Chebychev-tau method (Gottlieb & Orszag, 1977) for each wave number. The governing equation for the vertical component of the vorticity, ω_y , is solved first, followed by the fourth order equation for $\nabla^2 v$ which is separated into two second-order equations. The extra boundary conditions needed at the walls are provided by the continuity equation, which reduces to $\frac{\partial v}{\partial y} = 0$ at $y=0$. The solution for v and ω_y together with the continuity equation and the definition of ω_y provide equations for u and w . Since the pressure is not computed as part of the solution algorithm, it is computed separately using a Poisson-solver when needed.

The turbulence statistics for the 2D data are in agreement with existing experimental results, and have been widely used in turbulence research (Moin, 1987). It is therefore a well verified code.

2.3 Parameters and grid

The effect of periodic boundary conditions on turbulence statistics is believed to be minimal if the horizontal dimensions of the computational box are sufficiently large that all correlations decay to zero in a distance less than half the computational box size in each of the horizontal directions. In the present study, the physical dimensions of the computational domain are $(L_x, L_y, L_z) = (4\pi\delta, 2\delta, \frac{4}{3}\pi\delta)$, where δ is the channel half width. The number of grid points is $(NX, NY, NZ) = (128, 129, 128)$. The Reynolds number, based on δ and the 2D wall shear velocity, $u_{\tau 2D} \equiv \sqrt{\nu \frac{\partial U}{\partial y}}$, is 180,

which corresponds to a Reynolds number based on the centerline velocity of 3300. For the 2D flow, the grid dimensions, in wall units, are $\Delta x^+ = 17.67$ and $\Delta z^+ = 5.89$, and the first grid point off the wall is at $y^+ = 0.054$.

The governing equations are normalized with the 2D shear velocity, $u_{\tau 2D}$, and δ , which gives an initial non-dimensional streamwise pressure gradient $\frac{\partial P}{\partial x} = -1$. For the 3D simulation, $\frac{\partial P}{\partial x}$ is set to keep the mean mass flux in the x -direction constant. The imposed spanwise pressure gradient is set to -10 . For the time-period considered in this study, the mean flow angle was less than 45° , which is low enough for the 3D flow to be sufficiently resolved with the 2D grid. Some simulations were performed with an extremely high spanwise pressure gradient, $\frac{\partial P}{\partial z} = -100$. This was done in order to make the effects large and thus easier to study. For these simulations it was necessary to use $NX=256$ because of the large turning angle which required the horizontal grid to be closer to a square.

2.4 The minimal flow unit

One of the difficulties with the study of organized structures in turbulent boundary layers is the presence of several structures located randomly in space and time. The minimal flow unit (Jimenez and Moin, 1990) is a channel flow in which the dynamics is forced to be much simpler. The horizontal dimensions in the channel flow code are reduced to the smallest size that can maintain turbulence. Only one low-speed streak and often just two or three vortical structures are found within the computational domain. The flow is called a minimal unit because, apparently with a minimum set of structures the basic cycle of turbulence generation and dissipation is maintained. Even though the flow would not occur naturally, it does satisfy the Navier-Stokes equations and the turbulence statistics are very similar to those found in a "regular-sized" channel. It is therefore believed that the key mechanisms that maintain turbulence in the minimal flow are nearly the same as that in the regular channel.

In the minimal channel, the spanwise dimension of the computational box was slightly less than 100 wall units and its streamwise dimension was about 250-350 wall units. These correspond approximately to the mean spanwise distance between the streaks and the streamwise extent of vortical structures in the channel flow.

The minimal flow studied in this work had a Reynolds number, $Re_L = \frac{U_L \delta}{\nu} = 2000$ and physical dimensions $(L_x, L_y, L_z) = (\pi\delta, 2\delta, \frac{\pi}{3}\delta)$ while the number of grid-points were $(NX, NY, NZ) = (32, 129, 16)$, where U_L is the laminar center line velocity with the same mass flux.

In the study to be described in §3.1.3, the minimal channel was used primarily to obtain an increased understanding of the dynamics of the “2D” wall turbulence. In addition to the advantage of a simplified turbulence, the small size of the computational domain makes it much easier to follow a single structure in time. Due to periodic boundary conditions, the structure of interest will remain throughout its lifetime inside the computational domain which is so small that it can easily be found.

A spanwise pressure gradient was applied to the minimal flow unit as well, but because the spanwise size of the computational domain is very small, the computations were meaningful only for very small turning angles. The spanwise pressure gradient was therefore chosen to be lower than in the regular 3D channel, $|\frac{\partial P}{\partial z}| = 5|\frac{\partial P}{\partial x}|$. It was also useful to apply spanwise pressure gradients of both signs to the same initial field to see how the same eddy would respond to mean streamwise vorticity of both signs.

2.5 Preliminary considerations for the 3D turbulent channel flow

The purpose of this section is to show that the 3D channel flow considered in this study behaves like a shear-driven TBL and to describe its global characteristics. It is useful to first look at the laminar case. The governing equations are then

$$\frac{\partial u_i}{\partial t} = -\frac{\partial p}{\partial x_i} + \frac{1}{Re} \frac{\partial^2 u_i}{\partial y^2} \quad (2.5.1)$$

The equations are uncoupled and the u_1 -profile will not change when the spanwise pressure gradient is imposed. Because w is independent of u , it will evolve as an impulsively started 2D channel flow. It is more instructive to consider the governing equation for $w_y \equiv \frac{\partial w}{\partial y}$ and its boundary conditions,

$$\frac{\partial w_y}{\partial t} = \frac{1}{Re} \frac{\partial^2 w_y}{\partial y^2} \quad (2.5.2)$$

$$\frac{\partial w_y}{\partial y} \Big|_{y=0} = Re \frac{\partial p}{\partial z} \quad w_y \Big|_{y=\delta} = 0.$$

where $y = \delta$ is the channel centerline. It can be seen that the spanwise pressure gradient does not influence $\frac{\partial w}{\partial y}$ inside the flow; it generates a flux at the wall, which diffuses outward. A spanwise boundary layer will therefore grow outward from the wall. Outside this boundary layer, w has no spatial gradients, and

$$w_{\infty}(t) = - \int_0^t \frac{\partial p}{\partial z}(t') dt' = - \frac{\partial P}{\partial z} t$$

A series solution for w can be found for the entire domain using the method of separation of variables

$$w(t, y) = - \frac{\partial p}{\partial z} Re \left\{ y - \frac{1}{2} y^2 - 2 \sum_{n=0}^{\infty} e^{-\frac{[(\frac{1}{2}+n)\pi]^2}{Re} t} \left[\left(\frac{1}{2} + n \right) \pi \right]^{-3} \sin \left[\left(\frac{1}{2} + n \right) \pi y \right] \right\} \quad (2.5.3)$$

A similarity solution exists for the case of infinite distance between the walls

$$w(\eta) = - \frac{\partial p}{\partial z} t \left\{ c (\eta^2 + 1) \int_0^{\eta} (\eta^2 + 1)^{-2} e^{-\frac{1}{2} \eta^2} d\eta - \eta^2 \right\} \quad (2.5.4)$$

where,

$$c^{-1} = \int_0^{\infty} (\eta^2 + 1)^{-2} e^{-\frac{1}{2} \eta^2} d\eta, \quad \eta = \sqrt{Re/2} \frac{y}{\sqrt{t}}$$

This solution is in excellent agreement with eqn. (2.5.2) as long as the spanwise boundary layer is thin compared to the channel half width.

When the flow is turbulent, the governing equations for the mean velocities, U_i , are

$$\frac{\partial U_i}{\partial t} = - \frac{\partial P}{\partial x_i} + \frac{1}{Re} \frac{\partial^2 U_i}{\partial y^2} - \frac{\partial \overline{u'_i v'}}{\partial y} \quad (2.5.5)$$

As in the laminar flow, the vertical mean velocity component is zero. It can be shown that the mean pressure is

$$P(x, y, z, t) = \alpha x + \beta z - \overline{\rho v'^2}(y, t) \quad (2.5.6)$$

plus an arbitrary constant, where α and β are the imposed horizontal mean pressure gradients. Their values in the present flow were given in §2.3. Since $\overline{v'w'}$ is zero initially, W will grow like the laminar flow until $\overline{v'w'}$ becomes significant. The spanwise boundary layer will grow outward from the wall in the turbulent case as well, while

further out $W(t) = -\frac{\partial P}{\partial z}t$ independent of y . The mean velocity in the x direction, U , is affected by the spanwise pressure gradient through $-\frac{\partial \overline{u'v'}}{\partial y}$ only. Any change in U is therefore due to a change in the structure of the turbulence. When the flow relaxes back to a new steady state, the Reynolds stresses will be higher than that of the initial flow since the Reynolds number is higher.

The pressure driven 3D channel flow considered here is equivalent to a channel flow with walls moving with a uniform spanwise acceleration. This can be shown as follows. The transformation

$$w = \hat{w} - \frac{\partial P}{\partial z}t \quad z = \hat{z} - \frac{1}{2} \frac{\partial P}{\partial z}t^2 \quad (2.5.7a)$$

gives

$$\frac{\partial \hat{w}}{\partial t} + \hat{u}_k \frac{\partial \hat{w}}{\partial \hat{x}_k} = -\frac{\partial p'}{\partial \hat{z}} + \frac{1}{Re} \frac{\partial^2 \hat{w}}{\partial \hat{y}^2} \quad (2.5.7b)$$

$$\hat{w}(y = 0, t) = \hat{w}(y = 2\delta, t) = \frac{\partial P}{\partial z}t \quad (2.5.7c)$$

This is the governing equation and boundary conditions for a channel flow whose walls are accelerating in the spanwise direction at a constant rate.

2.6 3D channel flow vs 3D boundary layers

The 3D channel flow studied here should be contrasted to 3D boundary layers studied experimentally. As mentioned in Chapter 1, most pressure-driven spatially evolving 3D boundary layers encounter inviscid skewing of the vorticity vector in the outer flow. This effect is absent in the present simulations where all 3D effects diffuse outward from the wall. The present study examines the effect of three-dimensionality on the near wall turbulence. Most 3D boundary layers studied experimentally or encountered in applications are statistically stationary whereas the 3D channel flow of the present study is temporally evolving. Moreover, due to spatial homogeneity, at any instant the ensemble averaged streamlines are straight. However, the flow features are similar if the streamwise coordinate and time are related via Taylor's hypothesis. Figure 2.1 shows the mean flow particle paths in the channel flow, showing the typical curvature and the wall-normal skewing expected in spatially evolving boundary layers. Unfortunately, in many experimental studies of 3D boundary layers, the means for generating the three-dimensionality has also introduced adverse streamwise pressure gradients. Some of the observed effects may be attributed to the adverse pressure

gradient rather than to three-dimensionality. The 3D channel flow studied here does not have such additional complex effects.

2.7 Methods of identifying the mechanics underlying the 3D effects

In this section various statistical methods and a technique for the analysis of the unsteady flow dynamics are described.

The probability density function (PDF) is a useful quantity for linking changes in statistical quantities to changes in the turbulence structures. PDFs show the distribution of a quantity, f , and are normalized such that

$$\int_{-\infty}^{\infty} P(f)df = 1. \quad (2.7.1)$$

where $P(f)$ is the PDF of f . When the PDF is multiplied (weighted) by some function $g(f)$, the integral over all values of f is equal to \bar{g} . A plot of the weighted PDFs for the 2D and the 3D flows will therefore show how much the change in occurrence of each f -value contributes to the change in \bar{g} . The joint PDF between two flow variables, f_1 and f_2 , shows how the different combinations of f_1 -values and f_2 -values are distributed. When it is weighted by some function $g(f_1, f_2)$, it shows how each combination contributes to \bar{g} . In the current work, this is used to study how each combination of u'_i and u'_j contributes to the change in the Reynolds shear stress $\overline{u'_i u'_j}$.

The quadrant analysis (Willmarth & Lu 1972; Wallace *et al.* 1972) of $\overline{u'_i u'_j}$ is a useful supplement to weighted joint PDFs. Each value of $u'_i u'_j$ is classified into one of four quadrants according to the sign of u'_i and u'_j . The Reynolds shear stress can then be separated into a sum of four terms, each equal to the integral of $u'_i u'_j P(u'_i, u'_j)$ over that quadrant. The change in a term shows the integral effect of all changes within the quadrant and how it varies with the distance from the wall.

Simpson and Devenport (1990) pointed out the usefulness of an octant analysis in the study of 3D TBLs. The Reynolds stresses are separated into 8 terms according to the sign of each of the velocity fluctuations. For example, the first octant-term for $\overline{u'v'}$ is equal to the sum of $u'v'$ over all points where u' , v' and w' are all positive, divided by the total number of points. We will use the octant analysis to distinguish between the contributions to the Reynolds stresses by streamwise vortices of positive and negative signs of rotation. When the octant-contribution for the 2D flow is subtracted, it can be seen how each octant contributes to the change in the Reynolds

stress. In the current work, only the change in magnitude of the contribution for each octant is considered.

The average flow field around an event (loosely defined as a fluid motion in some specified direction) or a structure can be computed using conditional averaging (Blackwelder & Kaplan 1976; Kim & Moin 1986). We have examined the effect of three-dimensionality on conditional eddies. In the current work this is done in the following manner : A range is specified for a chosen quantity at a particular distance from the wall. For each point which satisfies these conditions, the origin of the coordinate system is moved to that point and the surrounding flow field is added to that from the previous points.

Two-point correlations are used to extract information about the size and relative locations of structures. The direction of strongest correlation was used to estimate the average angle of structures as follows. In a horizontal plane, the angle of maximum correlation, θ_R , is derived from $\frac{d}{d\alpha} \overline{f(x, z) f(x + \Delta x, z + \alpha \Delta x)} = 0$ where $\alpha \equiv \tan(\theta_R) = \frac{\Delta z}{\Delta x}$. A Taylor expansion and using the horizontal flow homogeneity and periodicity of this flow leads to

$$\alpha = - \frac{\overline{\frac{\partial f}{\partial x} \frac{\partial f}{\partial z}}}{\overline{\frac{\partial f}{\partial z} \frac{\partial f}{\partial z}}} \quad (2.7.2)$$

Finally, a non-statistical approach called the *companion flows method* was used to study the unsteady flow dynamics. Two simulations, one with and one without a spanwise pressure gradient, were started from the same "2D" initial field. Gradually, the two flows deviate due to 3D effects. Comparison of the two flows allow identification of 3D effects on the instantaneous structures. For example, the flow field around a vortex in the "2D" flow can be compared with the field around the same vortex in the 3D flow and those vortices which generate significantly different fluctuations can be detected. Comparison is most useful for early times, when large differences are restricted to a few locations in the flow.

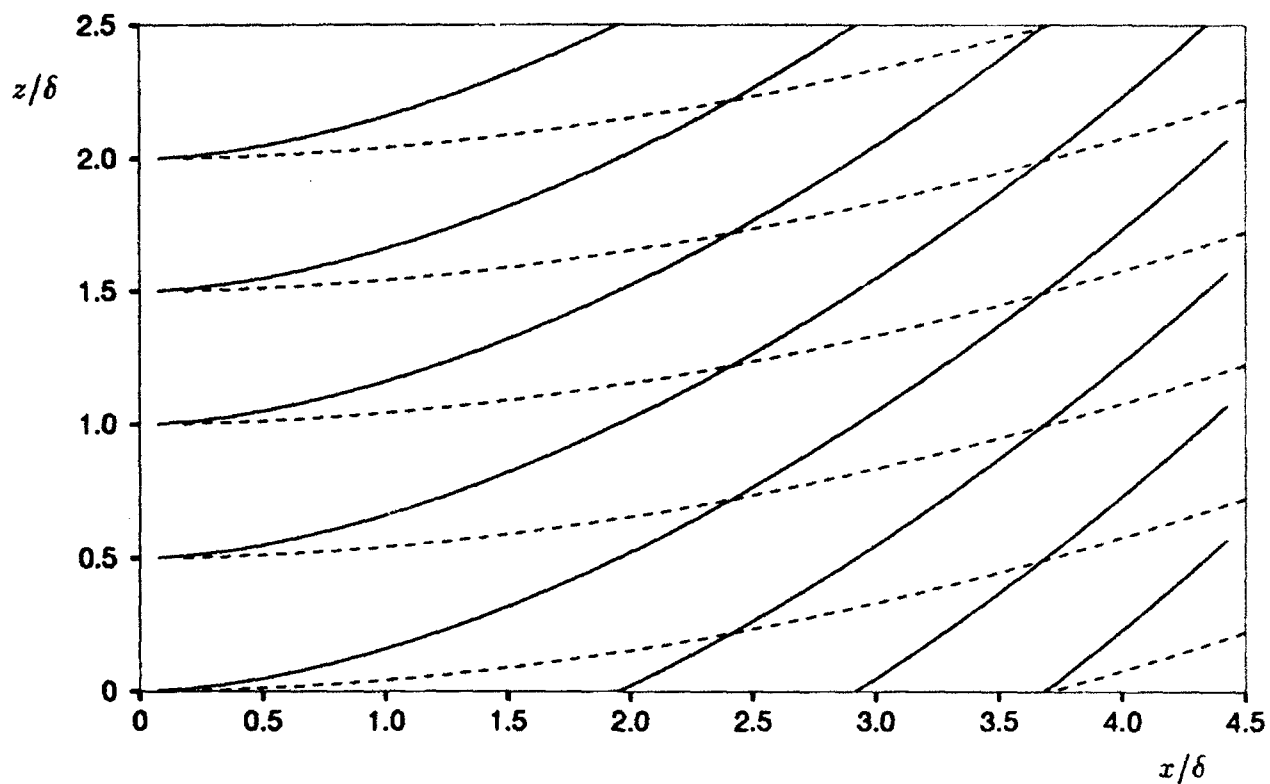


FIGURE 2.1. Mean flow path lines for $y_{2D}^+ = 11$ (—) and $y_{2D}^+ = 20$ (- - -) obtained from simulations described in Chapter 4.

CHAPTER 3

NEAR-WALL TURBULENCE STRUCTURES IN "2D" BOUNDARY LAYERS

We refer to "organized structures" as the non-random component of the velocity fluctuations in a turbulent flow. To quote Lumley, an organized structure is "a pattern which is recognizable and recurs throughout the flow". They are known to be the primary contributors to the Reynolds shear stresses and other statistical quantities and are also believed to be important in the dynamics which maintains turbulence. Several types of structures have been identified in boundary layers, but in this work our discussion tends to focus on the three-dimensional effects on the widely observed quasi-streamwise vortices, high/low-speed streaks and shear layers. Streamwise vortices are associated with large values of v and w and ω_x , streaks are associated with large streamwise velocity fluctuations, u' , normal vorticity ω_y , and spanwise vorticity fluctuations ω'_z ; whereas shear layers protruding from the wall are associated with large ω'_z away from the wall. A brief review of the existing knowledge and new findings regarding these structures are given below. This study is limited to the near-wall region because the spanwise boundary layer originates and grows outward from the wall.

3.1 Quasi-streamwise vortices

A vortex is a swirling motion in coordinates moving with and aligned with its axis. Several vortex lines coming together in a compact region of space is also a good indicator for the presence of a vortex in that region. Both definitions will be used below. The velocity vectors in any vertical cut normal to the mean flow direction show that quasi-streamwise vortices are abundantly present in the near wall region and are associated with intense velocity fluctuations (Figure 3.1a). Streamwise vortices have been shown to be responsible for turbulence generation and the so called bursting event is merely due to the passage of such vortices past the measuring station (Kim & Moin, 1986). In the near-wall region ($y^+ < 20$) the most intense v' , w' and $u' > 0$ are associated with the vortices closest to the wall (Figure 3.1).

3.1.1 Average size and location

The mean location of the near wall streamwise vortices is at $y^+ = 20$, (Kim, Moin & Moser, 1987). Once a streamwise vortex was identified in a $(z - y)$ plane, its streamwise extent was determined by a sequence of $z - y$ cuts in the positive and negative x -direction. It was determined that the streamwise extents of the vortices rarely exceed $\Delta x^+ = 350$. This is consistent with a mean streamwise spacing between near-wall vortical structures of 440 reported by Clark and Markland (1971).

3.1.2 Detection of vortices

Both definitions of a vortex in terms of swirling motion and collapsed set of vortex-lines can be used to identify vortices in instantaneous flow fields. However, when several vortices are to be visualized in 3D space it is useful to have a function whose contour surfaces capture vortices. One obvious choice for such a function is the streamwise vorticity. A study of how well contours of streamwise vorticity fluctuations capture swirling velocity vectors in the $z - y$ plane reveals that contour levels of magnitude $60u_{\tau 2D}/\delta$ does a fairly good job (Figure 3.1a). In the minimal channel, streamwise vorticity fluctuations of magnitude $0.5u_L/\delta$ were used. Low pressure regions was used by Robinson (1991) to detect vortices, but in the near-wall region of the channel flow no threshold on pressure was found which captured most of the vortices present, and only vortices. The pressure minima in the centers of near-wall vortices was not sufficiently strong compared to low-pressure events occurring very close to the wall. One way to compensate for this is to identify regions of local minima for p . This can be done by plotting high values of $\nabla^2 p$. This procedure captured vortices slightly better than contour surfaces of ω_x . Consider the Poisson equation for pressure,

$$\nabla^2 p = -\rho \frac{\partial u_i}{\partial x_j} \frac{\partial u_j}{\partial x_i}.$$

The dominant source term inside streamwise vortices was found to be $\frac{\partial w}{\partial y} \frac{\partial v}{\partial z}$, which is the product of the component terms in ω_x . Hunt, Wray & Moin (1988) suggested using the second invariant of the velocity gradient tensor together with low pressure levels as the detection criterion for vortices. This did not seem to improve significantly on the detection of vortices close to the wall, but may be useful further away from the wall.

With a few exceptions, surfaces of streamwise vorticity fluctuations will be used to identify vortices in the present study because ω'_x is easily computed and gives the sign of rotation for the vortex as well. For quantitative studies, the swirling velocity vectors in a vertical plane normal to the vortex-axis were used to identify vortices.

3.1.3 Dynamics of quasi-streamwise vortices in TBLs

The dynamics of quasi-streamwise near-wall vortices was studied using the minimal channel (see §2.4). It is convenient to study the dynamics in this flow because the computational domain is small and it is significantly more economical to follow the temporal evolution of the flow structures.

Any viable description of the flow dynamics is considered complete if it is cyclic. In the following, the process leading to the formation of streamwise vortices will be described, i.e. the sequence of events leading to the roll-up of a layer of vorticity into a streamwise oriented vortex rod will be outlined.

Figures 3.2 and 3.3 show the roll-up of a layer of streamwise vorticity into a streamwise vortex. Initially, a compact streamwise vortex (shown by dashed lines) and two layers of streamwise vorticity of opposite sign are discernible. Of interest is the vortex layer near the wall. The layer is seen to roll-up and form a compact streamwise vortex. A perspective view of the first roll-up is shown in Figure 3.4.

The sequence of cyclic underlying events for the production of this streamwise vortex are as follows. We begin with an *inclined* streamwise vortex near the wall (corresponding to the vortex marked by the dashed lines in Figure 3.2). Consider the governing equation for the streamwise vorticity

$$\frac{D\omega_x}{Dt} = \omega_x \frac{\partial u}{\partial x} + \omega_y \frac{\partial u}{\partial y} + \omega_z \frac{\partial u}{\partial z} + \nu \nabla^2 \omega_x, \quad (3.1)$$

The tilting terms on the right hand side of eqn. (3.1) are simplified as follows

$$\omega_y \frac{\partial u}{\partial y} + \omega_z \frac{\partial u}{\partial z} = \frac{\partial v}{\partial x} \frac{\partial u}{\partial z} - \frac{\partial w}{\partial x} \frac{\partial u}{\partial y} \quad (3.2)$$

Instantaneous contour plots of all the terms in the ω_x equation clearly revealed that the regions of large values of the second term in the right hand side of (3.2) coincide with the layer of streamwise vorticity shown in Figure 3.2 (see Figure 3.5). Therefore, $\frac{\partial w}{\partial x} \frac{\partial u}{\partial y}$ is the dominant contributor to the formation of the streamwise *layer* of vorticity shown. The tilting of the parent streamwise vortex with respect to the

wall leads to significant $\frac{\partial w}{\partial x}$ (Figure 3.6a). The layer is stronger on the downwash side of the parent vortex due to higher values of $\frac{\partial u}{\partial y}$ encountered there (Figure 3.2).

This is how the streamwise vortex layer is generated. The layer is unstable (Jimenez & Orlandi, 1992) and rolls into a streamwise vortex. Examination of the terms in eqn. (3.1) reveals that once the vortex is formed, the stretching term, $\omega_x \frac{\partial u}{\partial x}$, becomes dominant and intensifies the vortex (Figure 3.7). The inclination of the newly formed vortex generates horizontal velocity derivative, $\frac{\partial u}{\partial x}$ (Figure 3.6b).

Note the velocity derivative along the axis of the inclined vortex, ω_I , is

$$\frac{\partial u_I}{\partial x_I} = \frac{\omega_i \omega_j}{\omega_k \omega_k} \frac{\partial u_i}{\partial x_j}$$

Computation of each term showed that the dominant term is

$$\frac{\omega_x^2}{\omega_k \omega_k} \frac{\partial u}{\partial x}$$

It is interesting that even though the vortex is situated near the wall the term involving $\frac{\partial u}{\partial y}$ has less contribution to stretching than the term involving $\frac{\partial u}{\partial x}$.

Note that according to the process described above only tilted streamwise vortices are capable of self-generation and self-induced stretching. It is well known that a streamwise vortex near a wall is associated with a concentration of vorticity of opposite sign at the wall. It is important to distinguish between this vorticity and the vortex layer of opposite sign described here. In fact, Orlandi and Jimenez (private communication) have demonstrated that the wall streamwise vorticity does not play an important role in the near wall dynamics.

3.2 High- and low-speed streaks

Contours of u' in horizontal planes near the wall are highly elongated in the streamwise direction, particularly in the viscous sublayer. Low-speed streaks ($u' < 0$) are longer than high-speed streaks (Robinson, 1991). The former will usually have a width between $\Delta z^+ = 20$ and 40 and their lengths can exceed $\Delta x^+ = 2000$. Contours of positive u' cover wider regions and become rapidly shorter with increasing contour-levels. Their widths vary significantly, but are mostly between $\Delta z^+ = 40$ and 80. The average distance in the spanwise direction between two streaks of the same type (according to the sign of u') is well established as being close to $\Delta z^+ = 100$. Streaks contain most of the intense u' , ω_z and ω_y near the wall.

The significant streamwise extent of u' -contours may be due to a sequence of vortices following each other, pumping high-speed fluid toward the wall and low-speed fluid away from the wall. Plots of the velocity vectors in $z - y$ planes along a randomly chosen low-speed streak support this scenario (a few planes are shown in Figure 3.8). Note that the vortices seen near the streak in the $z - y$ planes in Figure 3.8 have alternate signs, and that the distance between the vertical planes is slightly more than 350 wall units (see §3.1.1). This picture is consistent with the dynamics of vortex-generation as described in §3.1.3. There, it was argued that near-wall vortices are generated below tilted near-wall vortices of opposite sign. Since the newly generated vortex is closer to the wall, it will have a lower streamwise convection velocity and will therefore end up behind the "parent-vortex". A sequence of vortices with alternate signs and varying distances from the wall can thus be created.

As pointed out above, contours of positive u' tend to be shorter than those of negative u' . Marking of an instantaneous flow field according to the sign of v reveals a streaky pattern (Figure 3.9a). However, contours become rapidly less elongated when the magnitude of the contour level is increased (not shown) and both high speed and low speed streaks contain regions of intense v which are not highly elongated. The relationship between the magnitude of u' and v' can be seen from the joint probability density function between u' and v' (not shown). It shows that in the viscous sublayer the magnitude of $u' > 0$ is correlated with the magnitude of $v' < 0$ while the magnitude of $u' < 0$ appears to be independent of the magnitude of $v' > 0$. This is seen even more clearly when the joint PDF is weighed by u'^2 (Figure 3.10). Therefore, high speed streaks tend to be shorter than low speed streaks (Figure 3.9b).

The difference in correlation with v' between $u' < 0$ and $u' > 0$ is explained as follows: A high magnitude of $v' < 0$ near the wall indicates that the fluid is from a region far away from the wall and will therefore generate high $u' > 0$. On the other hand regions with $v' > 0$ pump low-speed fluid from a rather uniform bed of low-speed fluid (Figure 3.11).

High-speed streaks tend to be wider than low-speed streaks because the fluid moving toward the wall is redirected in the spanwise direction by the streamwise vortices and the wall. A spanwise movement of high-speed fluid will generate a wider region of $u' > 0$ while a spanwise motion of low-speed fluid near the wall does not generate $u' < 0$ (outward motion does).

3.3 Near-wall shear layers

When the vortices eject low-speed fluid away from the wall, a strong shear layer develops between the low-speed fluid and the high-speed fluid it replaces. Thin regions of $\frac{\partial u'}{\partial y} \ll 0$ are therefore seen on top of low-speed fluid (Figure 3.12). The abundance of shear layers protruding from the wall in transverse views of turbulent boundary layers was reported by Jimenez, Moin, Moser and Keefe (1988). Johansson, Her and Haritonidis (1987) pointed out that shear layers have long life times. Together with the high-speed streaks, the shear-layers contain the strongest vorticity fluctuations (ω'_z) in a TBL. Robinson (1991) observed that these shear-layers could "shed" spanwise vortices. This is not believed to be a significant event for the near-wall turbulence which is the region studied in this work.

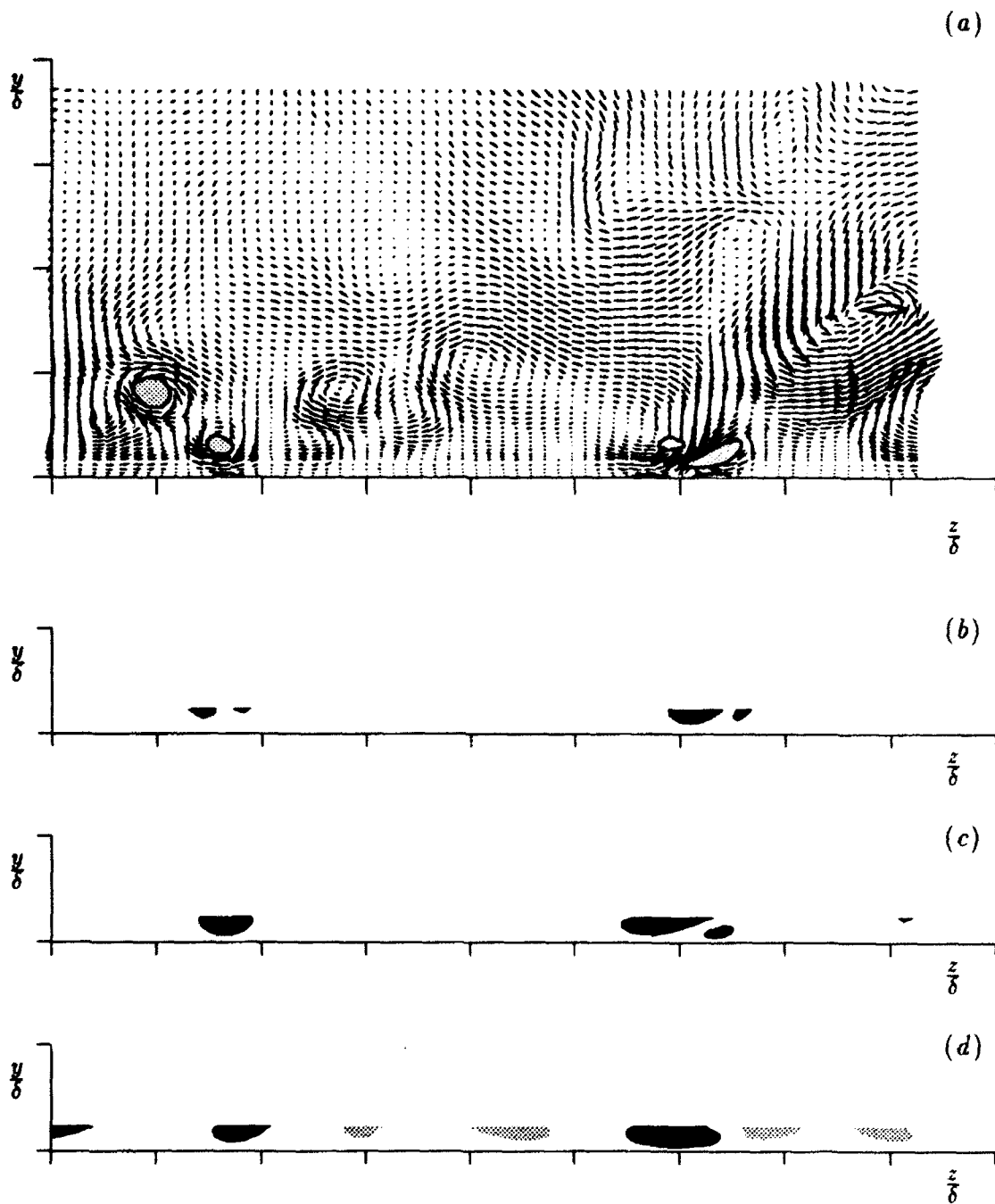


FIGURE 3.1. (a) Sample of velocity field and regions of $|\omega_x| > 60u_\tau/\delta$ (grey). (b) regions below $y^+ = 10$ in (a) with $|v| > 0.5u_\tau$, (c) $|w| > u_\tau$ and (d) $u' > 2u_\tau$ (black) and $u' < -2u_\tau$ (grey). The Figure demonstrates that vortices closest to the wall generate the most intense $|v|$, $|w|$ and $u' > 0$, but not always the most intense $u' < 0$. Tic mark are spaced 0.25 apart.

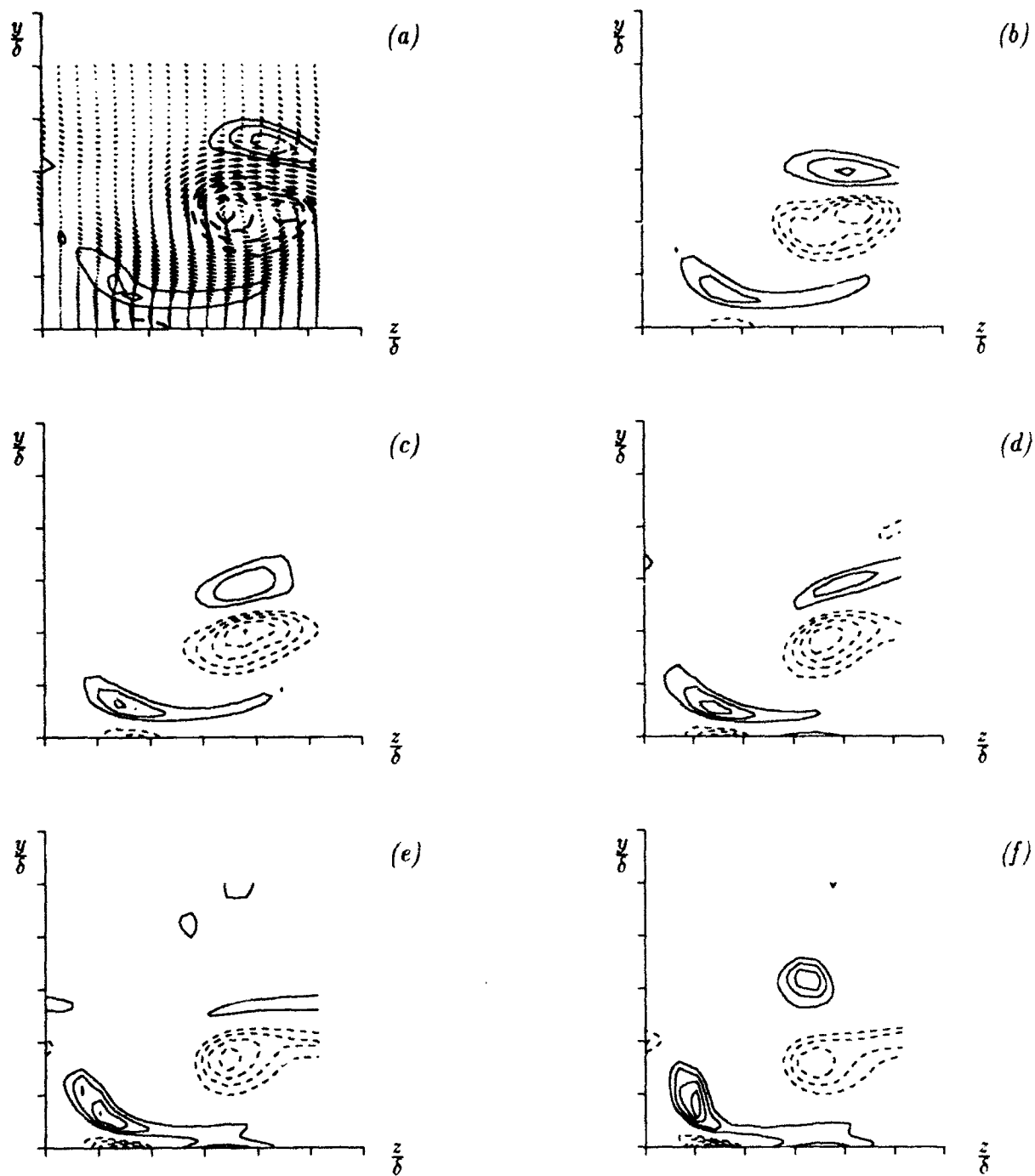


FIGURE 3.2. Time evolution of contours of ω_x in coordinates moving with the structures. Increment is $0.25u_L/\delta$ starting with $0.5u_L/\delta$ (—) and $-0.25u_L/\delta$ starting with $-0.5u_L/\delta$ (----). Velocity vectors are included for the first frame. Tic marks are 0.2 apart. The time sequence is *a, b, c, d, e, f*.

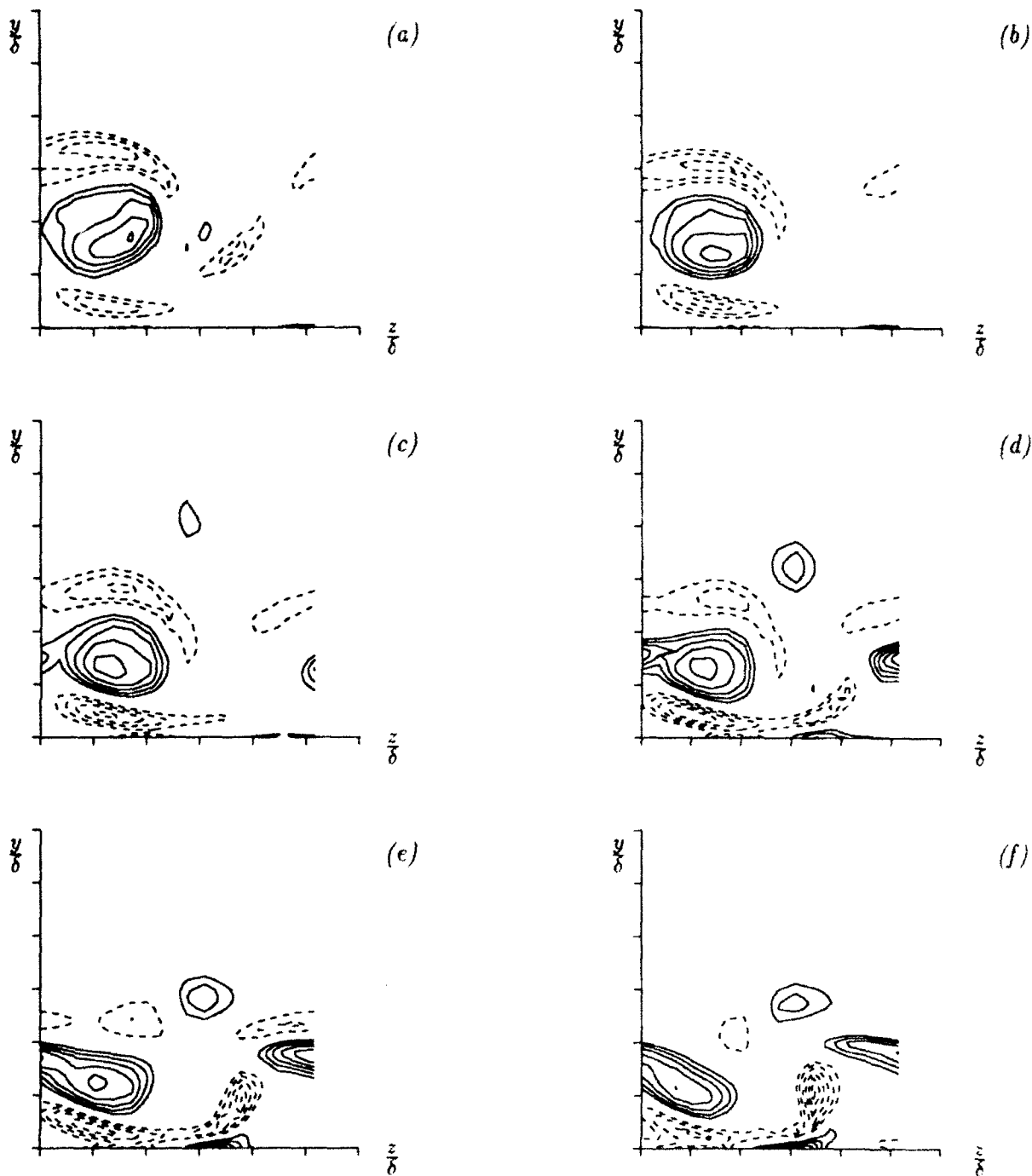


FIGURE 3.3. Time evolution of front part of the vortex formed in Figure 3.2. Contour levels are the same. First frame corresponds to last frame in Figure 3.2. The time sequence is a, b, c, d, e, f .

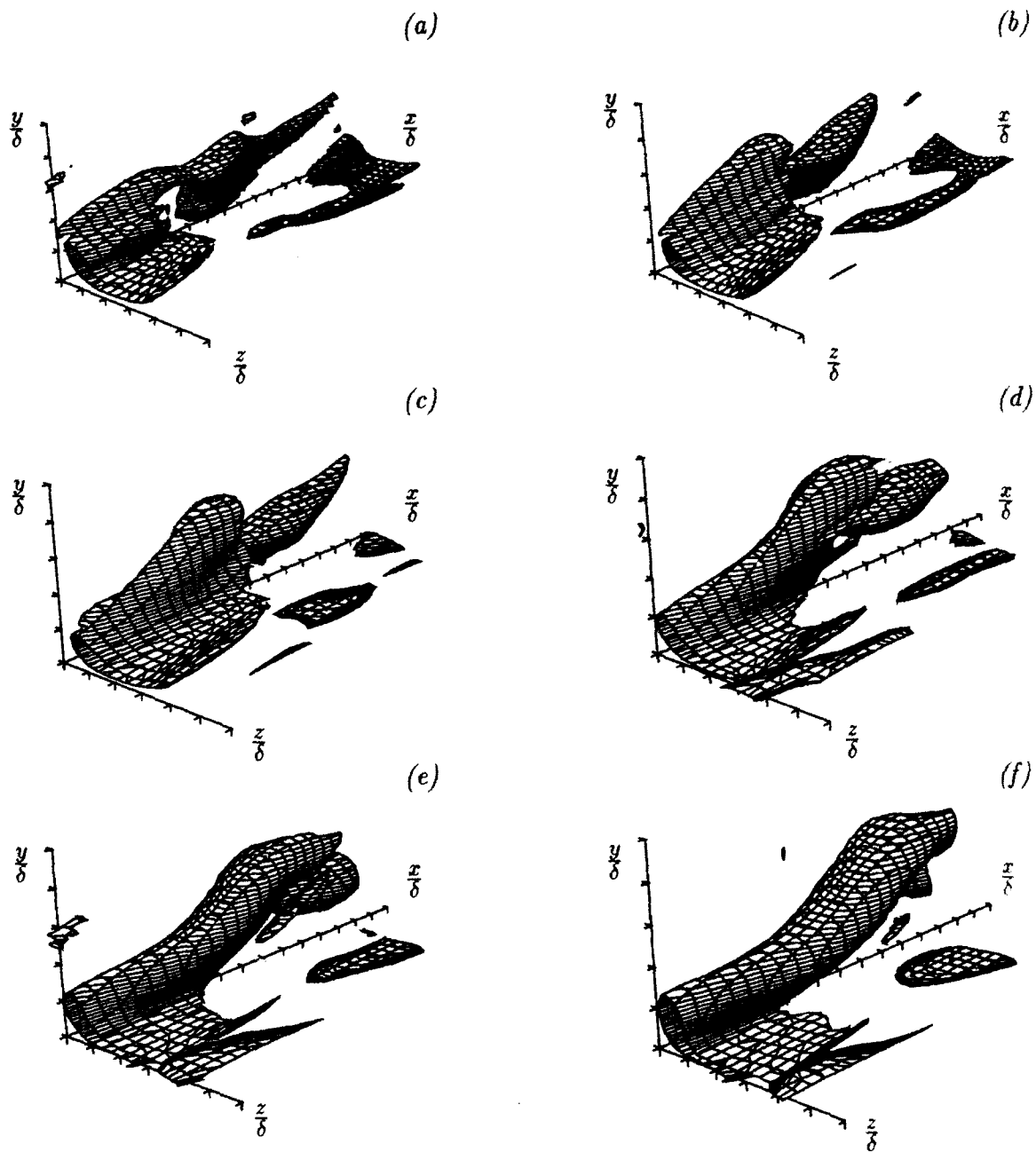


FIGURE 3.4. Time evolution of contours of $\omega_x = 0.5u_L/\delta$ in coordinates moving with the structures. The $z - y$ cuts across the contour surfaces are also seen in Figure 3.2. Tickmarks are 0.2 apart. The time sequence is a, b, c, d, e, f .

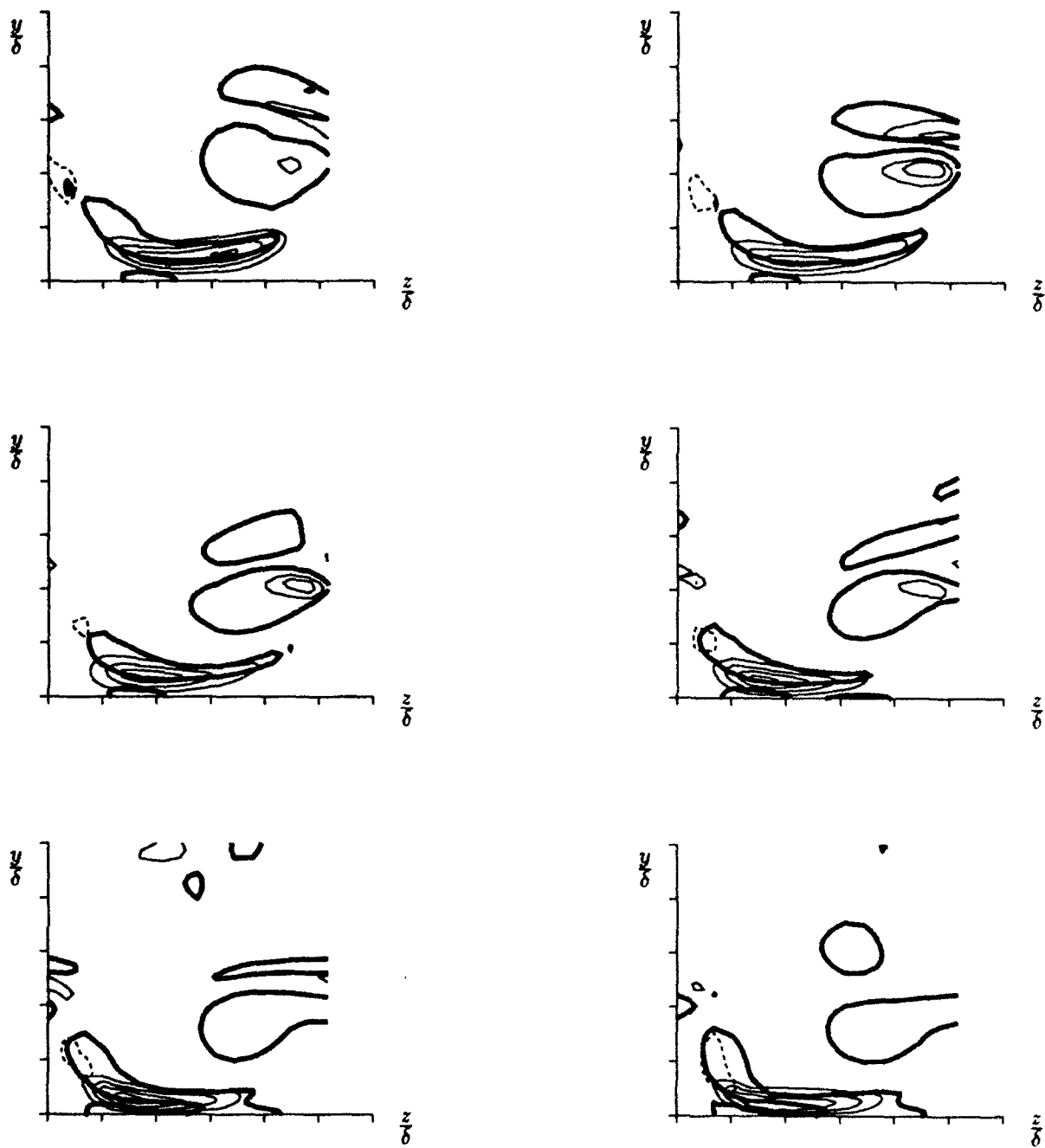


FIGURE 3.5. Components of tilting terms for the streamwise vorticity associated with the vortex formation in Figure 3.2. Contour levels of $-\frac{\partial w}{\partial x} \frac{\partial u}{\partial y}$ (—) and $\frac{\partial v}{\partial x} \frac{\partial u}{\partial z}$ (----) start at $0.05(u_L/\delta)^2$ and increment is $0.05(u_L/\delta)^2$. Contour level of $|\omega_x|$ is $0.5u_L/\delta$ (—). Tic marks are 0.2 apart.

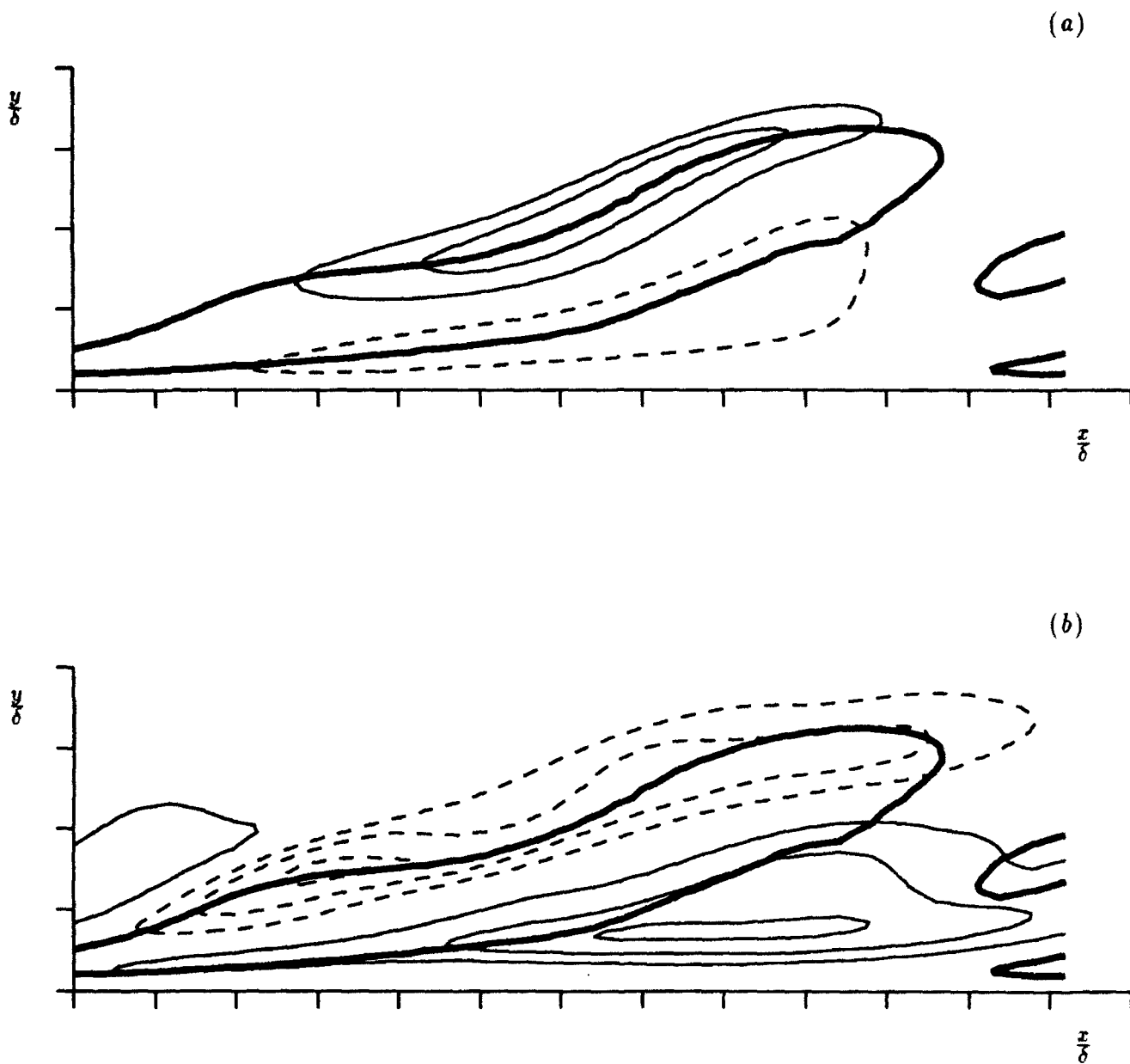


FIGURE 3.6. Horizontal gradients associated with a tilted near-wall vortex. Contours of $\omega_x = 0.5u_L/\delta$ (—) show the newly formed vortex in the last frame in Figure 3.4. Iso-contours of positive (—) and negative (----) values of (a) w and (b) u' are inclined due to the tilting of the vortex. Tic marks are spaced 0.25 apart.

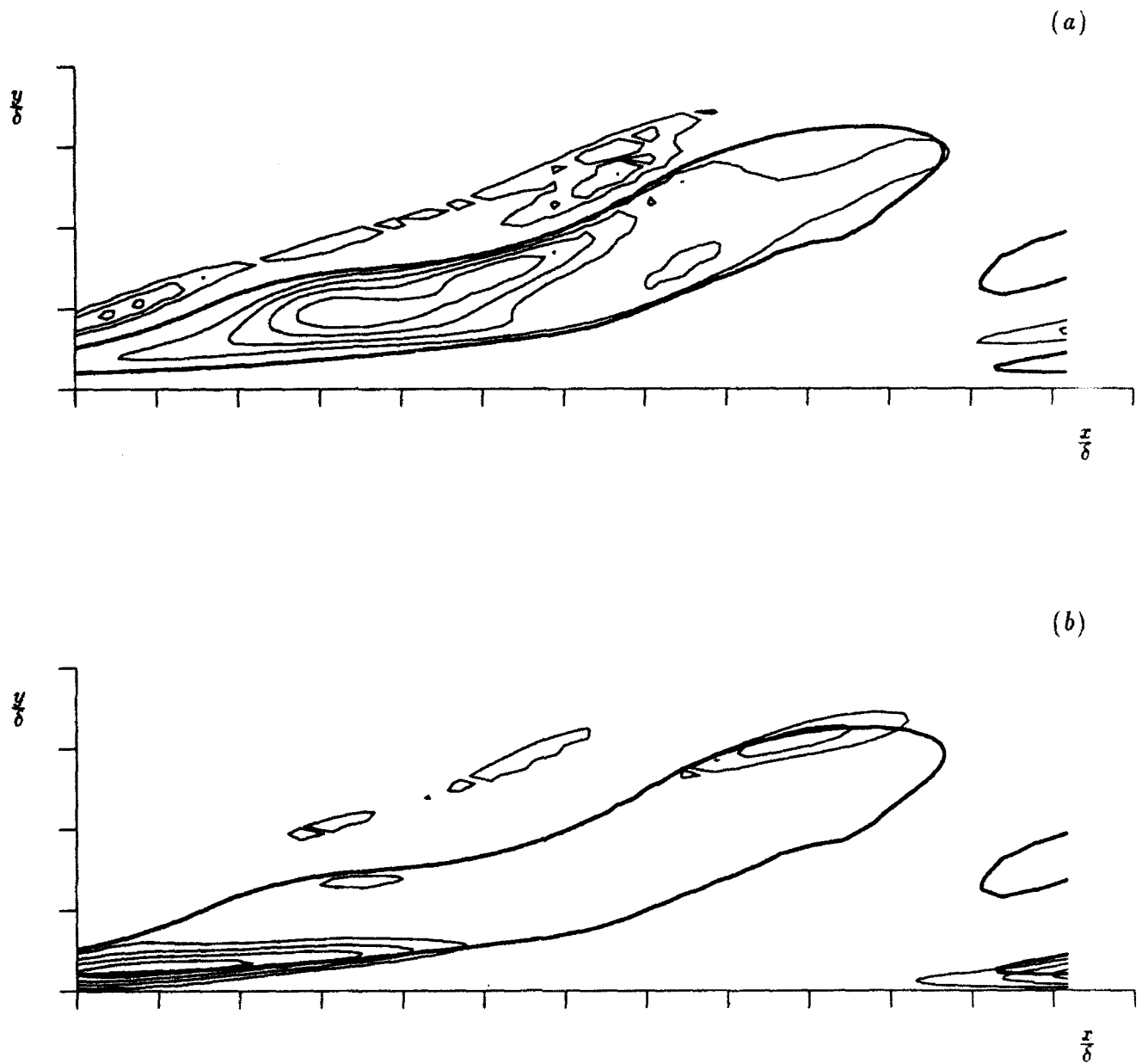


FIGURE 3.7. Tilting and stretching terms within a vortex. Contours of $\omega_x = 0.5u_L/\delta$ (—) show the same vortex as in Figure 3.6. Isocontours of (a) $\omega_x \frac{\partial u}{\partial x}$ and (b) $\omega_y \frac{\partial u}{\partial y} + \omega_z \frac{\partial u}{\partial z}$ with increment u_L^2/δ^2 starting with u_L^2/δ^2 .

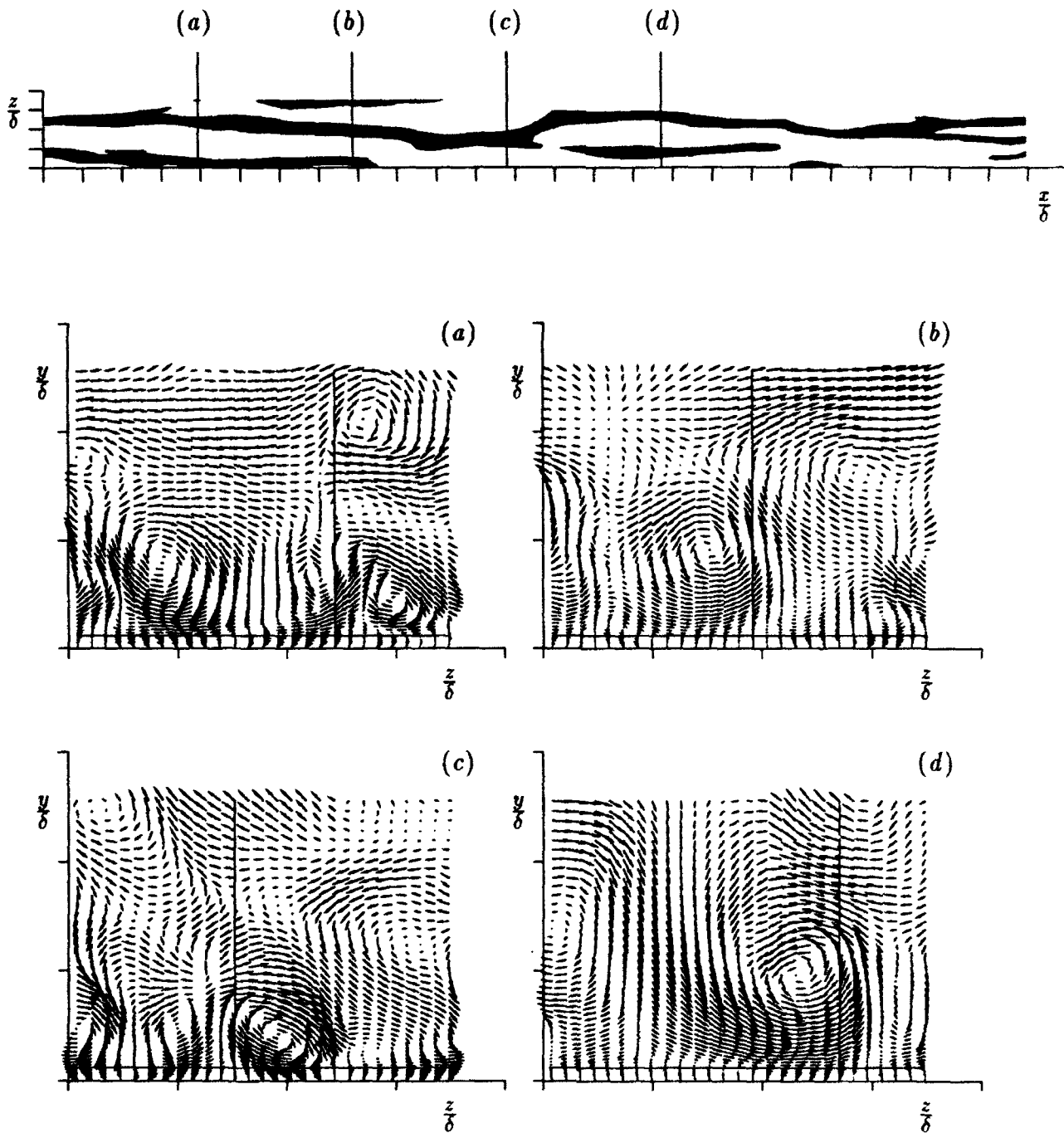


FIGURE 3.8. Velocity vectors in vertical planes along a randomly chosen low-speed streak at $y_{2D}^+ = 5$ (top, black: $u' < -u_\tau$). Vertical lines show the location of the long low-speed streak in the top figure. The horizontal lines is the plane of the streak ($y^+ = 5$). This illustrates that streaks are maintained by a system of staggered vortices. Tic marks are 0.25 apart except on the horizontal axis of the top figure where they are 0.5 apart.

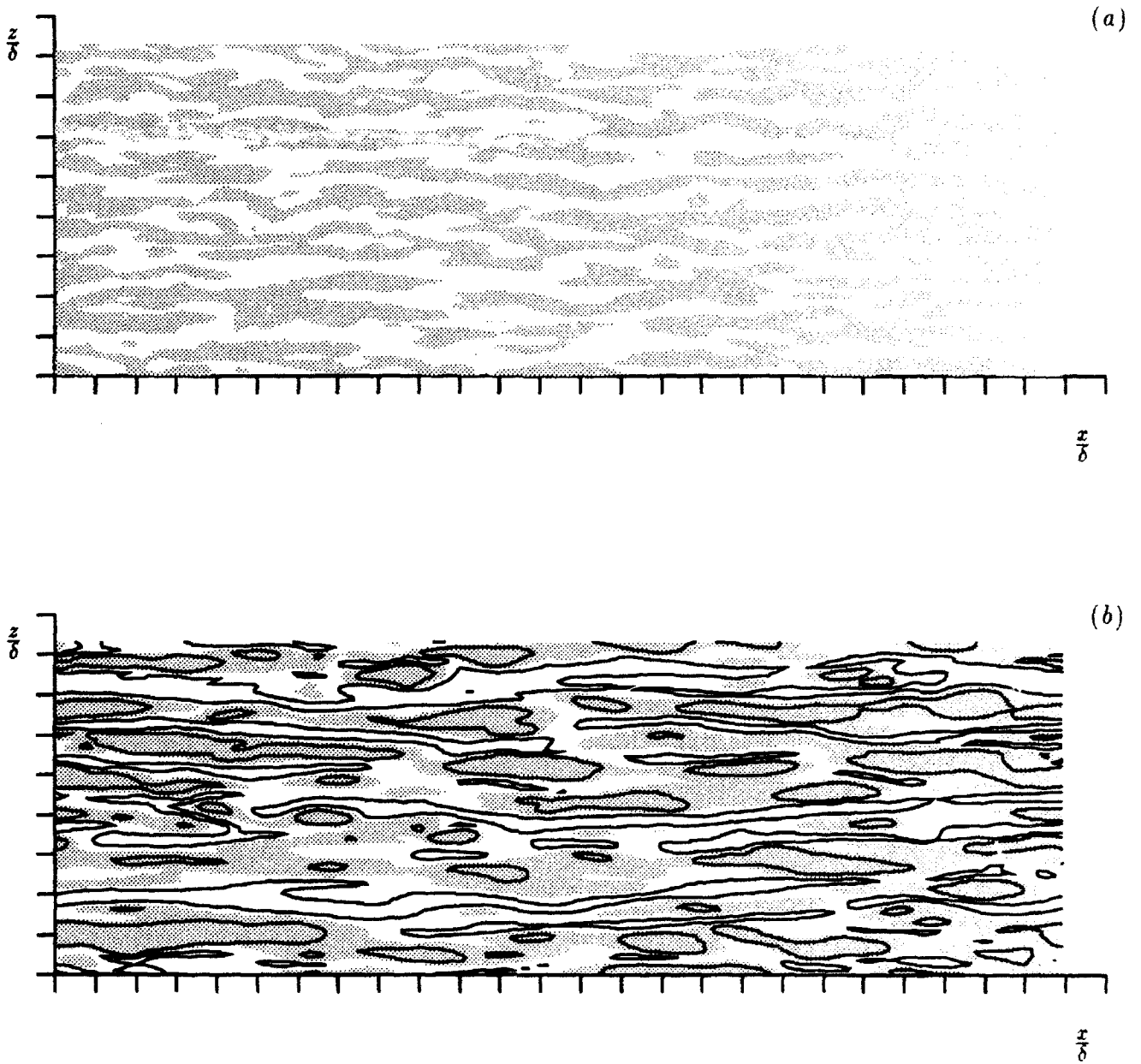


FIGURE 3.9. (a) Regions of positive v (grey) at $y_{2D}^+ = 5.4$. In (b) grey represent $u' > 0$ and the lines are contours of $u' = \pm 1.5u_\tau$. The contours of $u' < -1.5u_\tau$ are longer and thinner than those of $u' > 1.5u_\tau$. Tic marks are 0.5 apart.

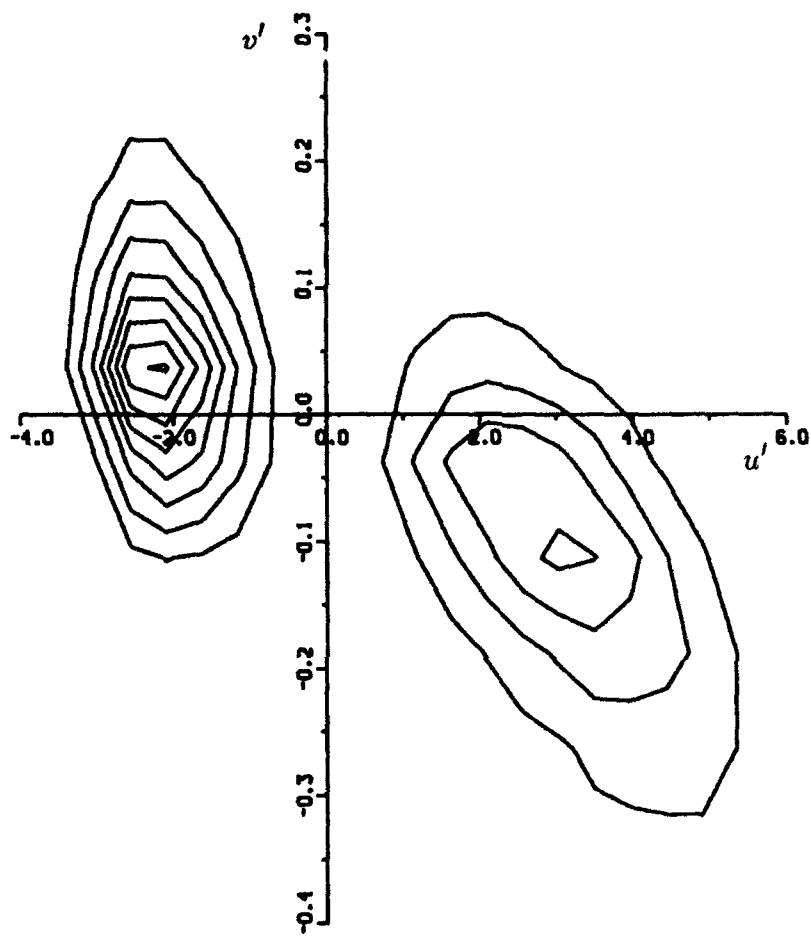


FIGURE 3.10. Contours of the joint PDF between u' and v' weighted by u'^2 at $y^+ = 5$ show that $u' < 0$ is uncorrelated with $v' > 0$ (vertically elongated contour lines) while $u' > 0$ is correlated with $v' < 0$ (tilted contour lines).

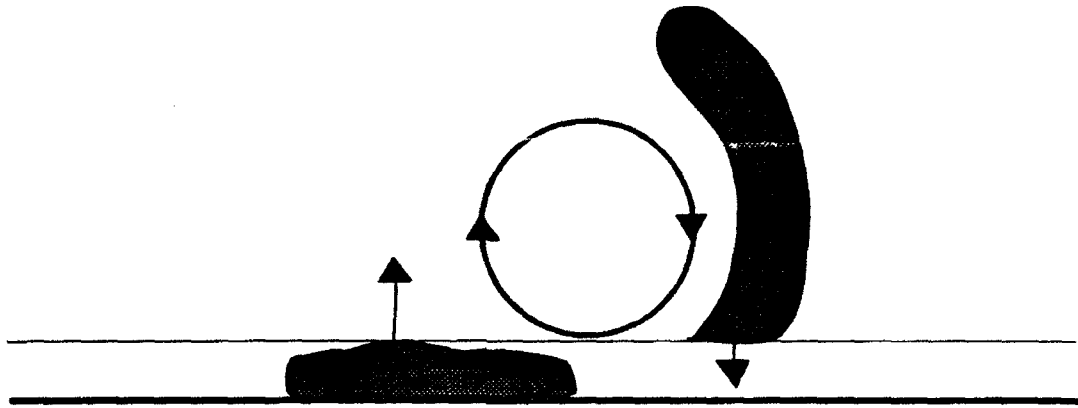


FIGURE 3.11. Schematics showing the regions of origin for fluid crossing $y_{2D}^+ = 5$ over a time Δt . The region of fluid swept toward the wall originate from regions extending across the mean velocity gradient while the ejected fluid originates from a region extending in the horizontal directions.

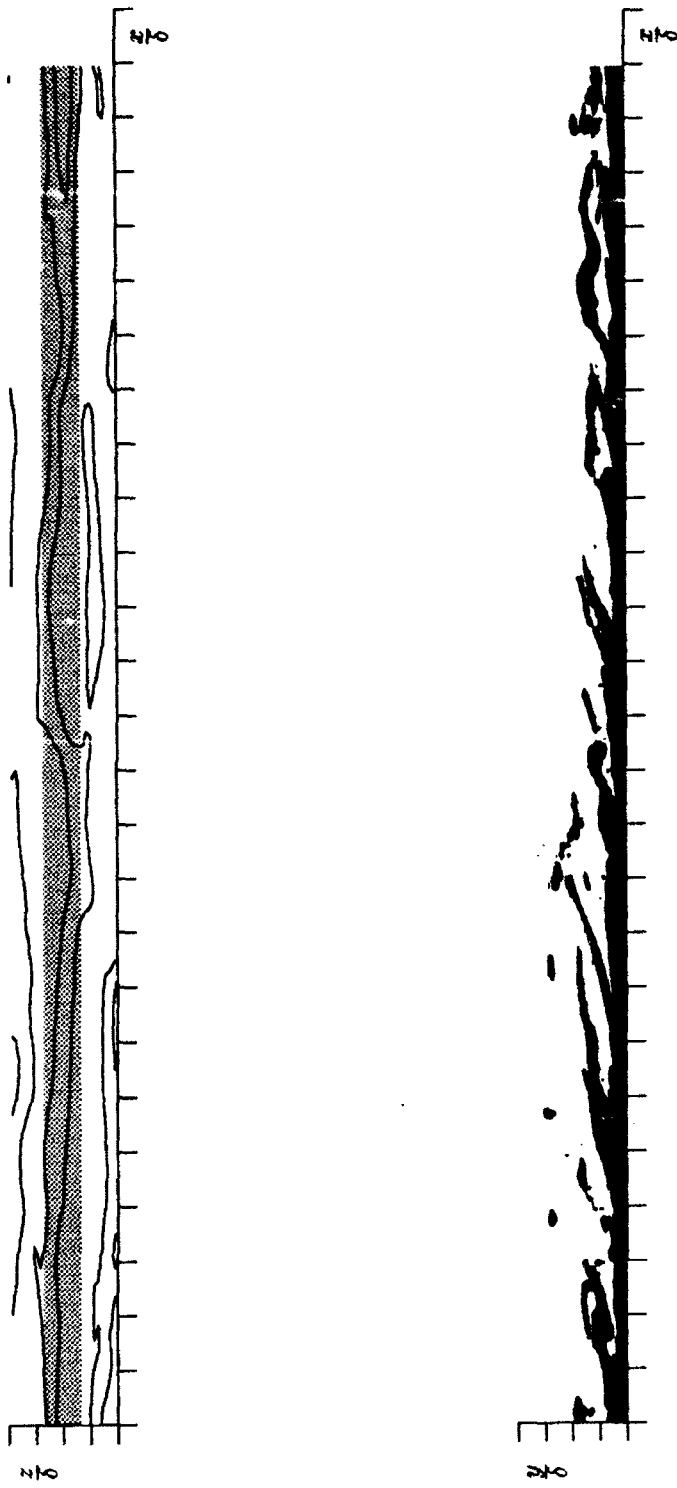


FIGURE 3.12. (a) Superposition of regions with $\omega'_2 < -40$ in $x - y$ planes across a streak displays the presence of shear layers on top of a low speed streak. (b) lines represent $u' = -u_r$ and the grey area show the region over which the shear layers are accumulated in (a). Tic marks are 0.5 apart on the horizontal axes and 0.25 apart on the vertical axes.

CHAPTER 4

RESULTS AND DISCUSSION

The statistics of the 3D flow studied here were reported by Moin *et al.* (1990). They found a reduction in the total Reynolds shear stress (Figure 4.1), turbulent kinetic energy, and the structure parameter, a_1 . The reduction in turbulent kinetic energy was due to a large decrease in $\overline{u'^2}$ and a smaller decrease in $\overline{v'^2}$ (Figure 4.2a). In coordinates aligned with the Reynolds shear stress direction (see eqn. 2.1b), the spanwise intensity was almost unchanged (Figure 4.2b). The Reynolds stress budgets showed that a reduction in the production terms caused the drops in $\overline{u'^2}$ and $-\overline{u'v'}$ while a reduction in $-\overline{v'\frac{\partial p'}{\partial y}}$ caused the drop in $\overline{v'^2}$, which does not have a production term. The Reynolds shear stress angle lagged behind the mean velocity gradient angle.

In this chapter, the mechanics underlying these changes are described. Emphasis will be placed on the evolution of the six Reynolds stresses, however, evolutions of the mean velocities (§4.3), vorticity intensities (§4.4) and the two-point correlations (§4.5) are also discussed. The present results will be compared with the experimental data and the underlying mechanisms suggested in the literature (§4.6).

It is known (see Chapter 3) that the quasi-streamwise vortices are the primary contributors to the Reynolds shear stress in 2D boundary layers. The dynamics associated with these vortices will therefore be studied in detail. It turns out that the flow dynamics associated with positive and negative streamwise vortices (the same sign as or opposite to the mean streamwise vorticity) are different. In this work the sign of a streamwise vortex will be defined as that of the streamwise vorticity fluctuation in the center of the vortex. The mean x -vorticity is positive in the present flow due to the direction of the imposed spanwise pressure gradient (Figure 4.3).

It will be shown below that the key mechanisms for the reduction in the Reynolds stresses in the 3D flow are :

- I Fluid swept toward the wall by positive vortices will not get as close to the wall in 3D as in 2D, and will therefore generate less Reynolds stresses. In coordinates moving with the vortex in the spanwise direction, the fluid will be forced toward the vortex-center and will therefore experience a lower vortex-induced vertical velocity (Figure 4.4a).

II Ejections by negative vortices generate less intense velocity fluctuations because the lifted fluid originates at a higher distance from the wall in 3D (Figure 4.4*b*). These ejections will also experience higher viscous forces leading to higher dissipation in the turbulent kinetic energy equation.

These are the only significant mechanisms during the early evolution of the flow. Later two other mechanisms contribute significantly to the reduction of the Reynolds stresses. These are:

III The streamwise vortices are shifted with respect to the wall layer streaks below them. In the new configuration, the vortices pump high- rather than low-speed fluid away from the wall. In addition, the flow trajectories are altered with adverse effect on the Reynolds shear stress (Figure 4.4*c*).

IV The high speed fluid swept toward the wall by negative vortices is convected away from the vortex in the spanwise direction by the spanwise mean flow and does not reach as close to the wall as in 2D (Figure 4.4*d*).

Since the effect of the spanwise pressure gradient diffuses outward from the wall in this flow (see §2.5), it is useful to study the initial and later responses separately. The initial period is defined as the time when the spanwise boundary layer edge is below $y_{2D}^+ = 20$ (y^+ based on 2D wall stress). The quasi-streamwise vortices are mostly outside the spanwise boundary layer and the flow is still very similar to a 2D channel flow. Comparison of the 2D and 3D flows is therefore much easier than at later times and 3D effects can be readily identified. One of the difficulties in studying the flow during the later period is that there is no obvious choice of coordinates in which a comparison with the 2D flow can be made (see §2.1).

4.1 Reynolds stresses during the initial period.

For some time after $\frac{\partial P}{\partial z}$ is imposed, most of the streamwise vortices will be outside the spanwise boundary layer. They will then convect in the spanwise direction without turning. A study of the instantaneous flows showed that this lasts for a time $0.3\delta/u_{\tau 2D}$ when $\frac{\partial P}{\partial z} = -10$ (unless otherwise stated all quantities are normalized with the 2D wall shear velocity, $u_{\tau 2D}$, and the channel half width, δ). This is the time it takes the spanwise boundary layer to reach the average location of the centers of the near-wall vortices, $y_{2D}^+ = 20$. The lack of turning at $t=0.3$ can be seen in Figures 4.5 *a* and *b*, where contours of ω'_x of magnitude $60u_{\tau 2D}/\delta$ (which in §3.1.2 were found to capture

vortices fairly well) and $|\frac{\partial u'}{\partial y}| > 50$ at the wall are shown for the two companion flows described in §2.7. The two simulations were started from the same 2D initial field $t = 0.3$ earlier. Both vortices and streaks have been convected in the spanwise direction, but their shapes have not been altered significantly by the spanwise pressure gradient. However, the turbulence statistics have been significantly changed within the viscous sublayer. The total Reynolds shear stress does not play an important role in the viscous sublayer, but a drop of about 10% in this region indicates that a significant change in turbulence mechanics has already occurred. In this section, the mechanics causing the altered statistics at $t=0.3$ will be discussed, and it is assumed that the mechanics is the same at earlier times.

The investigation of the six Reynolds stresses will be done in two steps. First, for each Reynolds stress the events which are contributing most to its change are identified. This is done using probability density functions and quadrant/octant-analysis as well as the companion flows method (§2.7). Second, these events are studied in detail and their underlying mechanics are identified.

The percentage changes in the Reynolds stresses are used to identify the locations where each stress is most affected. At $t=0.3$, all three intensities have decreased across the 3D layer. The streamwise intensity, $\overline{u'^2}$, has dropped by 2% at its maximum location, $y_{2D}^+ \approx 15$, and the maximum percentage drop is 8% at $y_{2D}^+ \approx 4$ (Figure 4.6). The vertical velocity intensity, $\overline{v'^2}$, has a maximum percentage drop of 9% at $y_{2D}^+ \approx 12$ while the spanwise intensity, $\overline{w'^2}$, has a maximum reduction of 9% very near the wall (Figures 4.7, 4.8). The streamwise Reynolds shear stress, $-\overline{u'v'}$, has been reduced by 5% at its maximum location ($y_{2D}^+ \approx 30$) and the maximum percentage drop is 13% very close to the wall (Figure 4.9a). The spanwise Reynolds shear stress, $\overline{v'w'}$, has become slightly negative with its maximum magnitude at $y_{2D}^+ \approx 10$ and the ratio of spanwise to streamwise eddy-viscosity is 0.3 across the viscous sub-layer. Finally, $\overline{u'w'}$ has become slightly positive with a maximum value at $y_{2D}^+ \approx 10$ which is ten times the local $\overline{v'w'}$ -magnitude and half the local $\overline{u'v'}$ -magnitude (Figure 4.1a).

4.1.1 Probability density functions, octant- and quadrant analysis

The intensity-weighted PDFs, $u_i'^2 P(u_i')$, show which ranges of velocity fluctuation levels are contributing most to the aforementioned reductions. They are shown in Figure 4.10 near the y -locations of maximum percentage changes, but the trend is virtually the same across the viscous sublayer. The streamwise intensity is reduced

due to a reduction of the most negative and medium-range positive u' while the vertical intensity is reduced due to reductions of medium-range positive and negative v' . Medium-range positive w' and a wide range of negative values causes the drop in the spanwise intensity. The asymmetry of the weighted PDF for $\frac{\partial w'}{\partial y}$ at $t=0.3$ may indicate that vortices of opposite sign are affected differently. Note that the PDF of w' very near the wall is proportional to that of $\frac{\partial w'}{\partial y} \Big|_w$.

According to the quadrant analysis (Figure 4.11), the weakening of the events in the second quadrant, $u' < 0$ with $v' > 0$ and in the fourth quadrant, $u' > 0$ with $v' < 0$, contribute about equally to the reduction in $-\overline{u'v'}$.

The octant analysis (Figure 4.12) gives key information about the location of weakened events (Simpson & Devenport 1990). It shows that in the viscous sublayer the reduced quadrant-2 events tend to be correlated with positive w' while the reduced quadrant-4 events tend to be correlated with negative w' . Since w' is mostly associated with streamwise vortices in this early time-period, this indicates that those quadrant-2 events that are weakened are generated by negative vortices while reduced quadrant-4 events tend to be generated by positive vortices (see Figure 4.3). This is in accordance with mechanisms I and II presented earlier in this chapter. Outside the spanwise TBL, the octants with $u'v' < 0$ and $w' > 0$ are most reduced. The octant analysis does not provide enough information to establish the sign of the vortices which generate these weakened events, since in this region these events may be below or above the vortex-centers. Figure 4.13 shows that the same two octants are responsible for the reduction in the velocity intensities as well.

The weighted joint PDFs between u' and w' at $y_{2D}^+ = 10$ (Figure 4.14) show that the increase in $\overline{u'w'}$ is due to a reduction of the most negative u' correlated with positive w' , and of medium-range positive u' correlated with negative w' . This is consistent with the octant analysis for $\overline{u'v'}$. The quadrant analysis (Figure 4.15) shows that both quadrants which generate negative $u'w'$ contribute significantly to the increase in $\overline{u'w'}$. The regions of reduced positive and negative u' are therefore causing the change in this Reynolds stress as well.

The weighted joint PDFs between v' and w' at $y_{2D}^+ = 10$ (Figure 4.16) show that the negative $\overline{v'w'}$ is due to a reduction of intense positive and negative v' correlated with intense w' of the same sign (quadrant 1 and 3). This is supported by the quadrant analysis (Figure 4.17). The reduced values of w' are well correlated with the reduced values of v' . Therefore, negative $\overline{v'w'}$ is generated due to the *weakening* of certain

events which is very different from the mixing mechanism typically advanced for generation of negative $\overline{u'v'}$. It is for this reason that eddy viscosity models can not predict, at least, the early stages of three-dimensionality. It should be noted that the mechanisms associated with events **I** and **II** (Figure 4.4) described earlier have now also been identified with generation of $\overline{u'w'}$ and $-\overline{v'w'}$.

4.1.2 The companion flows method

The comparison of the two companion flows (see §2.7) will now be used to confirm and expand these findings. Regions with $|u'| > 2$, which according to the PDF of u' are most affected by the spanwise pressure gradient at $y_{2D}^+ = 5$, are shown for the two flows in Figure 4.18. The 3D flow field has been moved in the negative z -direction to account for the spanwise convection so the two fields become easier to compare. The shifted streamwise fluctuations will be denoted by \tilde{u}' , where $\tilde{u}'(x, z) = u'(x, z + l)$ and $l = l(y, t)$ is the spanwise length that the 3D flow has been convected. l was found by comparing u' in the two instantaneous flow fields at one x -location (Figure 4.19). It can be seen that the two flows are very similar. In order to identify the subtle events causing the changes in the statistics, the regions which contribute most to the change in $\overline{u'^2}$ are located. These are defined as the regions where $\tilde{u}'_{3D}{}^2 - u'_{2D}{}^2$ is most negative. In Figure 4.20, contours of the most negative $\tilde{u}'_{3D}{}^2 - u'_{2D}{}^2$ at $y_{2D}^+ = 5$ are shown. The plot also shows the sign of w'_{2D} (\tilde{w}'_{3D} has mostly the same sign as its 2D counterpart). It can be seen that the regions which have a reduction in $\overline{u'^2}$ are well correlated with w' with sign opposite to u' (mechanism **I** & **II**). A corresponding plot which showed the sign of v' instead indicated that the reduced u' -regions correlate well with v' of opposite sign. Figure 4.21 shows the regions which contribute most to the reduction of each of the velocity intensities. It indicates that the events which cause the reduction in $\overline{u'^2}$ are also causing the reduction in $\overline{v'^2}$ and $\overline{w'^2}$.

The vortices which are associated with reduced u' can be seen in $z - y$ planes cut through the regions identified in Figure 4.21. In almost every case the reductions in positive u' were associated with positive vortices and the reductions in negative u' were associated with negative vortices. The strengths and locations of the vortices varied, but most were located between $y_{2D}^+ = 20$ and 40 and were of low or medium-range strengths. A sample of each of the vortices and the corresponding patches of the affected velocity regions are shown in Figures 4.22 and 4.23 in coordinates moving with the vortices in the spanwise direction.

The Reynolds stresses are altered at $t=0.3$ because near-wall vortices produce less intense velocity fluctuations. When these vortices have a positive sign of rotation, they tend to generate reduced $u' > 0$, $v' < 0$ and $w' < 0$ (sweep), and when they have a negative sign they tend to generate reduced $u' < 0$, $v' > 0$ and $w' > 0$ (ejection). This causes the velocity intensities and $-\overline{u'v'}$ to be reduced and $-\overline{v'w'}$, $\overline{u'w'}$ to become positive (§4.2.1). The mechanisms underlying these changes will now be discussed.

Particle trajectories about negative vortices

When fluid particles enter the viscous sublayer, their paths will be affected by the spanwise mean velocity gradient. This change in trajectory is linked to the alteration of the Reynolds stresses. *In what follows it is most convenient to consider the equivalent flows where the flow becomes 3D due to a spanwise acceleration of the walls (eqn. 2.5.7), because then the vortices will not move significantly in the spanwise direction.* “Streamlines” within the $z - y$ plane ($\frac{dy}{dz} = \frac{v}{w}$) will therefore indicate how the particle paths are affected by the spanwise TBL. Figure 4.24 shows “streamline”-segments for the sample-vortices in Figures 4.22 and 4.23. Lines for both companion flows are shown together, traced to or from a common point. The discussion below is based on these figures.

In 2D, vortices with a negative sign of rotation will move fluid particles in the positive z -direction below their centers. In 3D this motion is opposed by the spanwise mean flow. If a fluid particle is sufficiently close to the vortex-center, it will encounter a small spanwise mean motion and will have sufficient momentum to move in the positive z -direction and be ejected as in 2D. However, a fluid particle which in 2D moves down close to the wall and is then ejected (and generates $u' \ll 0$), will be redirected by the moving wall and dragged away from the vortex along the wall (see also sketch in Figure 4.4b). In 3D the fluid which is ejected by the vortex is convected toward the vortex by the moving wall and will tend to originate further away from the wall than the fluid ejected in 2D (Figure 4.24b). Recall that the PDF's of u' indicated that the most negative values of u' were most affected in 3D. Such large negative values are generated by fluid originating from the closest proximity of the wall. In Figure 4.24b the fluid particles originating below the vortex and closest to the wall are swept to the left in 3D and are not shown. Only “streamlines” near the region of significant reduction in the magnitude of u' are shown. The strongest

vortices close to the wall at $t=0.3$ are able to move fluid in the positive z -direction below $y_{2D}^+ = 5$ as well as lifting fluid convected toward them. They will therefore generate intense $u' < 0$ in 3D as in 2D. In 2D these streamlines originate from below the vortex and in 3D they originate from the far right of the vortex.

Moin *et al.* (1990) reported a higher dissipation of turbulent kinetic energy in 3D. This appears to be due to the spanwise convection of the ejected low-speed fluid over high-speed fluid regions and thereby increasing the magnitude of $\frac{\partial u'}{\partial y} < 0$ (Figure 4.25). As will be shown later, the probability density function of vorticity fluctuations show that the probability of large negative $\frac{\partial u'}{\partial y}$ increases significantly.

Particle trajectories about positive vortices

Vortices with a positive sign of rotation will in 2D move fluid toward the wall in the negative z -direction below their centers. In 3D the spanwise TBL will drag this fluid toward the vortex-center, where the vortex-induced vertical motion is lower. Therefore, it will not reach as close to the wall as in 2D (Figure 4.24a, 4.4a). This reduces the magnitudes of both positive u' and negative v' . The large values of w' near the wall are due to redirection of the fluid swept toward the wall. Therefore, the reduction of negative w' close to the wall is consistent with this scenario.

This concludes the dynamics of near-wall fluid motions associated with positive and negative vortices. In addition, as seen in Figure 4.9 the $-\overline{u'v'}$ is also reduced outside the spanwise boundary layer. The same approach was followed in order to identify the regions of reduced $-\overline{u'v'}$ in the outermost spanwise boundary layer. At $y_{2D}^+ = 25$, the regions where $-\overline{u'v'}$ were most reduced were found to correlate well with $w' > 0$ which is consistent with the octant analysis. Vertical cuts through regions of reduced quadrant-2 events show that they are associated with negative vortices with centers further away from the wall (such that $w' > 0$ below them, see sketch in Figure 4.26). In the same way it was found that the reduced quadrant-4 events at $y_{2D}^+ = 25$ were associated with positive vortices with centers closer to the wall ($w' > 0$) (see sketch in Figure 4.26 & Figure 4.27). The signs of the vortices which are associated with reductions in these quadrants are therefore the same across the TBL. That is, negative vortices are associated with quadrant 2 reductions and positive vortices with quadrant 4 reductions. The vortices linked to the reduced quadrant-4 events tend to be closer to the wall than those linked to reduced quadrant-2 events (see sketch in Figure 4.26).

4.2 Reynolds stresses during the later period of three-dimensionality

After $t \approx 0.3$, the flow becomes more obviously three-dimensional in the sense that the streamwise vortices start to turn in the direction of the mean spanwise pressure gradient. The vortices closest to the wall become submerged in the spanwise boundary layer. Figure 4.28 shows surfaces of streamwise vorticity fluctuations equal to $60u_{\tau 2D}/\delta$ (which in §3.1.2 were found to adequately capture streamwise vortices) at $t=0.45$ and $t=0.60$. Contours of $|\frac{\partial u'}{\partial y}| > 50$ at the wall are also included to show the streaks. The turning of vortices makes the flow more difficult to analyze, because the vortices now contribute to all the Reynolds stresses. In 2D, u' is mostly generated due to transport of high or low speed fluid in the vertical direction by the vortices whereas v' and w' are mostly due to the swirling motion. Because the vortices have varying turning angles according to their size and distance from the wall, it is impossible to find a unique coordinate system for comparison of the 2D and 3D flows using the companion flows technique.

4.2.1 Changes in the Reynolds stresses

At $t=0.9$, the velocity intensity in the initial mean flow direction, $\overline{u'^2}$, reaches its maximum percentage drop of 28% at $y_{2D}^+ \approx 8$ and recovery starts at the wall (Figure 4.6a). When the coordinates are rotated to keep the streamwise intensity at a maximum (eqn. 2.1d), $\overline{u_*'^2}$ starts to recover at $t=0.6$ and the maximum percentage reduction is 19% (Figure 4.6b). The vertical intensity, $\overline{v'^2}$, starts a slow recovery near the wall soon after $t=0.3$ (Figure 4.7). At $t=0.9$, the vertical intensity has almost recovered to its initial values near the wall, while at $y_{2D}^+ \approx 40$ it reaches a maximum percentage reduction of 19%. The spanwise intensity, $\overline{w'^2}$, increases rapidly after $t=0.3$ (Figure 4.8). In coordinates rotated to keep the spanwise intensity at a minimum (eqn. 2.1d), $\overline{w_*'^2}$ remains slightly lower than the 2D profile in the time-period studied (Figure 4.2b). The turbulent kinetic energy reaches a maximum percentage drop of 17% at $t=0.7$ and $y_{2D}^+ \approx 10$ and then starts to recover. The Reynolds shear stress, $-\overline{u'v'}$, attains its maximum percentage drop of 23% at $y_{2D}^+ \approx 30$ and $t=0.9$ (Figure 4.6a). The total Reynolds shear stress, $\sqrt{\overline{u'v'^2} + \overline{v'w'^2}}$, which is invariant with respect to coordinate rotation, reaches a maximum percentage drop of 21% at $t = 0.8$ (Figure 4.9b). Figure 4.1a shows the increase in the spanwise Reynolds shear stresses $-\overline{v'w'}$ and $\overline{u'w'}$ due to the turning of the structures. $\overline{u'w'}$ should be viewed as

a velocity correlation rather than a shear stress because it does not contribute to the mean momentum equations. The Reynolds shear stress angle where $\overline{v'w'_*} = 0$, eqn. (2.1b), and the intensity angle, where $\overline{u'_*w'_*} = 0$, eqn. (2.1d), are shown in Figure 4.29. It can be seen that the latter angle lags behind the former.

The changes in the turbulence statistics can be attributed to the structural changes, to the rotation of the coordinate system aligned with the streamwise vortices, and to the increased mass flow rate. Coordinate rotation effects can be eliminated by considering quantities which are invariant with respect to coordinate rotation. One may also consider a coordinate system which minimizes the turning effect on the flow quantity being examined. There are two characteristic angles for the Reynolds stresses: the Reynolds shear stress angle, eqn. (2.1b), and the intensity angle, eqn. (2.1d). When the coordinates are rotated with the stress angle, we have $\overline{v'w'_*} = 0$ and $|\overline{u'_*v'}| = \sqrt{\overline{u'v'^2} + \overline{v'w'^2}}$. A rotation of the coordinates with the intensity angle maintains $\overline{u'^2_*}$ at a maximum, $\overline{w'^2_*}$ at a minimum and $\overline{u'_*w'_*} = 0$. In the latter coordinate system, for example, it would be legitimate to compare the 2D and 3D PDFs of streamwise velocity fluctuations. The increased mass flow leads to increased Reynolds stresses and flow recovery.

In the following section the structural changes causing the reduction in the Reynolds stresses will be identified and the underlying mechanisms will be discussed. Most of the studies were conducted at $t=0.6$ when many statistical quantities were near their maximum change.

4.2.2 Identification of the most-affected events in the late period

It will be shown in this section that the reduction of the Reynolds stresses is due to a weakening of sweeps and ejections by vortices of both signs, but as in the initial period, sweeps by positive vortices and ejections by negative vortices are most affected.

In coordinates aligned with the maximum streamwise intensity (eqn. 2.1d) the intensity-weighted PDFs (Figure 4.10) show the same trend as in the initial period. That is, the streamwise intensity is reduced because there are fewer medium-range positive and intense negative u'_* , the normal intensity is reduced because there are fewer medium-range v' of either sign, and a reduction of negative $\frac{\partial w'_*}{\partial y}$ causes the

reduction in spanwise intensity. The latter is consistent with a reduction of sweeps associated with positive vortices.

The quadrant analysis for $\overline{u'_*v'}$ at $t=0.6$ indicates that, as in the early period (Figure 4.11), both sweeps and ejections are weakened (Figure 4.30). This result is independent of the choice of coordinates. In general, the analysis of Reynolds stresses containing u'_* and/or v' was qualitatively independent of the choice of coordinates, while stresses containing w'_* were strongly coordinate-dependent.

Conditional averaging (see §2.7) was used in order to establish how the changes in sweeps and ejections by vortices of each sign contribute to the changes in the Reynolds stresses. The primary difficulty with conditional averaging is to find the condition which captures the structure of interest. The changes at $t=0.3$ can be used to test the choice of condition, since the most affected events at this time are known to be sweeps by positive vortices and ejections by negative vortices. Conditioning on $\frac{\partial w'}{\partial y}$ at the wall has the advantage that no subjective choice of location inside the flow is needed. The range $20 < \frac{\partial w'}{\partial y} < 50$ and $-50 < \frac{\partial w'}{\partial y} < -20$ gave the correct trends (Figure 4.31). A narrower range (30-40) also revealed the correct features. In the later period, the conditional eddy corresponding to $\frac{\partial w'_*}{\partial y} = \pm(20 - 50)$ at the wall was used, where w'_* is the spanwise velocity in coordinates rotated with the intensity angle (eqn. 2.1d). In these coordinates, the rms of $\frac{\partial w'_*}{\partial y}$ is at a minimum. The conditionally averaged flow shows a reduction of sweeps and ejections by vortices of both signs, but the two events which were most affected during the initial period, sweeps by positive vortices and ejections by negative vortices, are also most affected during the later period.

In order to obtain less coordinate-sensitive conditionally-averaged data, we experimented with conditioning on v . If a vertical motion is part of a vortex, it will be accompanied by a vertical motion of opposite sign either to its right or to its left according to the position of the vortex. Several locations and ranges for v were tested. Unfortunately, the results were highly dependent on the choice of conditioning, but those which gave the correct trend for the initial period showed the same trend in the later period as well. Figure 4.32 shows the averaged field of negative u'_* around $-0.25 < v < -0.2$ at $y_{2D}^+ = 10$. It can be seen that the negative values of u'_* to the right (positive z) are most reduced, which implies that negative vortices are most affected (Figure 4.3). Note that the u'_* fields corresponding to both positive and negative vortices are depicted in the conditionally averaged field.

The octant analysis was very useful in the initial period. In the later period, the coordinate-dependence of w'_* poses a problem. Although a study of the instantaneous flow fields indicated that w'_* in coordinates aligned with either the Reynolds shear stress (eqn. 2.1*b*) or the direction of maximum intensity (eqn. 2.1*d*) was a good indicator of the sign of the vortices, the respective octant analyses led to qualitatively and quantitatively different conclusions. The only consistent trend resulting from both octant analyses was strong reductions from ejections generated by negative vortices. In general, there were reductions of sweeps and ejections by vortices of both signs, but the magnitudes of the reductions varied strongly. The octant analysis for $\overline{u'_*v'}$ in coordinates aligned with the shear stress direction is shown in Figure 4.33. In order to develop a less coordinate-dependent octant analysis, w'_* was replaced by the streamwise vorticity fluctuation, ω'_{x*} , as a better indicator of the sign of the vortices. However, this approach was unsuccessful because it did not correctly predict the well-established trends for the early period.

In conclusion, sweeps and ejections by vortices of either sign generate reduced fluctuations in the later period. The two events which were most affected during the initial period (I and II in Figure 4.4) continue to be most affected in the later period. In addition the other sweep and ejection events by vortices of both signs are weakened (III and IV in Figure 4.4).

4.2.3 Underlying mechanisms in the late period

Conditional averaging (Figure 4.31) and the intensity-weighted PDF's for $\frac{\partial w'}{\partial y}$ at the wall (Figure 4.10*c*) indicate that sweep-motions by positive vortices are reduced in the later period as well. The mechanism is believed to be the same: in 3D, fluid will be moved toward the vortex-center (in coordinates moving with the vortex) where the vertical velocity is lower, and it will therefore not reach as close to the wall as in 2D (Figure 4.4*a*).

The weakening of ejections associated with negative vortices are believed to be caused by the same mechanisms as in the initial period: that is, the fluid closest to the wall is convected in the spanwise direction instead of being lifted (Figure 4.4*b*), and the ejected fluid experiences more viscous dissipation due to convection of low-speed fluid on top of high-speed fluid in 3D (Figure 4.25). This is supported by the budgets for the Reynolds stresses which show continued reductions due to less production and more dissipation (Moin *et al.* 1990). It is also supported by the weighted PDF for u'_*

(Figure 4.10a) which shows reductions in the magnitudes of the most negative values of u'_* which result from the transport of fluid from near the wall.

Ejections due to positive vortices generates less intense fluctuations in the later period. Two mechanisms are believed to be responsible for this. First, the low- and high-speed streaks are shifted with respect to the vortices above them (Figure 4.4.c). The vortices then pump higher-speed fluid away from the wall and thereby generate less Reynolds shear stress than if they had pumped low-speed fluid. It can be seen in Figure 4.34c that in 3D high-speed fluid indeed resides under the ejection side of the vortex shown. A second mechanism is the change in particle trajectories. Fluid which is ejected will simultaneously be convected away from the vortex into a region of weak vortex-induced vertical motion. This is seen in Figure 4.34a where "stream-lines" within a vertical plane normal to a vortex indicate the trajectory of ejected fluid.

Sweep-motion by negative vortices generate lower levels of velocity fluctuations in the later period (Figure 4.4d). This is contrary to the initial period, when this type of event generated slightly more intense fluctuations than in 2D (see octant analysis in Figure 4.12). When the vortices are submerged in the spanwise boundary layer, the fluid swept toward the wall will simultaneously be swept away from the vortex and will not reach as close to the wall. This is seen in Figure 4.35 which shows selected "stream-lines" around a negative vortex in the 3D flow. This completes the presentation of the evidence and the corresponding mechanisms for the affected events sketched in Figure 4.4.

There are two characteristic directions for the Reynolds stresses. These are the direction of maximum streamwise intensity (eqn. 2.1d) and the direction of maximum streamwise Reynolds shear stress (eqn. 2.1b). The latter leads the former (Figure 4.29) and the reason for this will now be discussed. The difference between these angles is believed to be due to different turning angles of the vortices according to their distance from the wall. The vortices which are closest to the wall generate the highest magnitudes of positive u' and negative v' . Their high turning angles are therefore responsible for high stress- and intensity angles. Vortices further out generate significant levels of negative u' , but generate low levels of positive v (§3.1). These vortices (with lower turning angles) will therefore contribute more to the intensity angle than to the shear stress angle. Thus, the intensity angle is lower

because it has more contributions from the slightly turned vortices further from the wall than the shear stress angle.

Finally, a change which is clearly seen in the instantaneous flow fields is the kinking and later break-up of the wall layer streaks (Figure 4.36). It is not known to what degree this phenomenon affects the Reynolds stresses. The break-up mechanism is primarily in the horizontal plane. Vortices which in 2D are aligned with each other in the streamwise direction next to a streak turn in 3D. They will then no longer be aligned behind each other and the streak breaks up. Since intense high-speed regions on the high-speed streaks are well correlated with near-wall vortices, these regions turn swiftly and significantly (Figure 4.36).

In the late period, turbulent intensities near the wall begin to recover. The early part of the apparent recovery is not due to diminishing of 3D effects. It will be shown below that the 3D effects are still present; however, they are overcome by the increased mass flow. Recovery from 3D effects should occur when the vortices begin to align with the mean velocity gradient direction. In order to find when this occurs, it is necessary to estimate the angle of these vortices as a function of time and distance from the wall. One way of doing this is to compute the direction of strongest correlation for quantities which best capture vortices. The expression for this angle in the horizontal plane, θ_R , is given in eqn. (2.7.2). In Figure 4.37, the angles of strongest auto-correlation for p' , $\nabla^2 p'$ and $\omega'_x \cos(\theta_R) + \omega'_z \sin(\theta_R)$ are shown at $t=0.6$. All three angles are nearly the same (except in the viscous sublayer). The mean velocity in the direction normal to θ_R increases continuously in magnitude during the time-period studied (Figure 4.38). Thus, the three-dimensional effects in the late period have not diminished and recovery is caused by the increased "streamwise" mass flow.

4.3 Mean velocities

The mean velocity component in the x -direction, U , is virtually unchanged during the initial period ($t \leq 0.3$). Later, U is reduced near the wall and since the mass flow in the x -direction is fixed, it increases further out. The percentage reduction is largest very close to the wall, where $\frac{\partial U}{\partial y}$ undergoes its maximum drop of about 8% (Figure 4.39). This is the only observed quantity which was still dropping at $t=1.05$, when the accumulation of statistics was ended. During the initial period, the weakening of the events with highest and lowest u cancelled their respective contributions to U . In the later period, the turning reduces the magnitude of positive u' more than

the magnitude of negative u' because the vortices closest to the wall (which turn) generate the most intense positive u' while vortices further out (which don't turn) generate as intense negative u' as vortices close to the wall. The net effect is a reduced U near the wall in the later period.

The spanwise mean velocity component, W , is identical to the laminar profile (§2.5) during the initial period. When the structures turn, they make the Reynolds shear stress vector turn as well and the W profile is no longer laminar (Figure 4.40). However, W does not develop a logarithmic region during the time-period studied.

4.4 Vorticity intensities

In 2D channel flows, the x -vorticity intensity, $\overline{\omega_x'^2}$, is mostly due to quasi-streamwise vortices and the secondary vorticity they create below them (Kim *et al.* 1987). Because the sign of the secondary vorticity is opposite to that of the primary vortex, there is a local minimum in the viscous sublayer (Figure 4.41a). At $t=0.3$, $\overline{\omega_x'^2}$ is reduced all the way out to $y_{2D}^+ \approx 80$ with the largest percentage reduction of 9% at the wall. The reason for the reduction near the wall, where $\overline{\omega_x'^2} \approx \overline{w'^2}/y^2$, has already been discussed in Section 4.1. The reduction outside the spanwise boundary layer is believed to be due to reduced gradients caused by the weakened ejections from the near-wall region. After $t=0.3$, the shear layers which contain strong spanwise vorticity begin to turn. Since $\overline{\omega_z'^2}$ is significantly larger than $\overline{\omega_x'^2}$ in near-wall 2D flows, the turning tends to increase $\overline{\omega_x'^2}$ in this region. Outside $y_{2D}^+ = 50$, the two vorticity intensities are of about equal magnitude, and $\overline{\omega_x'^2}$ is reduced due to weakened ejections from the near-wall region. The weighted PDF for ω_x' at $y_{2D}^+ = 20$ shows an increase in negative values and a decrease in positive values at $t=0.6$ (Figure 4.42a). This is consistent with the turning of the shear-layers which generate more $\frac{\partial w'}{\partial y} < 0$. Note that the turning transforms some of $\frac{\partial u'}{\partial y} < 0$ of the shear layers to $\frac{\partial w'}{\partial y} < 0$.

Figure 4.41b shows that the vertical vorticity intensity, $\overline{\omega_y'^2}$, drops across the boundary layer. Note that ω_y is invariant with coordinate rotation. The maximum percentage reduction is 20% at $t=0.75$ and $y_{2D}^+=38$; recovery starts at $t=0.5$ near the wall. The weighed PDFs (Figure 4.42b) show that both positive and negative values of significant magnitude are reduced. These values are usually found between near-wall streaks, and next to shear layers further out (high $|\frac{\partial u'}{\partial z}|$ in both cases). The reduction is therefore consistent with the reduced values of u' . Recovery starts earlier

than for the streamwise velocity intensity and the turbulent kinetic energy, which indicates that the normal vorticity is more directly affected by the break-up of the streaks (§4.2.3) than the streamwise velocity fluctuations.

The spanwise vorticity intensity, $\overline{\omega_z'^2}$, (Figure 4.41c) is proportional to $\overline{u'^2}$ very close to the wall and decreases due to the weakening and turning of the streaks. During the initial period, an increase occurs between $y_{2D}^+ = 7$ and 25 because of the increased dissipation associated with ejections generated by vortices with a negative sign of rotation (§4.1.2). The PDF for ω_z' at $t=0.3$ (Figure 4.42c) shows an increase in contribution from $\omega_z' > 0$ which is consistent with more intense $\frac{\partial u'}{\partial y} < 0$. Later, this increase develops into a plateau due to the turning of the vortices (see profile of $\overline{\omega_z'^2}$ Figure 4.41a).

4.5 Two-point correlations and energy spectra

Two-point velocity correlations

$$R_{ij}(\Delta x, \Delta z, y, y', t) = \overline{u_i'(x, z, y, t)u_j'(x + \Delta x, z + \Delta z, y', t)} \quad (4.5.1)$$

contain information about the size and relative locations of structures. In a 2D near-wall layer, R_{11} is used to study the properties of the streaks while R_{22} and R_{33} are used to extract information on the average size and intensity of the quasi-streamwise vortices. In 3D, correlation contour lines in vertical planes are skewed (shown for R_{11} in Figure 4.43), while in the horizontal plane they reflect the weakening and turning of the turbulence structures (see below). Below, the correlations of the velocities in the rotated coordinates in horizontal planes are discussed. The rotation angle corresponds to the direction of maximum streamwise velocity intensity (eqn. 2.1d). Thus, R_{ii^*} is defined as in eqn. (4.6.1) with u_i' replaced by u_{i^*}' (§2.1).

Figures 4.44, 4.45, 4.46 show the evolution of velocity two-point correlations at $y_{2D}^+ = 10$. At $t=0.3$, $W = 0.99W_\infty$ at $y_{2D}^+ = 20$ and the structures have turned very little. The changes in the correlation length and magnitude are therefore mainly due to the weakening of the velocity fluctuations. Later, the most pronounced turning-effect is the formation of a kink in the contour lines for R_{11^*} and a significant difference in the directions of maximum correlation for short separations between the three auto-correlations. The angle of maximum correlation for R_{11^*} remains fairly close to the Reynolds shear stress angle for a wide range of distances from the wall and

times, while the angles for R_{22} and R_{33*} are larger. Figure 4.47 shows the angles of maximum correlation obtained from eqn. (2.7.2) as a function of the distance from the wall.

Differences in correlation angles are believed to be due to the variation of the turning angles of the vortices with distance from the wall. A review of the discussion of Figure 3.1 regarding the relation between the distance of a vortex from the wall and the velocity fluctuations it generates in 2D flows is therefore useful. The vortices which are closest to the wall turn the most and are the primary contributors to all the two-point correlations near the wall. Vortices further out generate fairly low velocity fluctuations near the wall except for negative u'_* and, therefore, contribute with their low turning angles, more to R_{11*} than to R_{22} and R_{33*} . The angle of maximum correlation for R_{11*} is therefore the lowest of the three near the wall.

The kink in R_{11*} is believed to be due to the turning of the near wall vortices. For large separations Δx and Δz , $u'(x, z)$ and $u'(x + \Delta x, z + \Delta z)$ are generated by different vortices. Therefore, the correlation angle tends to be lower than the angle for short separations where the two points would be located on a single vortex (see sketch Figure 4.48). R_{22} and R_{33*} show a weaker kink. This is because the vortices in Figure 4.48 contribute to R_{22} and R_{33*} over long distances only if they both are located near the wall. On the other hand, vortices both near and away from the wall contribute to intense $u'_* < 0$ near the wall.

The two-dimensional energy spectra for the u'_{i*} velocities, E_{11*} , E_{22} and E_{33*} are shown in Figures 4.49. E_{11*} in the 3D flow shows that the large scales (low frequencies) have rotated less than the the small scales. This is another manifestation of the kink in R_{11*} . R_{11*} at large separations is mostly made up of large scale structures which have turned by a smaller angle. The lack of pronounced kinks in R_{22} and R_{33*} is related to a more uniform angle of spectral contours for E_{22} and E_{33*} .

4.6 Comparison with previously suggested mechanisms

The mechanisms for the reduction of Reynolds stresses in 3D flows which have been suggested in the literature were described in §1.4.4. These mechanisms have been tested in the channel flow of the present study. The results of these tests are described below.

Lohmann (1976) suggested that in a flow along a cylinder, part of which is spinning, the vortices would be torn apart when they encounter the cross-flow. Such a break-up was not observed in the current work (compare x -vorticity contours in Figures 4.5 and 4.28), but the vortices in Lohmann's flow experienced a stronger and more sudden cross-flow which may have caused additional effects.

Vortices outside the inner layer tend to have arch shaped heads which induce ejections (Robinson, 1991). Bradshaw and Pontikos (1985) suggested that in 3D boundary layers the heads are tilted sideways and become less efficient in producing Reynolds shear stress. This hypothesis can not be tested in the current flow due to the lack of inviscid skewing mechanism (see §1.4.2).

Anderson and Eaton (1989) suggested that the mean streamwise vorticity, Ω_x , generated in 3D, leads to the cancellation of the natural boundary layer vortices of opposite sign, and also rolls up into streamwise vortices of the same sign. Thus, a preference for vortices of one sign is developed, resulting in fewer strong ejections in between vortices of opposite signs. There are two ways in which Ω_x might reduce the number of vortices of opposite sign: either the generation of these vortices is inhibited and/or the existing vortices are destroyed. The mechanics of the formation of *streamwise vortices* were discussed in §3.1 for 2D boundary layers. It was found that sheets of ω_x were formed close to the wall which rolled up into vortices. The vorticity of the sheet was of opposite sign to the primary vortex that generated the sheet. This process was not significantly affected when a spanwise pressure gradient was imposed. Using the minimal channel (§2.4) as the basic test set-up, a 2D flow with a strong streamwise vortex of negative sign was selected. Then two simulations with the imposed pressure gradient in the positive and negative z -directions were run. Comparing the 3 simulations (2D and two 3D's) did not reveal a marked difference in the process of formation and roll-up of a positive vortex sheet into a streamwise vortex (Figure 4.50). Note that in Figure 4.50c the vorticity of the vortex sheet is stronger than that in 2D because it is superimposed on the mean streamwise vorticity. However, the Figures showing the roll-up process (*b, d, f*) further downstream are very similar.

In addition, conditional averaging was used to study whether there were fewer vortices of one sign in the 3D channel. Several conditions were attempted (various ranges of ω'_x and v') and, depending on the condition used, the results sometimes indicated a weak preference for negative vortices, but never a preference for positive

vortices (mean streamwise vorticity is positive in the present flow). The mechanism proposed by Anderson and Eaton (1989) therefore does not occur in this flow.

Simpson and Devenport (1990) argued that low-speed fluid which is pushed sideways by high-speed fluid near the wall need not be ejected away from the wall in 3D flows due to the extra "spatial degree of freedom". The reduction in strength of the ejections is consistent with the findings of the present study (Figure 4.4*b* and *c*). However, their reasoning in terms of a third dimension of spatial freedom is unclear since the "three-dimensionality" only referred to in the mean flow and both 2D and 3D flows are three-dimensional.

Eaton (1992) suggested that the near-wall streamwise vortices respond to 3D effects in the same manner as the large imbedded vortices investigated by Shizawa and Eaton (1990) would. They found that vortices with sign of rotation opposite to that of the mean streamwise vorticity interacted with the cross-flow in a very different manner than those of opposite sign. Much weaker negative streamwise fluctuations were produced (weaker ejections) if the vortex-generated motion near the wall was in the same direction as the mean cross-flow while vortices of opposite sign generated stronger ejections of low-speed fluid. The imbedded vortices were well outside the location of maximum spanwise cross-flow such that the cross-flow below them was the same in both fixed coordinates and coordinates moving with the vortices (see sketch in Figure 4.51). This is not the case for the naturally occurring streamwise vortices closest to the wall in the 3D channel flow. That is, in the 3D channel flow in coordinates moving with the vortices, the ejections are most reduced for vortices with induced motion near the wall opposite to the mean spanwise flow (Figure 4.4*b*). It therefore seems that the imbedded vortices behave differently from the near-wall vortices in TBLs. We note that the embedded vortices of Shizawa and Eaton were much stronger than naturally occurring vortices in TBLs. In order to study the effect of the cross-flow on the most intense vortices in the channel flow, the average flow fields around a strong vortex was computed using conditional averaging. At $t=0.0$, 0.3 and 0.6 the ensemble averaged flow field around points with $|\frac{\partial w'}{\partial y}| > 100$ at the wall was computed (Figure 4.52). It can be seen that the conditionally averaged flow is consistent with the experimental result for the imbedded vortices. That is, strong vortices with induced motion in the direction of the mean spanwise flow generate the weakest ejections. A plausible explanation is that negative vortices of medium or low strength are unable to oppose the mean cross-flow and lift the fluid closest to the wall

as described in §4.1.2 (Figure 4.4.b). However, the strongest vortices are able to lift fluid from very close to the wall as well as the fluid being convected toward them.

Finally, Littell and Eaton (1991) measured turbulence statistics in an *equilibrium* 3D turbulent boundary layer on a spinning disk (see §1.4.3). Conditionally averaged two-point correlations offered information consistent with the present findings on the effect of the cross-flow on the streamwise vortices. Their results indicated that vortices with the same sign as the local spanwise mean velocity gradient generated weaker sweep-motion while vortices of opposite sign generated weaker ejections.

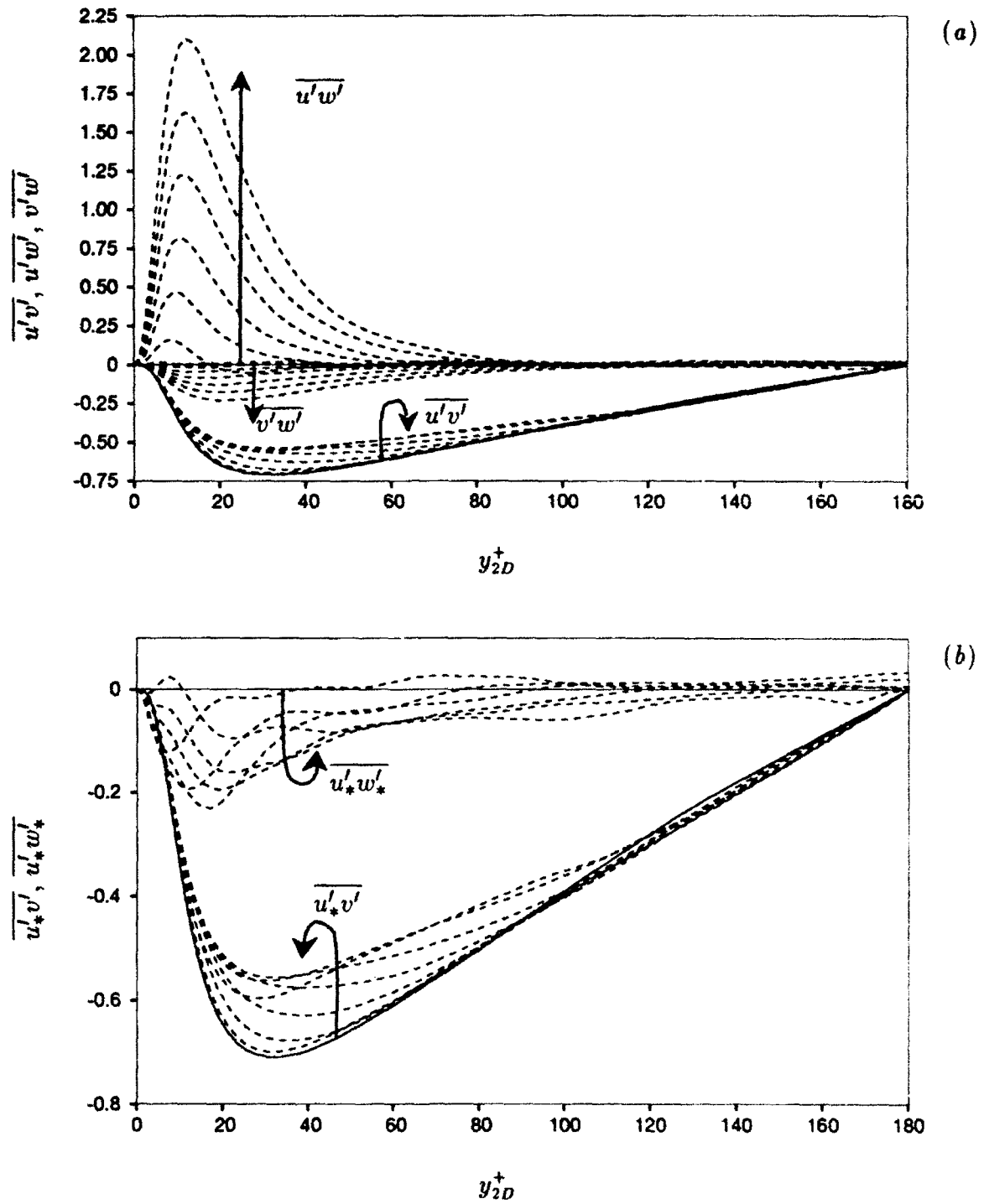


FIGURE 4.1. Reynolds shear stress profiles in (a) initial coordinates and (b) coordinates aligned with the Reynolds shear stress direction (see eqn. 2.1b). Starting from $t=0$. (—) with increments, $\Delta t = 0.15$.

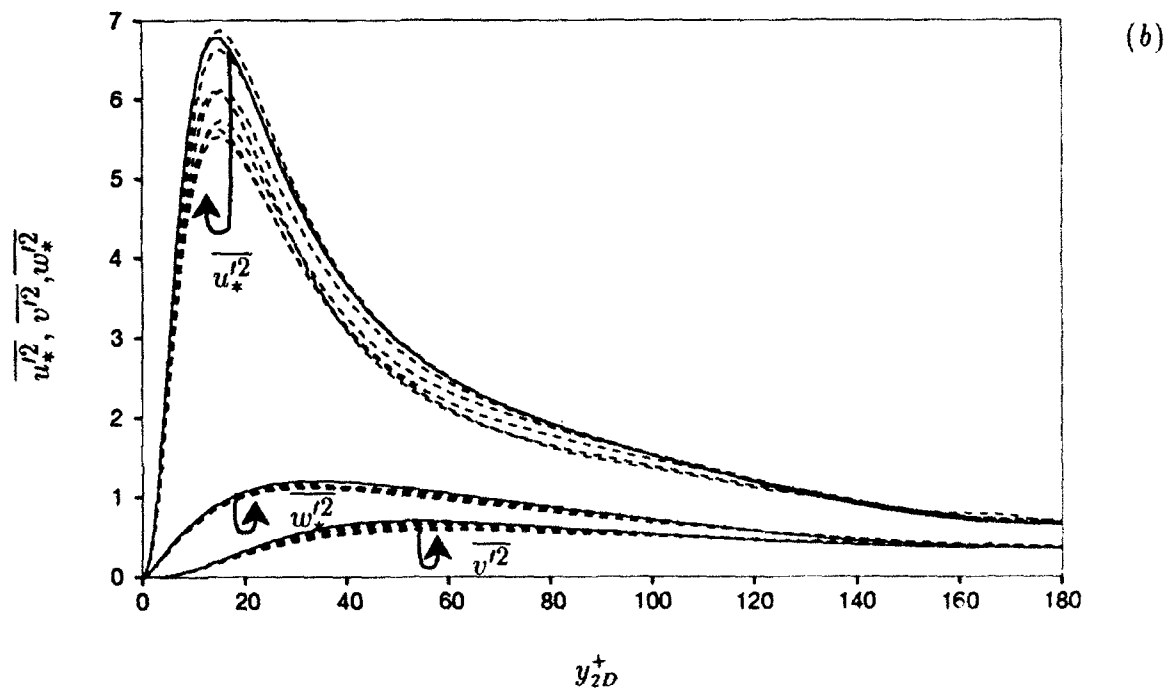
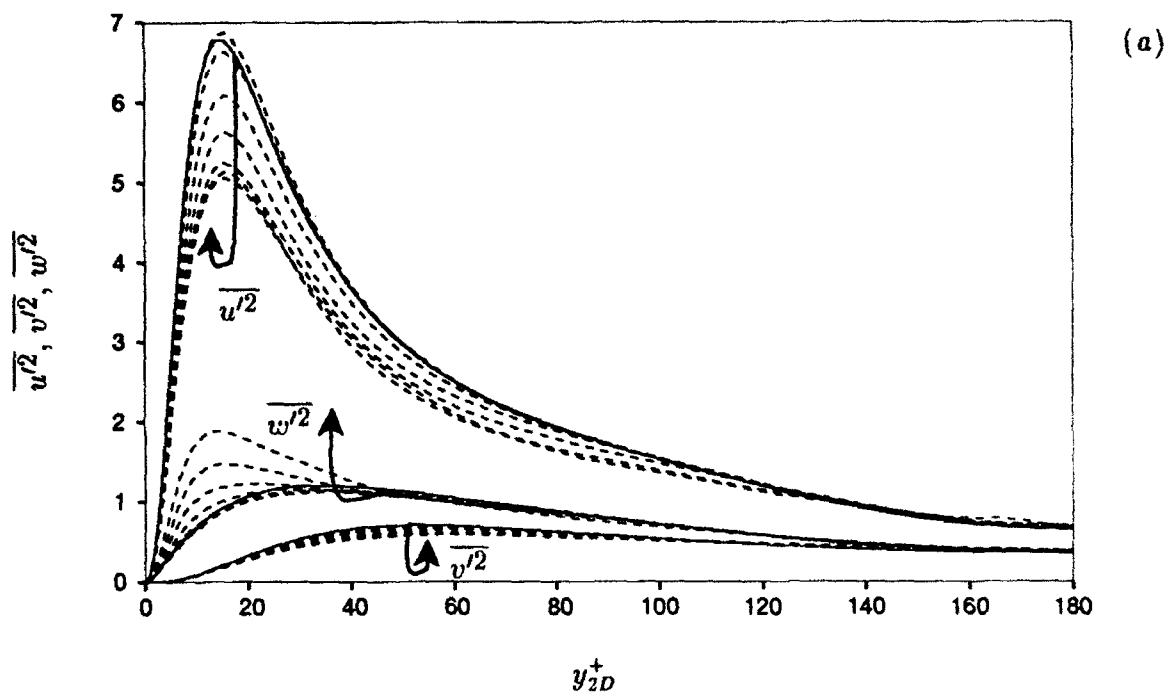


FIGURE 4.2. Intensity profiles in (a) initial coordinates and (b) coordinates aligned with the direction of maximum streamwise intensity (see eqn. 2.1d). Starting from $t=0.0$ (—) with increments, $\Delta t = 0.15$.

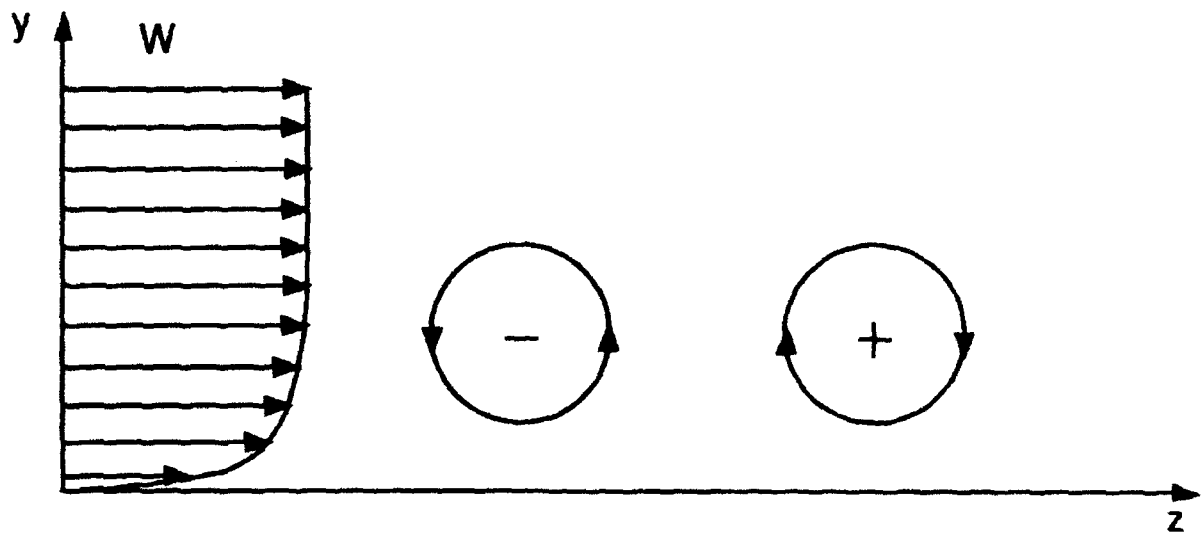


FIGURE 4.3. Schematics showing the sign convention for streamwise vortices.

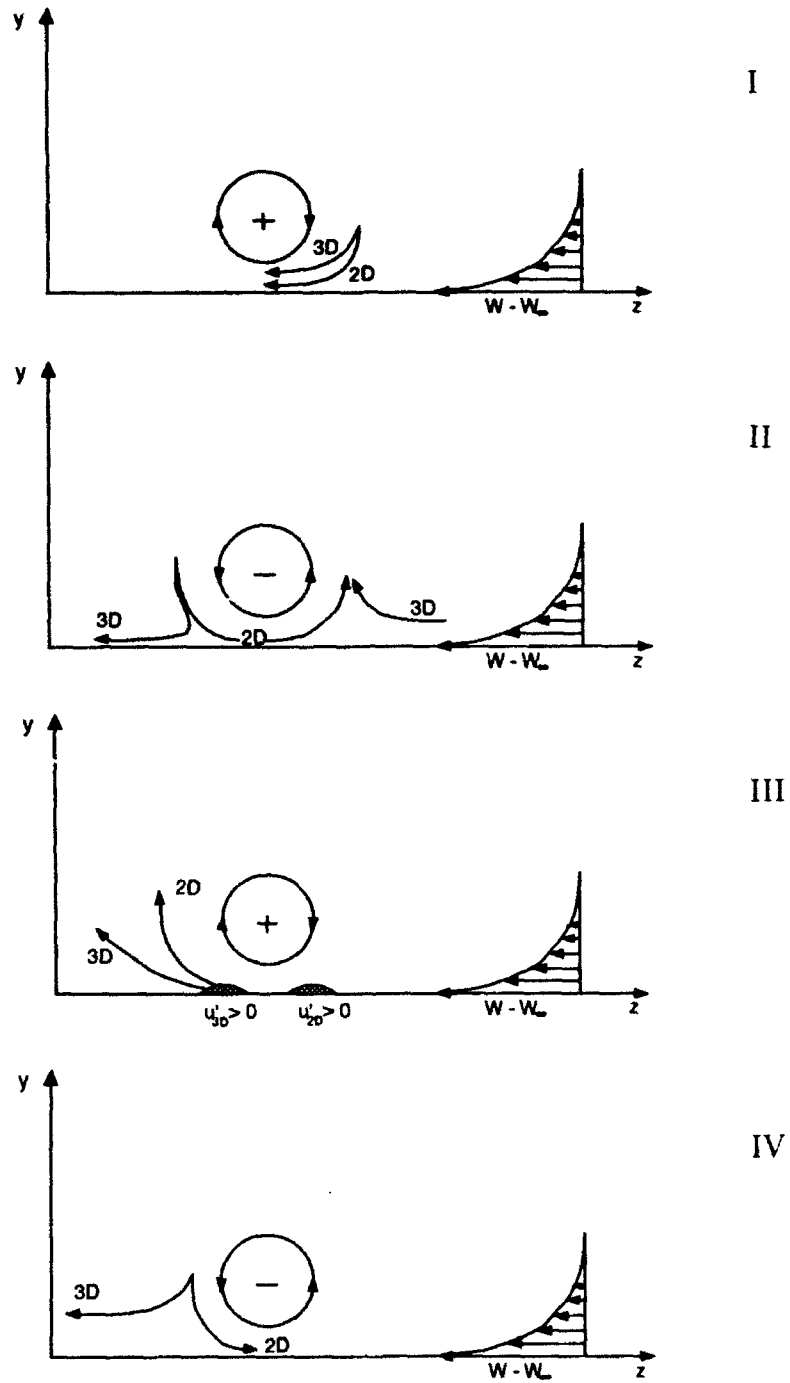


FIGURE 4.4. Schematics showing the underlying mechanisms I-IV which lead to the reduction of the Reynolds stresses. The observer is moving in the spanwise direction with the center of the streamwise vortex.

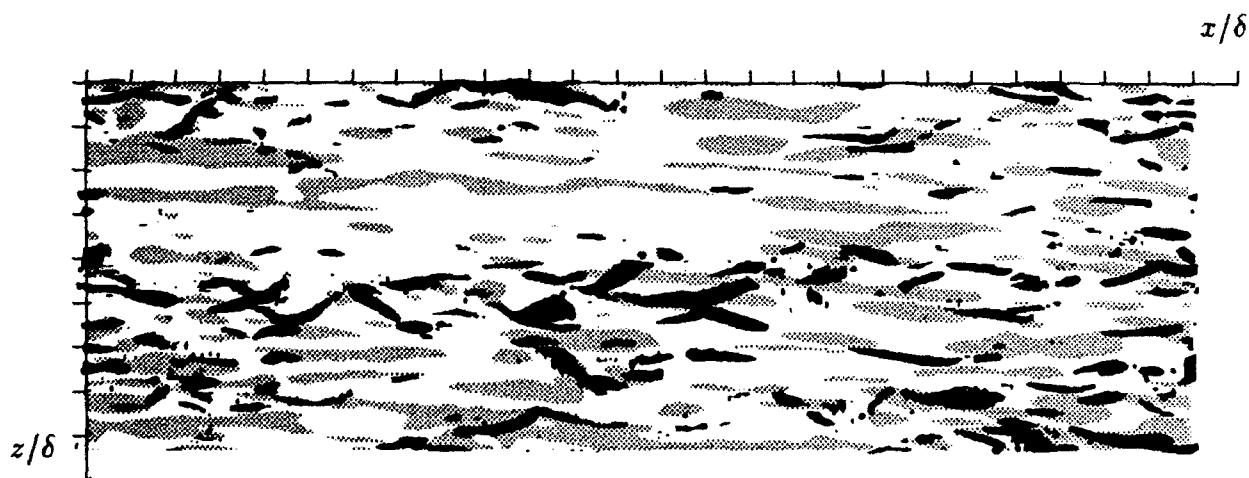
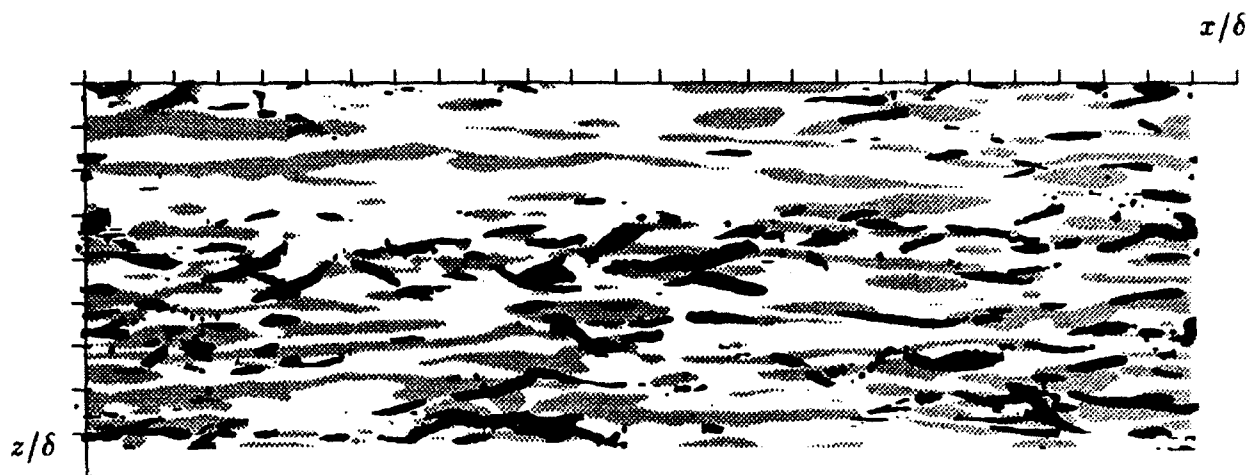


FIGURE 4.5. Top view of streaks ($|\frac{\partial u'}{\partial y}| > 50$ at the wall, shaded grey) and vortices ($|\omega'_x| > 60u_{\tau 2D}/\delta$) for the companion flows at $t=0.3$. (a) 2D flow and (b) 3D flow. Tic marks are 0.5 apart.

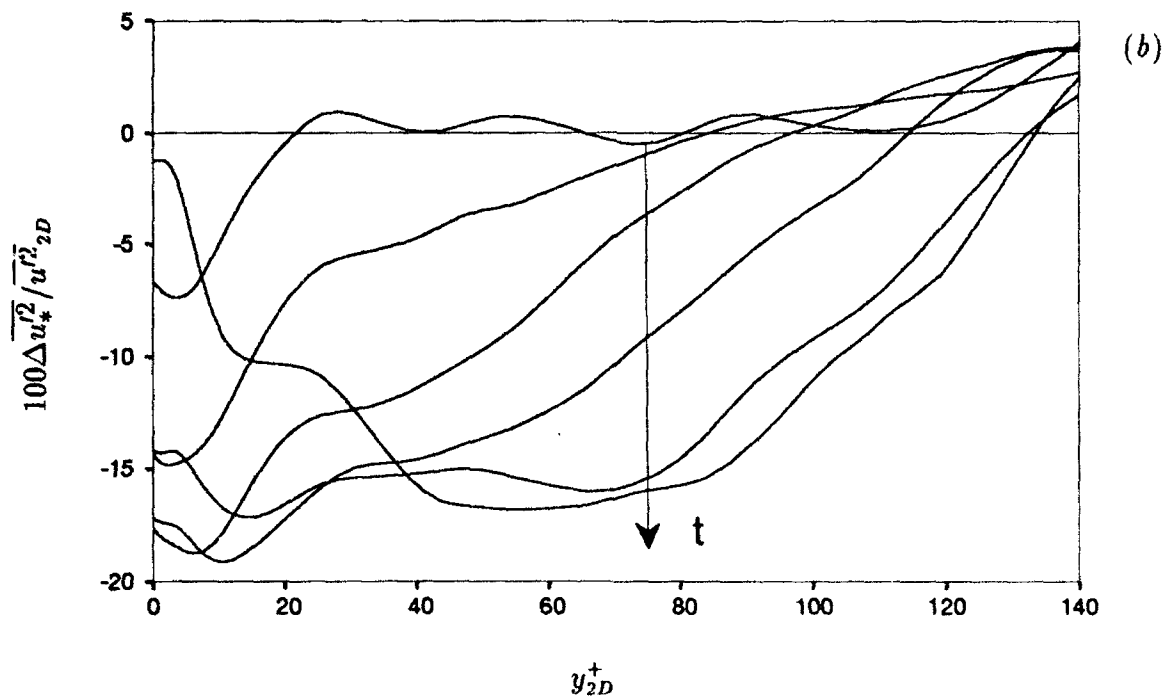
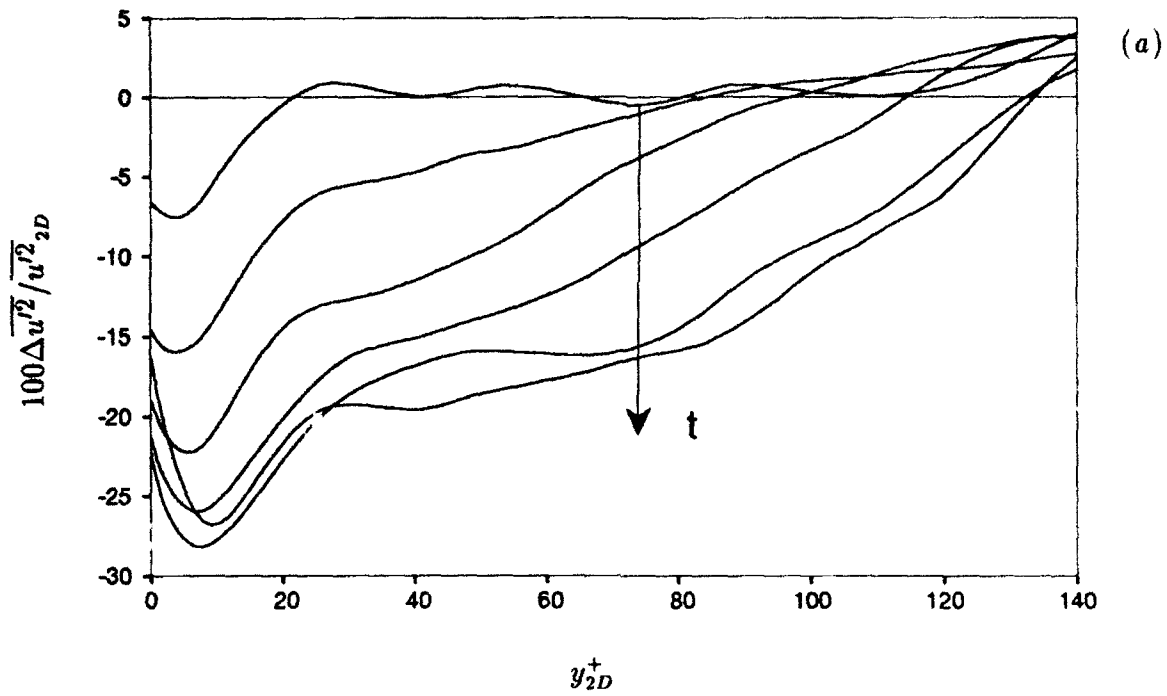


FIGURE 4.6. Percentage reduction of streamwise velocity intensity in (a) initial coordinates and (b) coordinates aligned with the direction of maximum velocity intensity. Starting with $t=0.3$ with increments, $\Delta t = 0.15$.

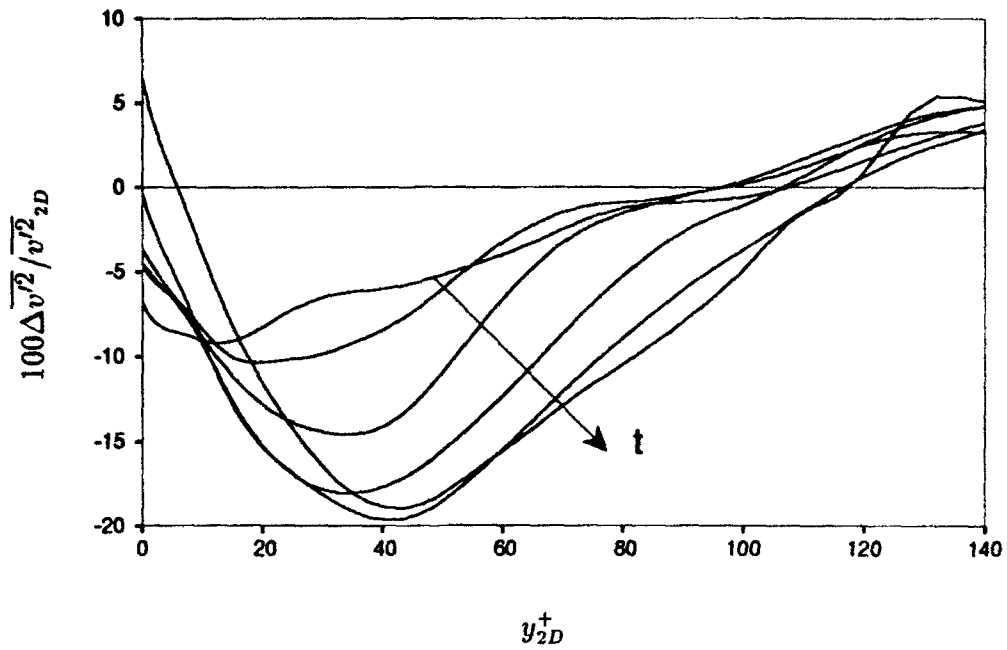


FIGURE 4.7. Percentage reduction of the normal velocity intensity. Starting from $t=0.3$ with increments, $\Delta t = 0.15$.

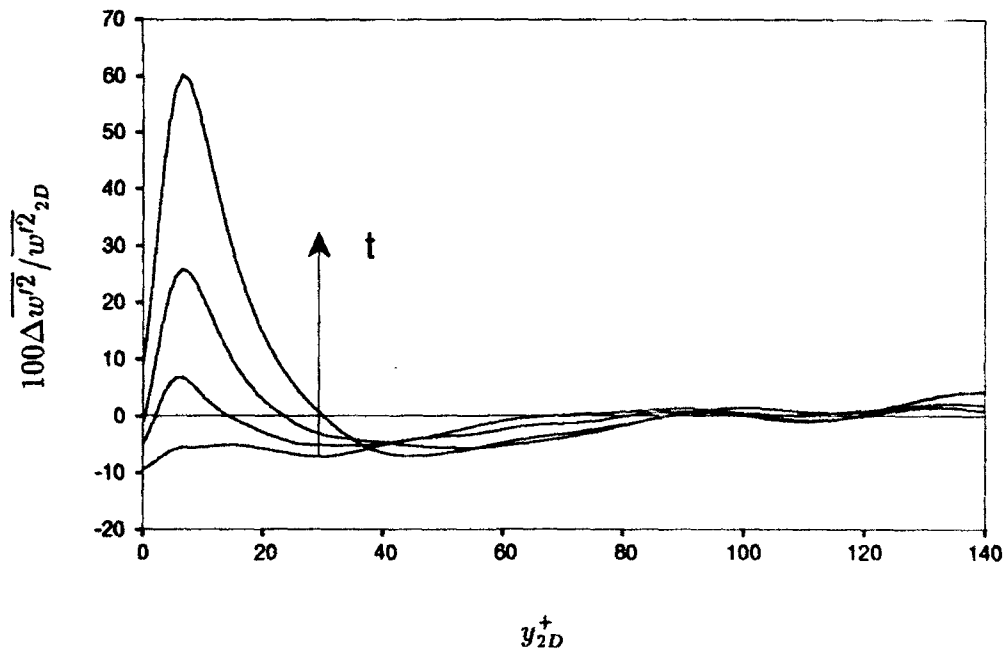


FIGURE 4.8. Percentage change in spanwise velocity intensity in initial coordinates. Starting with $t=0.3$ with increments, $\Delta t = 0.15$.

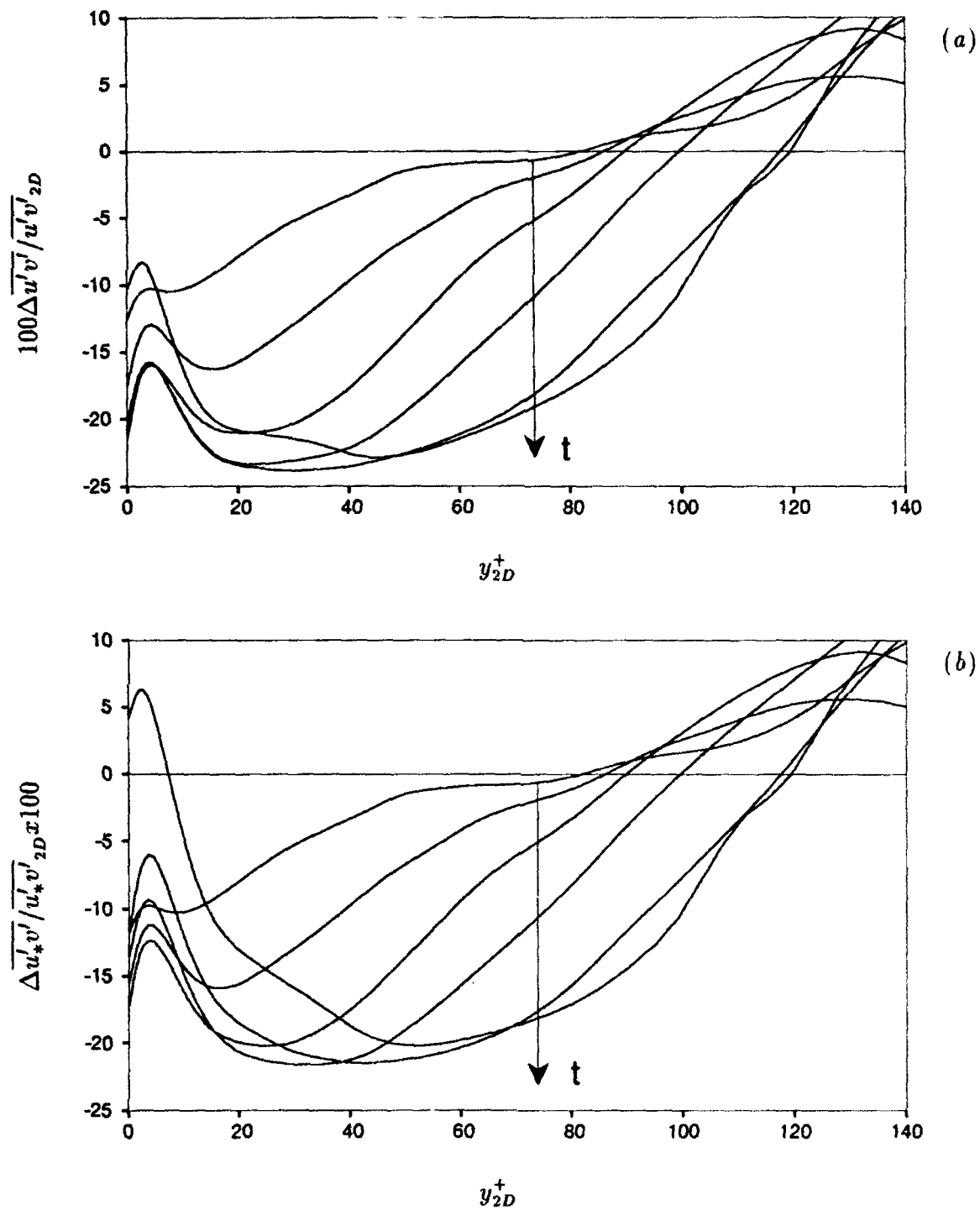


FIGURE 4.9. Percentage reduction of streamwise Reynolds shear stress in (a) initial coordinates and (b) coordinates aligned with the Reynolds shear stress direction (eqn. 2.1b). Starting with $t=0.3$ with increments, $\Delta t = 0.15$.

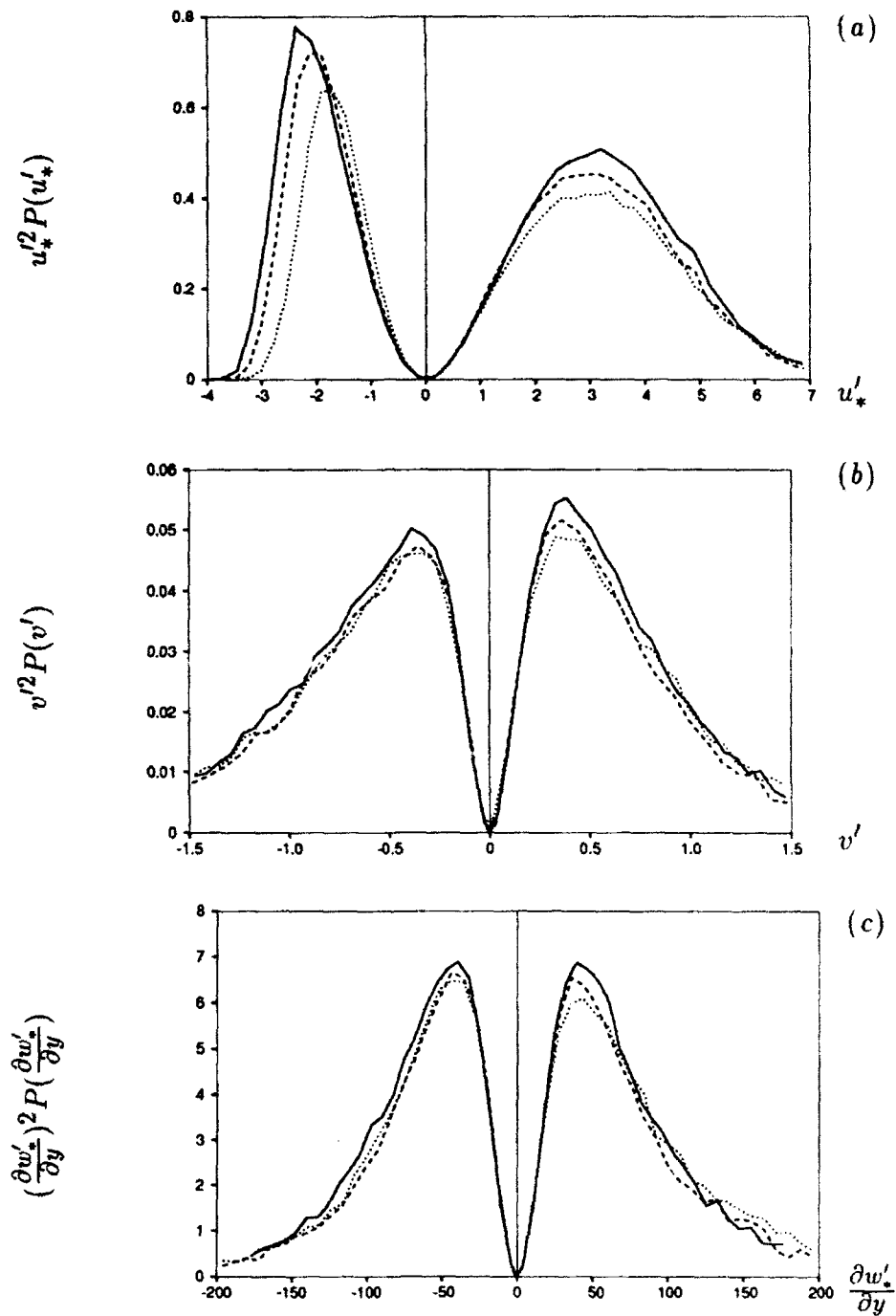


FIGURE 4.10. Intensity-weighted PDF for (a) u' at $y_{2D}^+ = 5$, (b) v' at $y_{2D}^+ = 10$ and (c) $\frac{\partial w'}{\partial y}$ at the wall. (—), $t=0$; (---), $t=0.3$; (.....), $t=0.6$. u'_* and w'_* are rotated with the direction of maximum intensity (eqn. 2.1d) for $t=0.6$ and is unrotated for $t=0.3$.

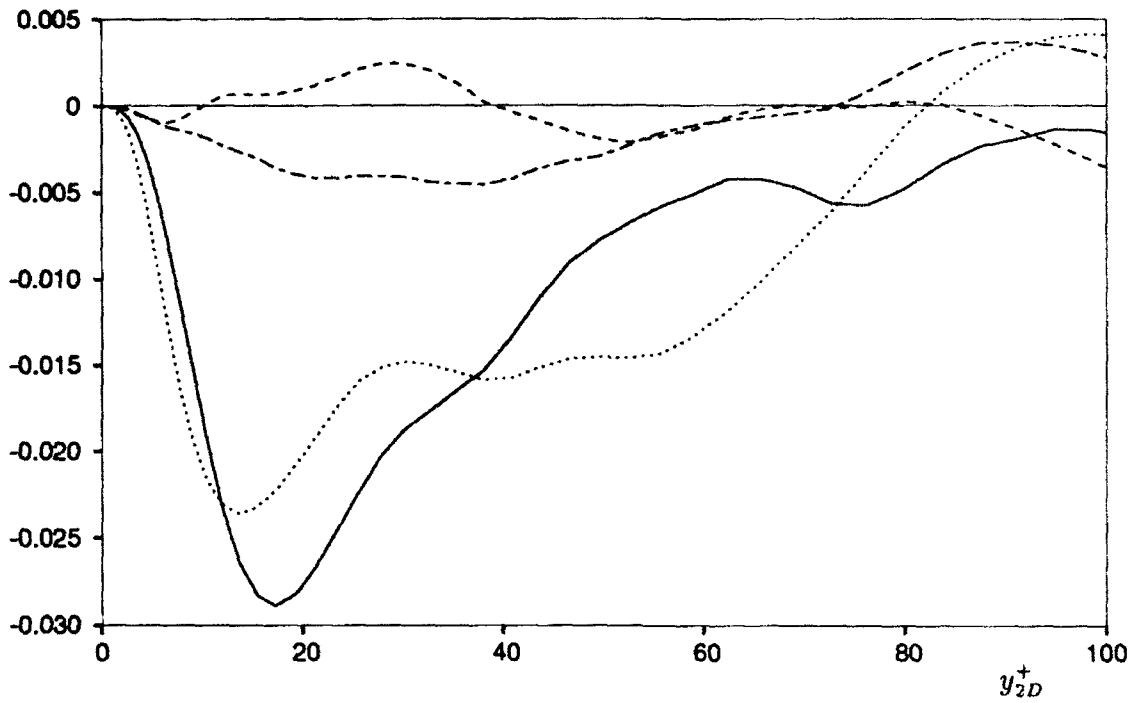


FIGURE 4.11. Change in magnitude of the contribution from each quadrant for $\overline{u'v'}$ at $t=0.3$. $u' > 0$ and $v' > 0$ (----), $u' < 0$ and $v' > 0$ (———), $u' < 0$ and $v' < 0$ (- · - · -), $u' > 0$ and $v' < 0$ (······).

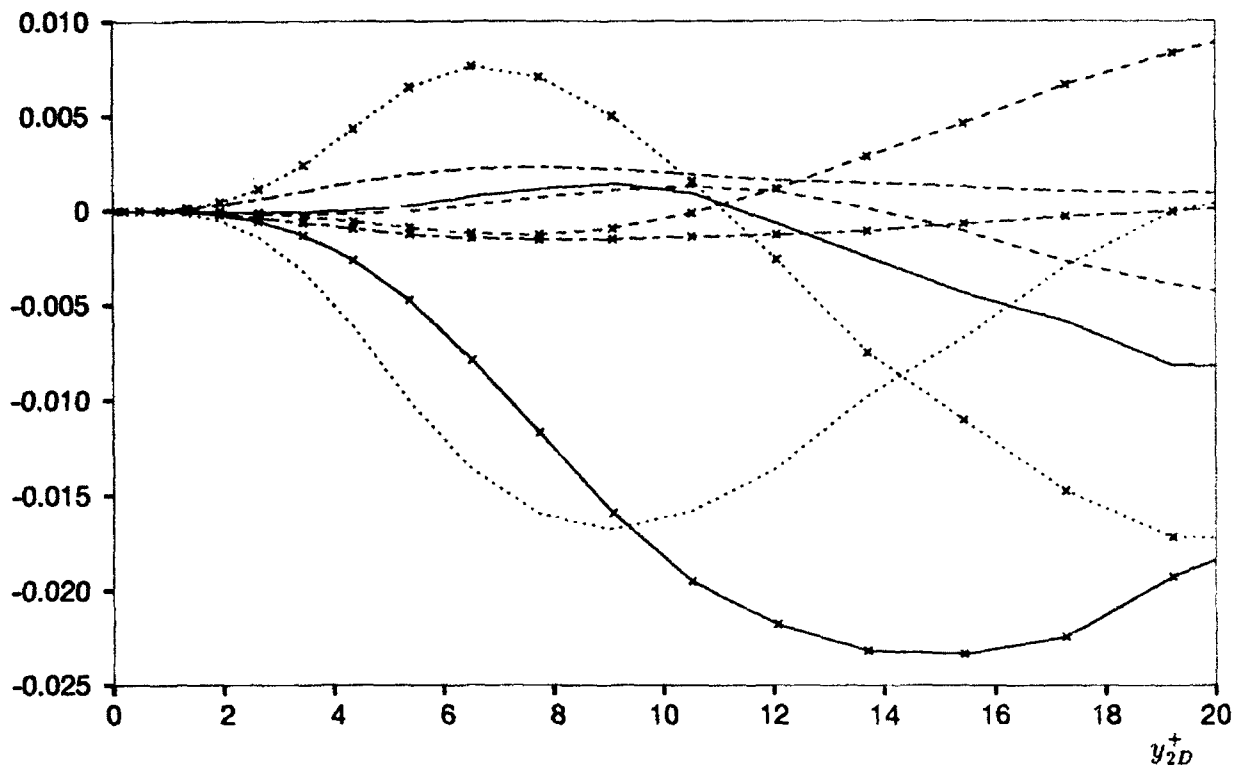


FIGURE 4.12. Change in magnitude of the contribution from each octant to $\overline{u'v'}$ at $t=0.3$. Legend as in Figure 4.11, except \times on lines represent $w' > 0$ and no \times represent $w' < 0$.

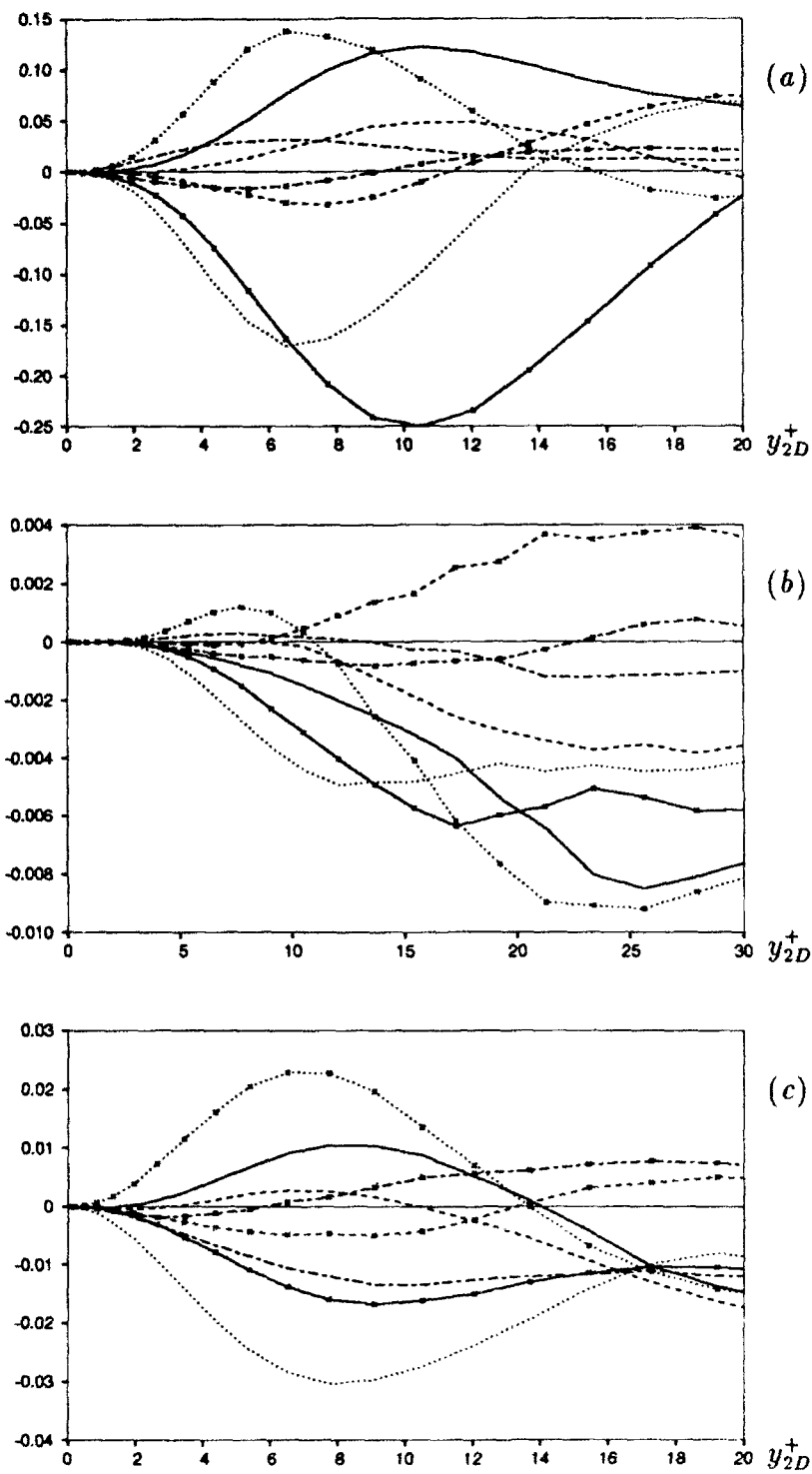


FIGURE 4.13. Change in magnitudes of the contribution from each octant at $t=0.3$ for (a) $\overline{u'^2}$, (b) $\overline{v'^2}$ and (c) $\overline{w'^2}$. Legend as in Figure 4.12.

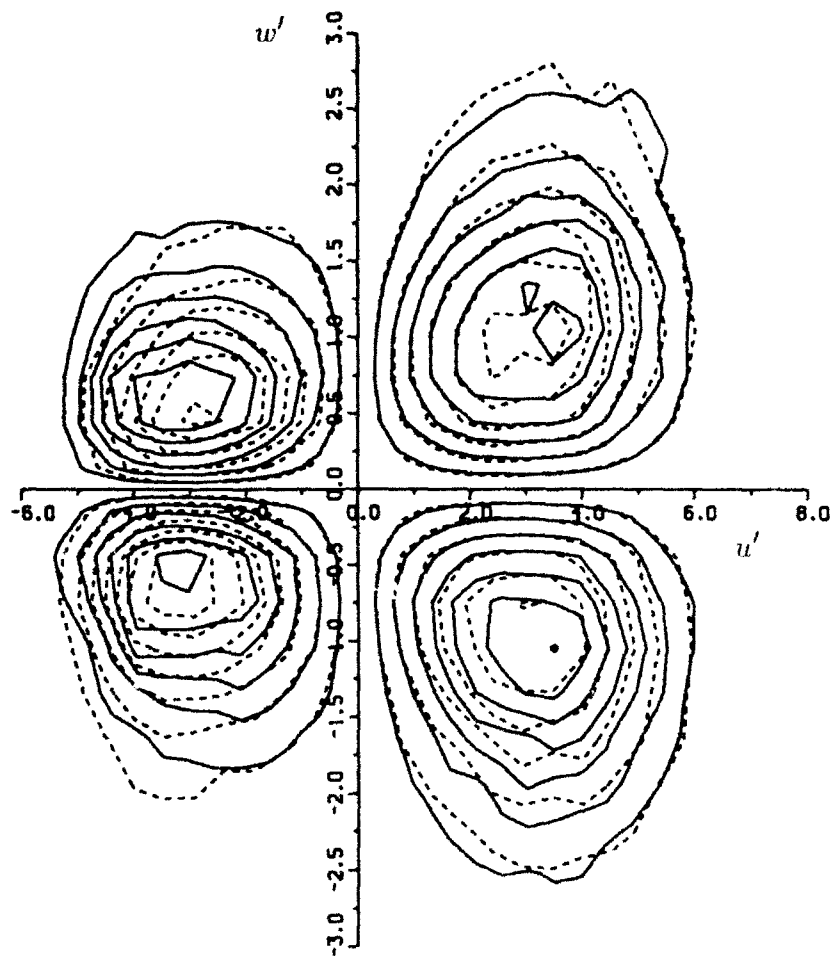


FIGURE 4.14. Weighted joint PDF between u' and w' at $y_{2D}^+ = 10$ and $t = 0.3$. 3D flow (----) and 2D flow (—).

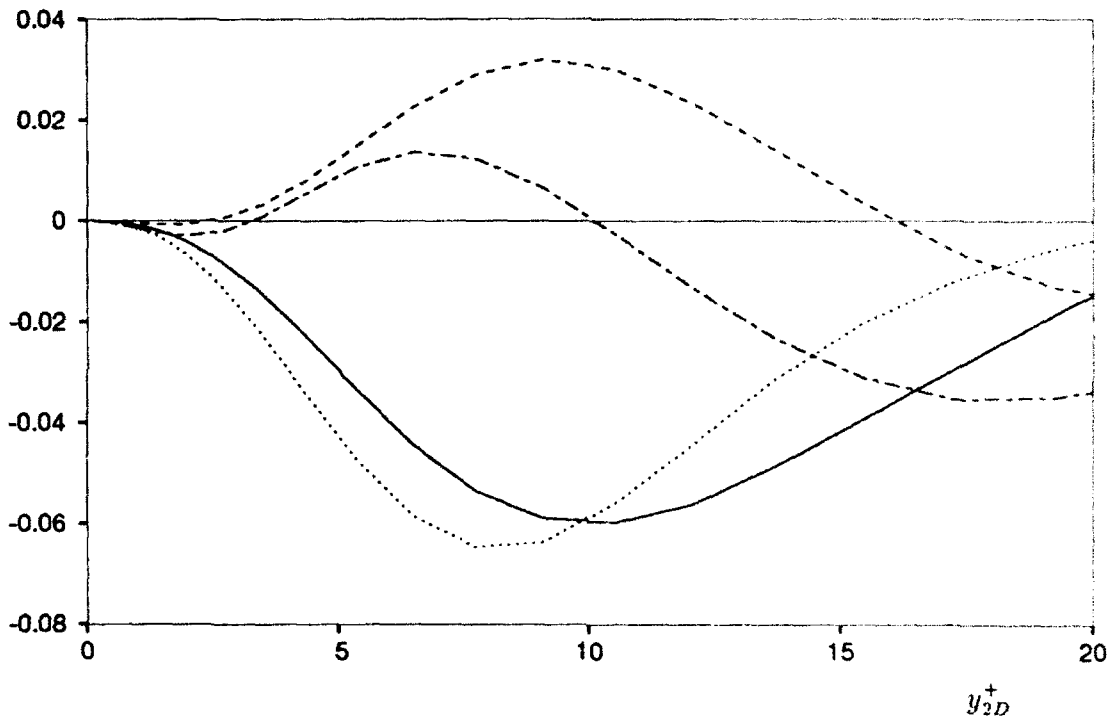


FIGURE 4.15. Change in contributions from each quadrant for $\overline{u'w'}$ at $y_{2D}^+ = 10$ and $t=0.3$. $u' > 0$ and $w' > 0$ (---), $u' < 0$ and $w' > 0$ (—), $u' < 0$ and $w' < 0$ (.....), $u' > 0$ and $w' < 0$ (- · - · -).

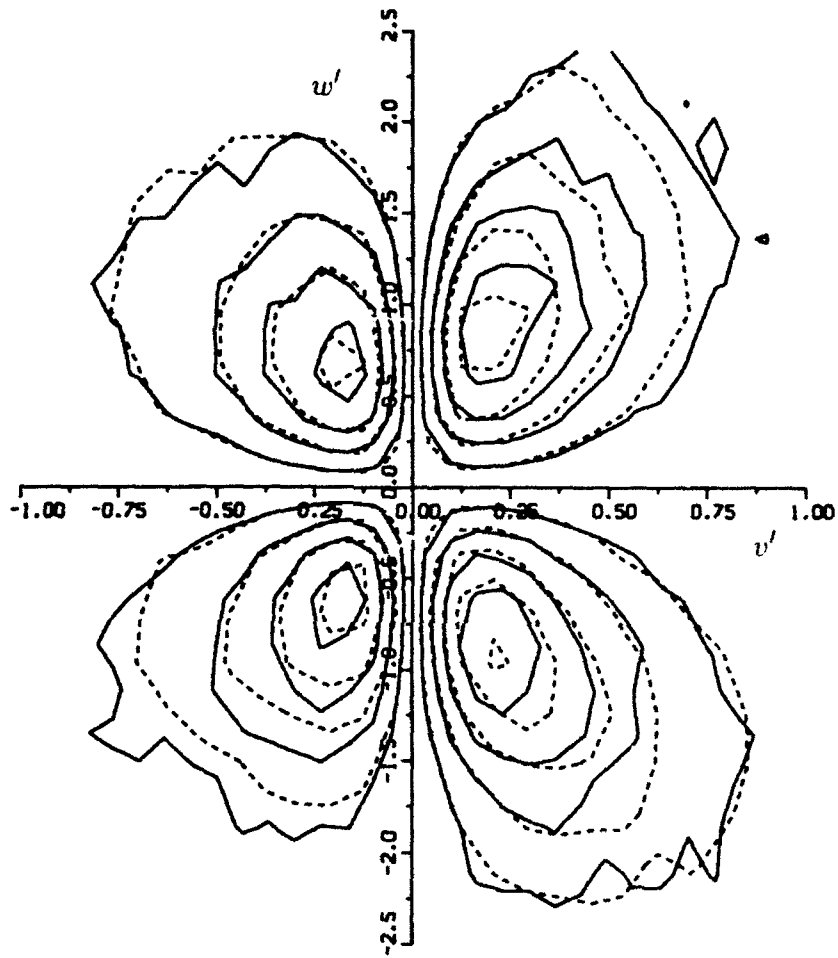


FIGURE 4.16. Weighted joint PDF between v and w at $y_{2D}^+ = 10$ and $t=0.3$. 3D flow (- - -) and 2D flow (—).

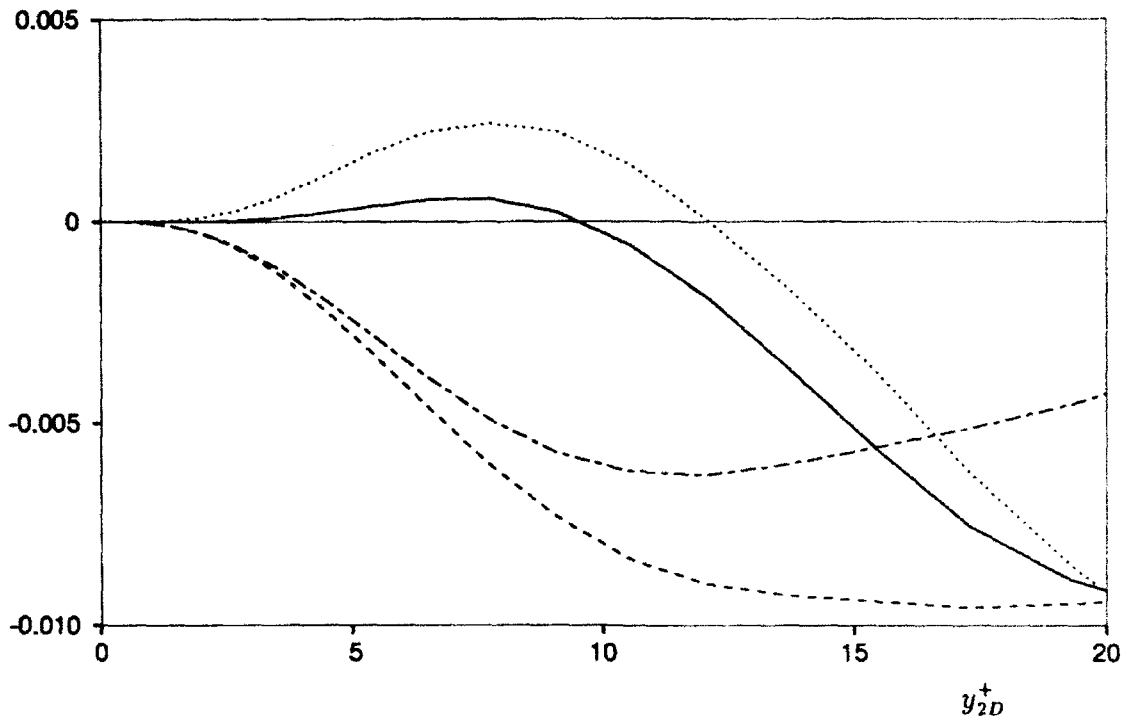


FIGURE 4.17. Change in magnitude of contribution from each quadrant for $\overline{v'w'}$ at $y_{2D}^+ = 10$ and $t=0.3$. $w' > 0$ and $v' > 0$ (—), $w' < 0$ and $v' > 0$ (----), $w' < 0$ and $v' < 0$ (.....), $w' > 0$ and $v' < 0$ (- - -).

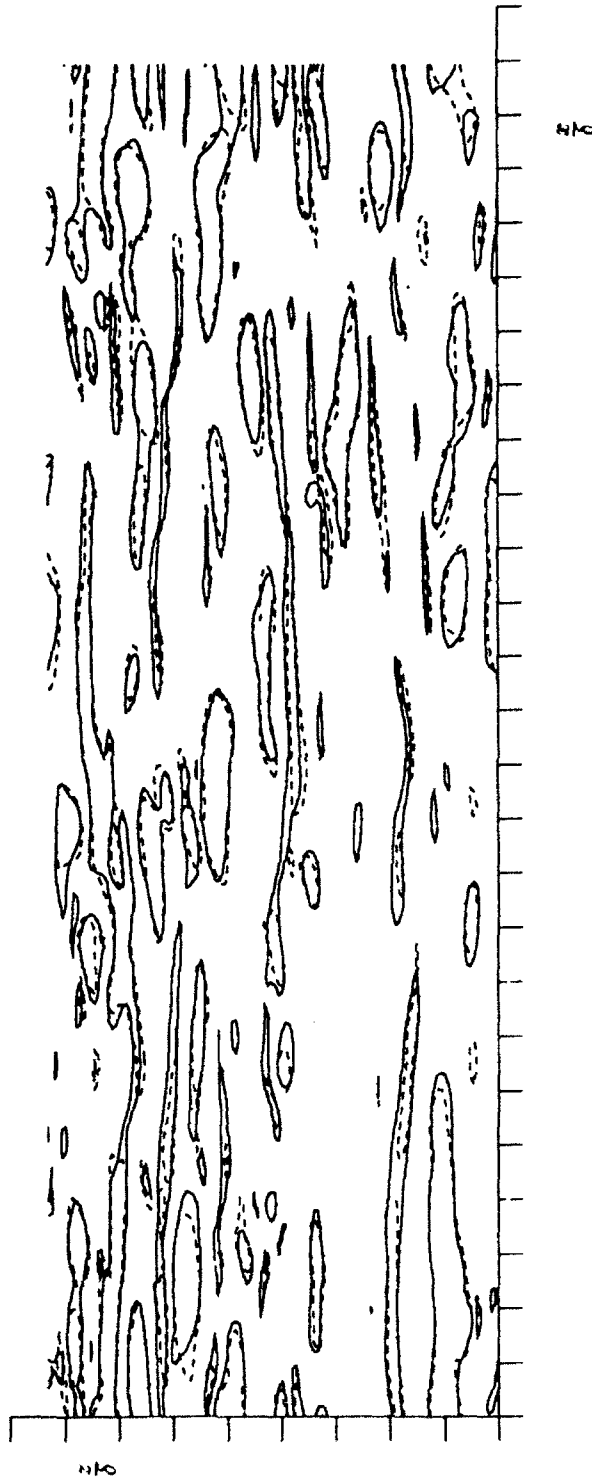


FIGURE 4.18. Contours of $|u'| = 2u_{r2D}$ for 2D (—) and shifted 3D (- - -) companion flows at $y_{2D}^* = 5$ and $t=0.3$. The spacing between tic marks is 0.5

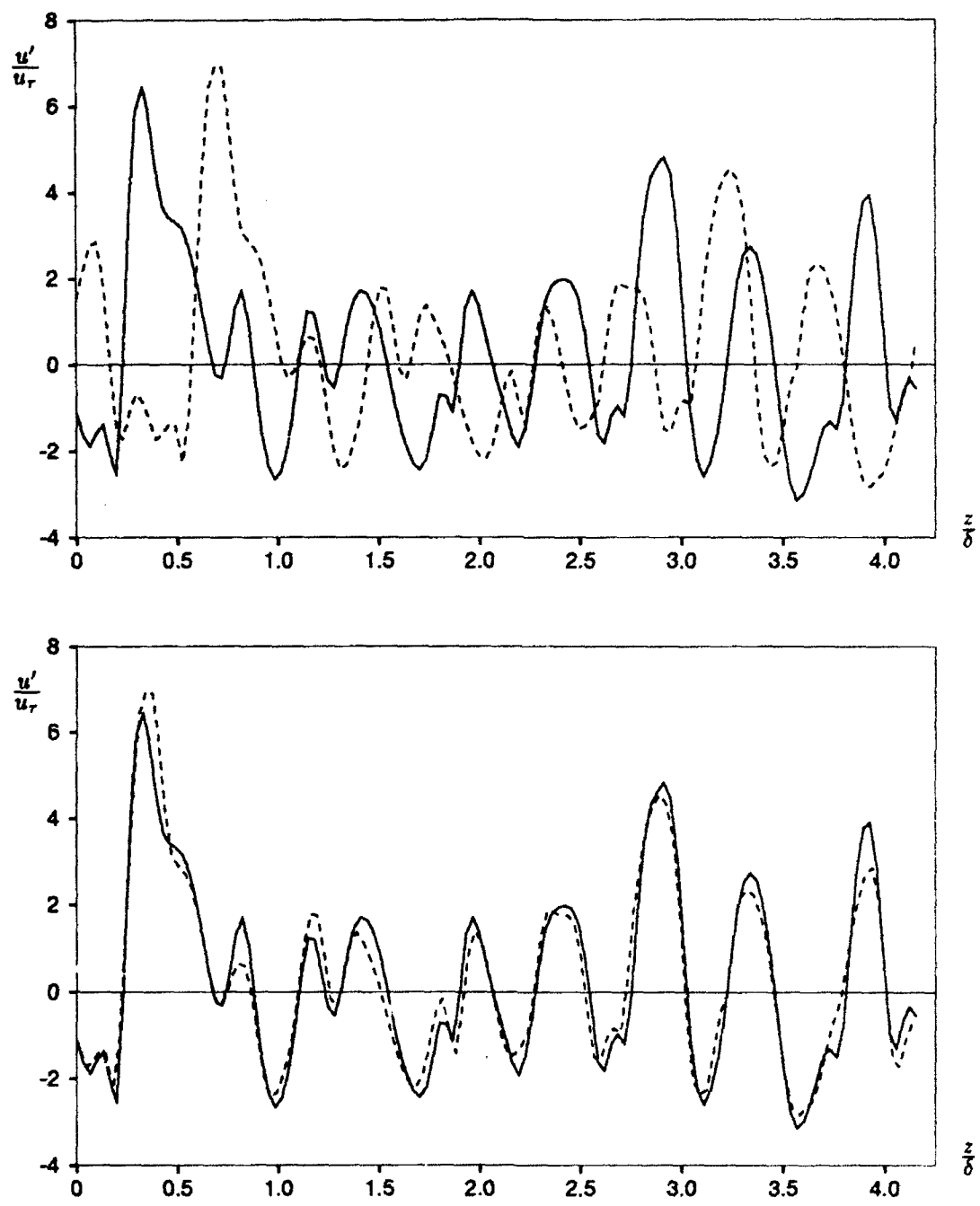


FIGURE 4.19. A spanwise trace of u' in 2D (—) and 3D (- - -) companion flows (a) unshifted and (b) shifted in the z -direction.

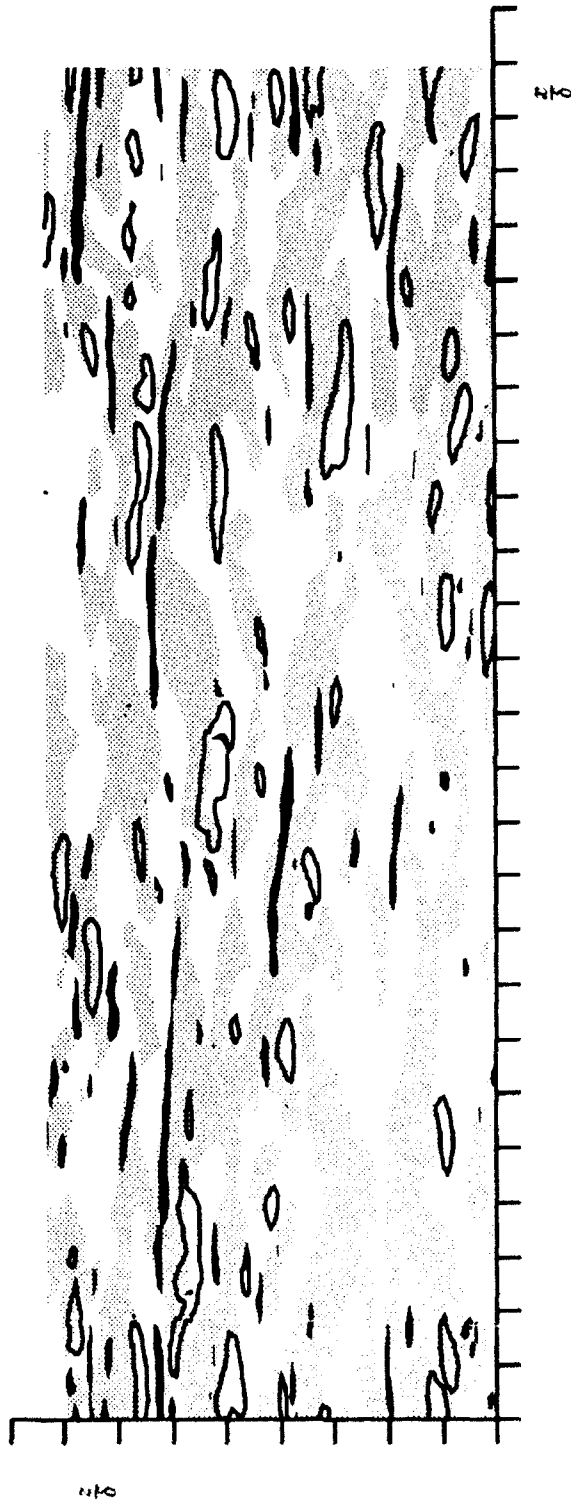


FIGURE 4.20. Companion flows at $y_{2D}^+ = 5$ and $t = 0.3$: $w_{2D}^+ > 0$ (grey), $u_{3D}^{+2} - u_{2D}^{+2} < -2$ with $u_{2D}^+ < 0$ (narrow filled contours) and with $u_{2D}^+ > 0$ (unfilled and broader closed contours). The tick marks are separated by 0.5.

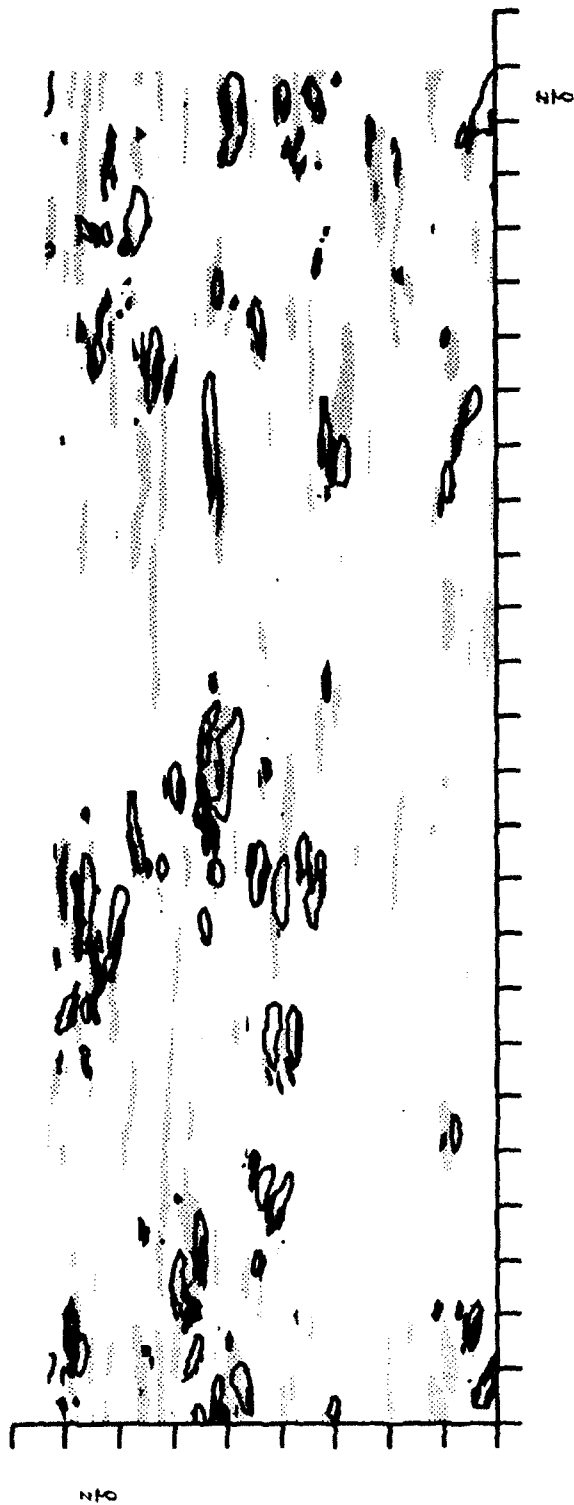


FIGURE 4.21. Shifted companion flows at $y_{2D}^+ = 5$ and $t = 0.3$: $u_{3D}^{I2} - u_{2D}^{I2} < -2$ (grey) $v_{3D}^{I2} - v_{2D}^{I2} < -0.05$ (filled black) $w_{3D}^{I2} - w_{2D}^{I2} < -0.5$ (closed unfilled lines). The tic marks are separated by 0.5.

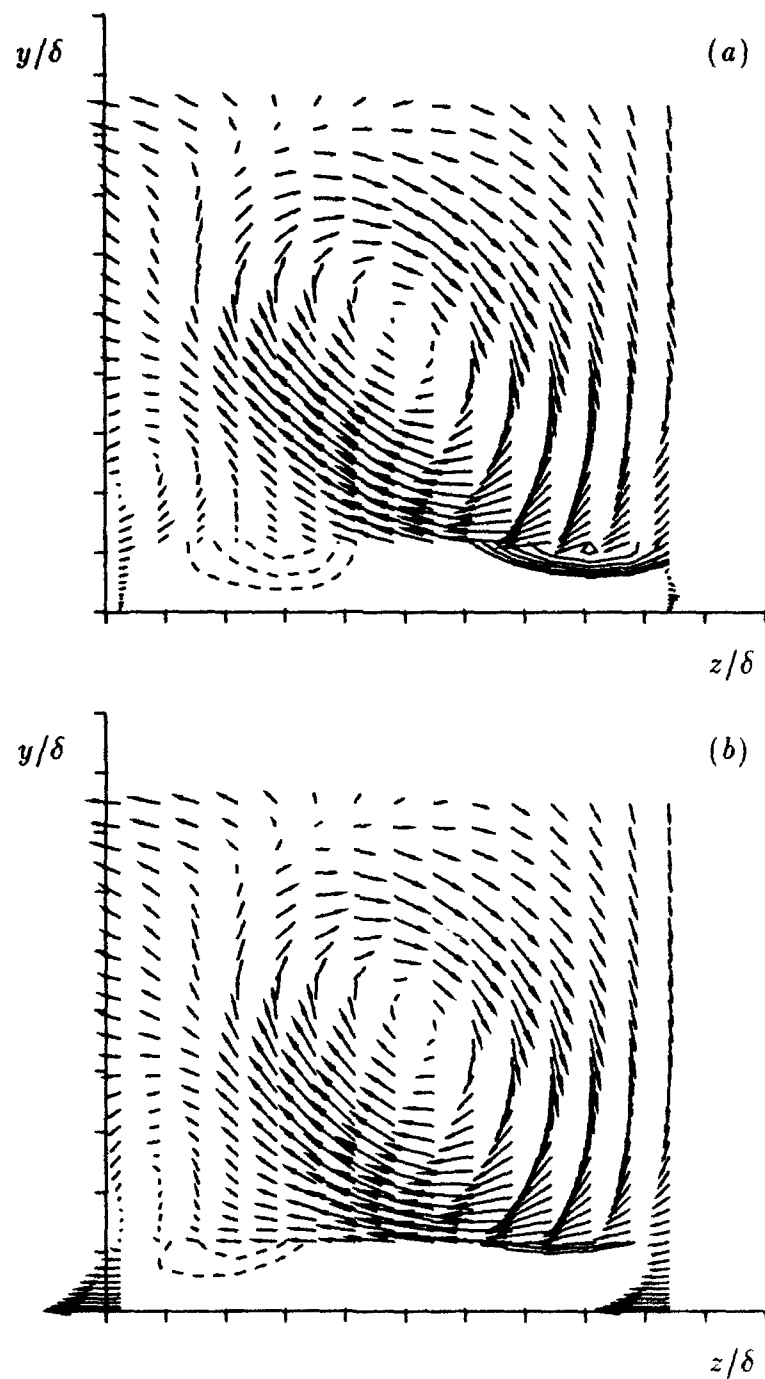


FIGURE 4.22. Sample vortex from the companion flows with positive sign of rotation for (a) 2D flow and (b) 3D flow at $t=0.3$. Contour lines below $y_{2D}^+ = 10$: (—) $u' \geq 5$ with increments $\Delta u' = 0.5$ and (- - -) $u' \leq -1$ with $\Delta u' = -0.5$. The tic marks are separated by 0.05.

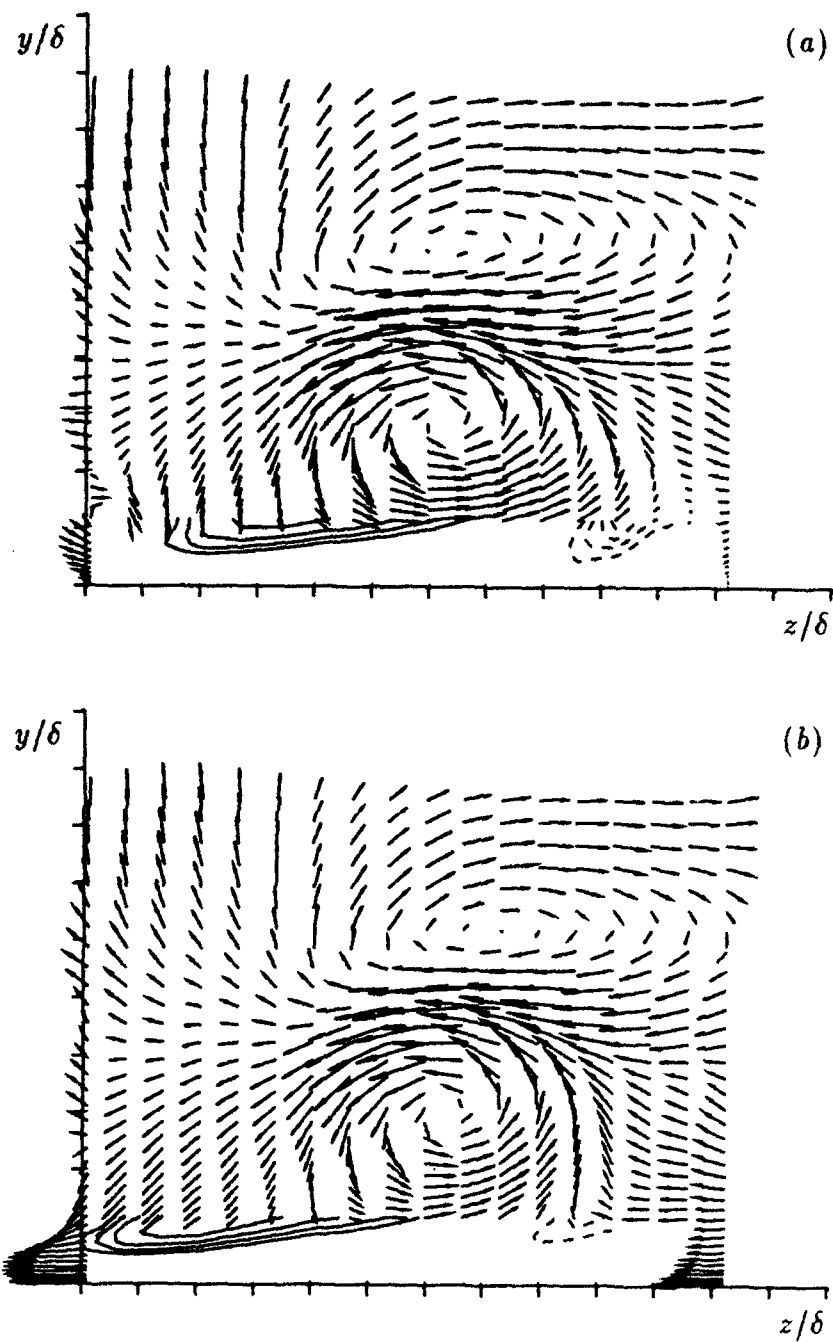


FIGURE 4.23. Sample vortex from the companion flows with negative sign of rotation for (a) 2D flow and (b) 3D flow at $t=0.3$. Contour lines below $y_{2D}^+ = 10$: (—) $u' \geq 4$ with increments $\Delta u' = 0.5$ and (----) $u' \leq -1.5$ with $\Delta u' = -0.5$. The tic marks are separated by 0.05.

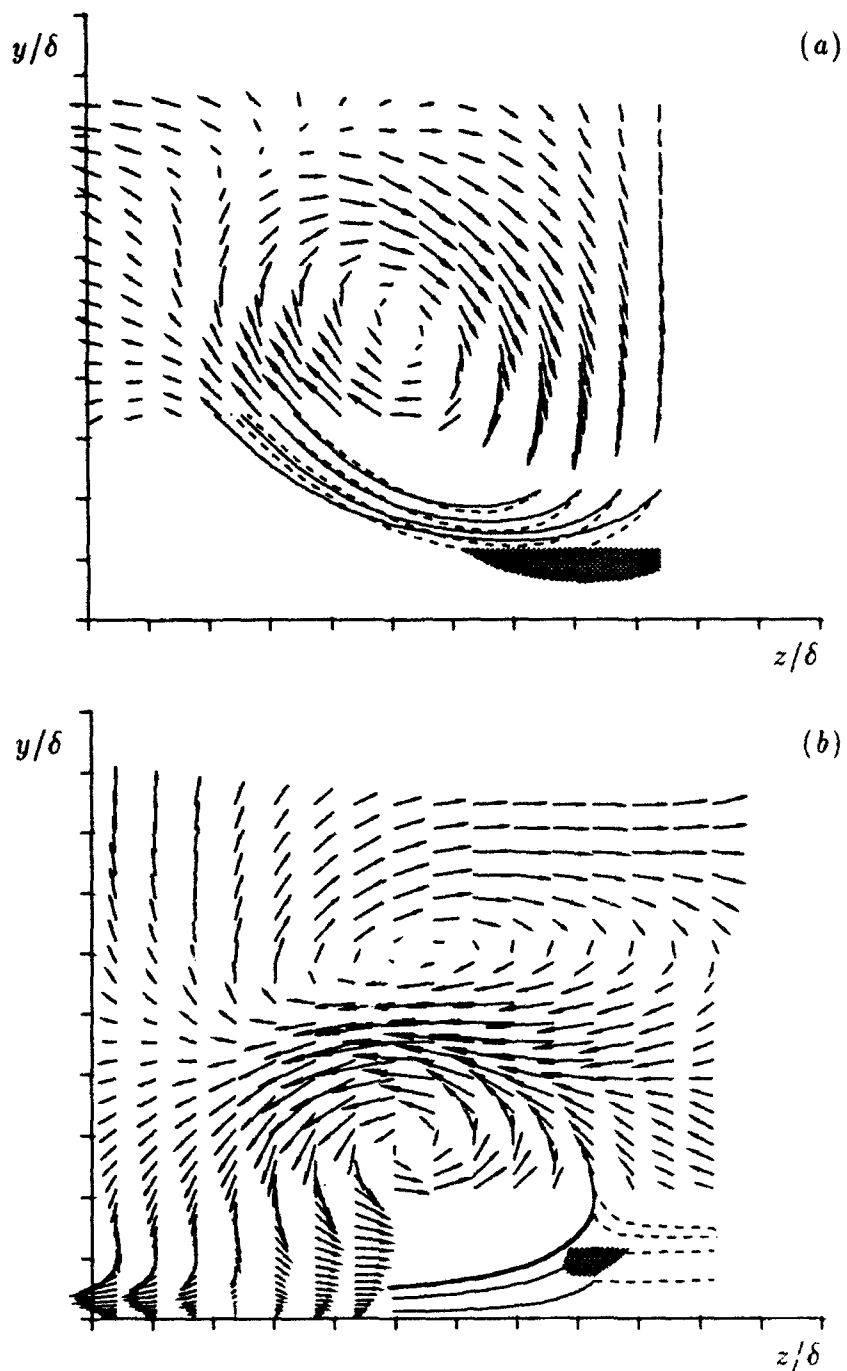


FIGURE 4.24. Segments of "streamlines" within the $z-y$ plane for the sample vortices in Figures 4.22 and 4.23. Lines for the 2D flow (—) and 3D flow (----) are traced from common points. Grey areas represent the lowest contour levels for u'_{2D} in these figures ($u' \geq 5$ in (a) and $u' \leq -1$ in (b)). Tic marks are separated by 0.025.

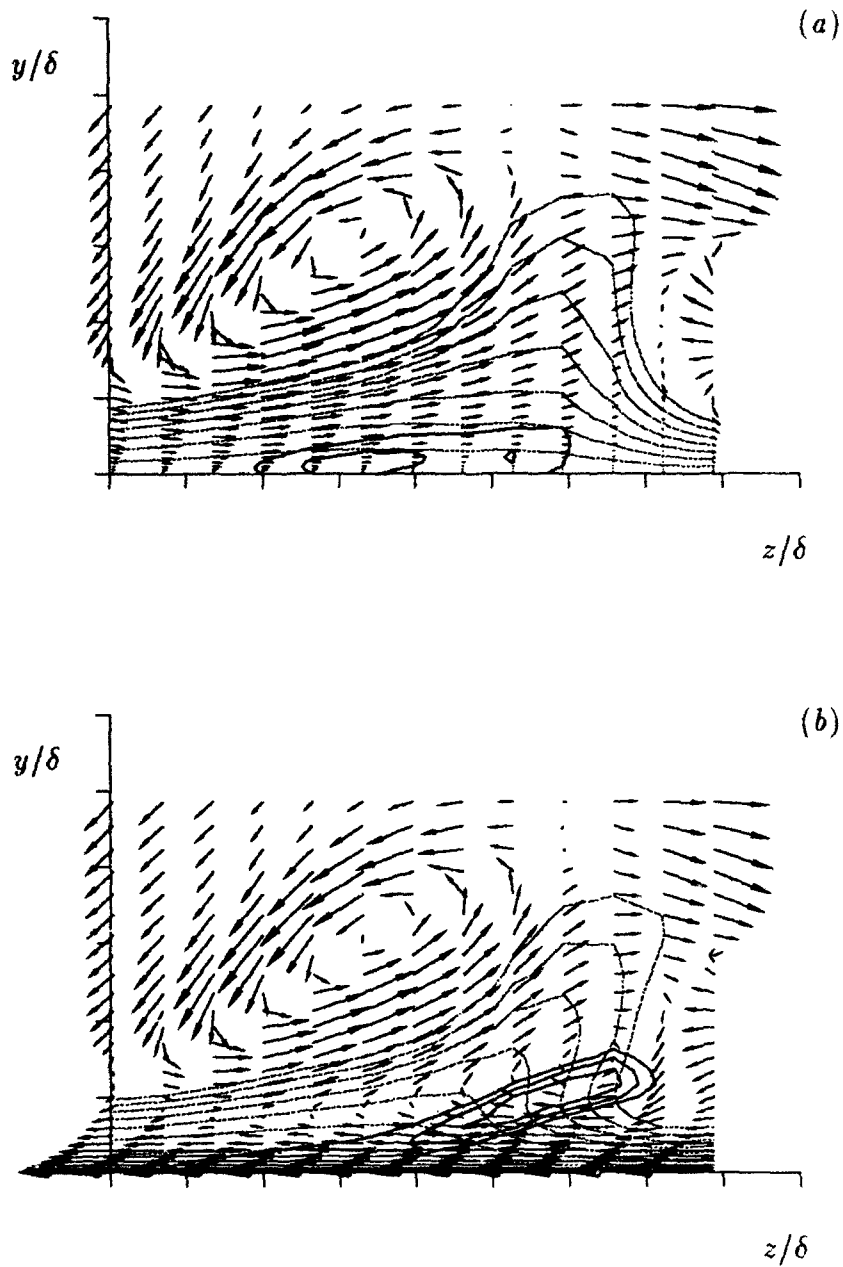


FIGURE 4.25. Sample vortex with a positive sign of rotation from (a) the 2D and (b) the 3D companion flows at $t=0.3$. Solid lines show contours of $\frac{\partial u'}{\partial y} < -100$ with increment 10. Dotted lines show $u \leq 7$ with increment 1. Tic marks are separated by 0.05.

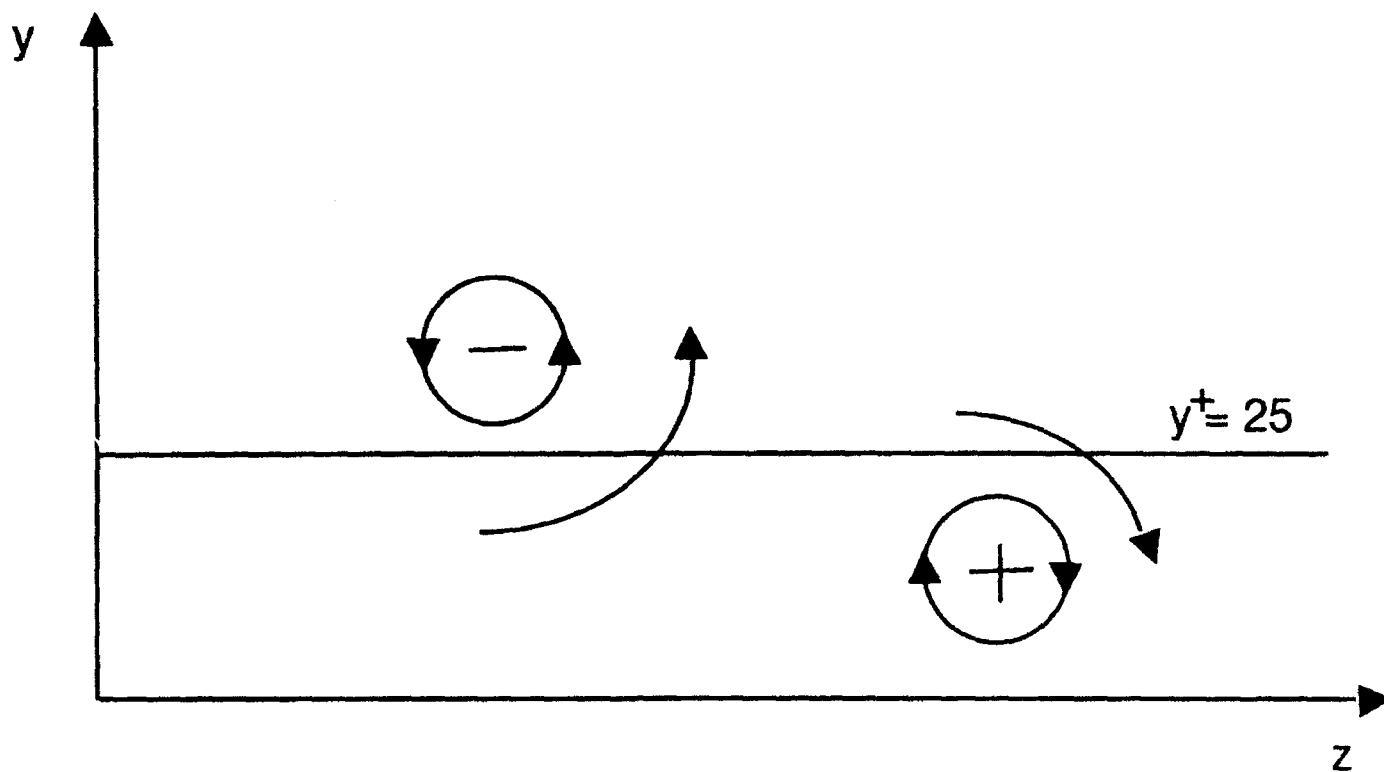


FIGURE 4.26. Schematics showing the events in which $u'v'$ is most reduced at $y_{2D}^+ = 25$.

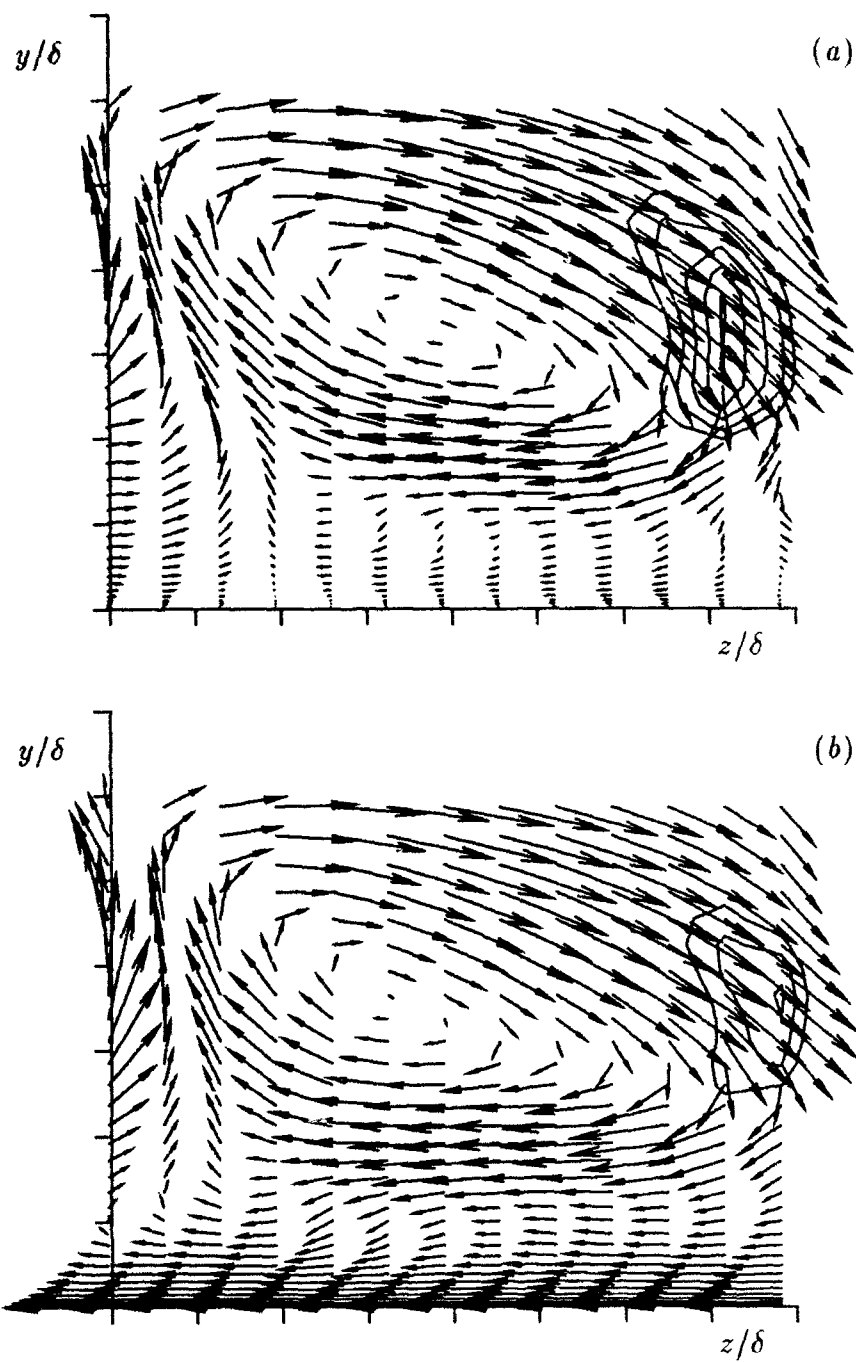


FIGURE 4.27. Contours of $u'v'$ with $u' > 0$ and $v' < 0$ outside spanwise TBL for a vortex in the (a) 2D and (b) 3D companion flows at $t=0.3$. Contour lines: $u'v' \leq -2$ with increment -1. Tic marks are separated by 0.05.

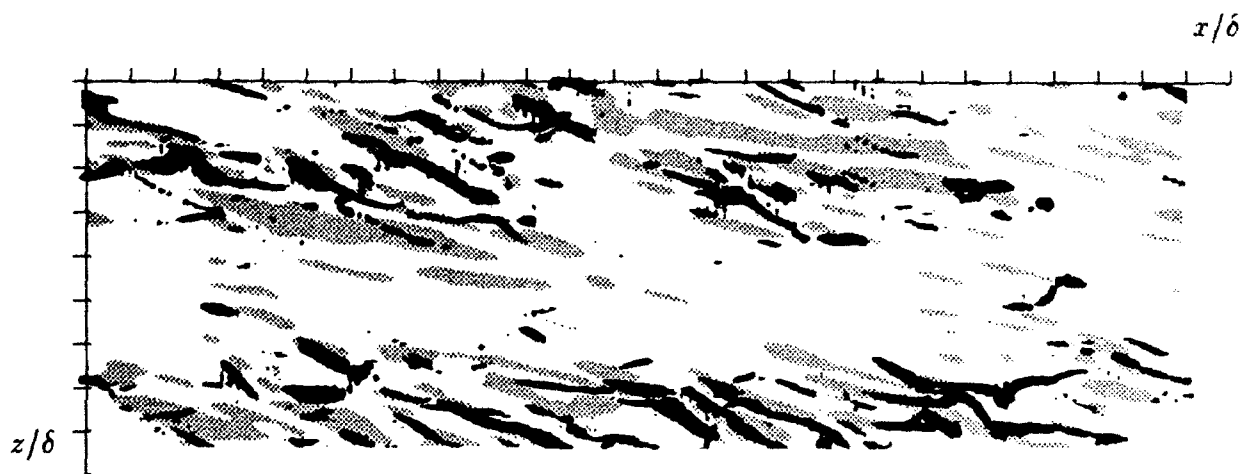


FIGURE 4.28. Top view of streaks ($|\frac{\partial u'}{\partial y}| > 50$ at the wall, shaded grey) and vortices ($|\omega'_x| > 60$) for (a) $t=0.45$ and (b) $t=0.6$. Tic marks are separated by 0.5.

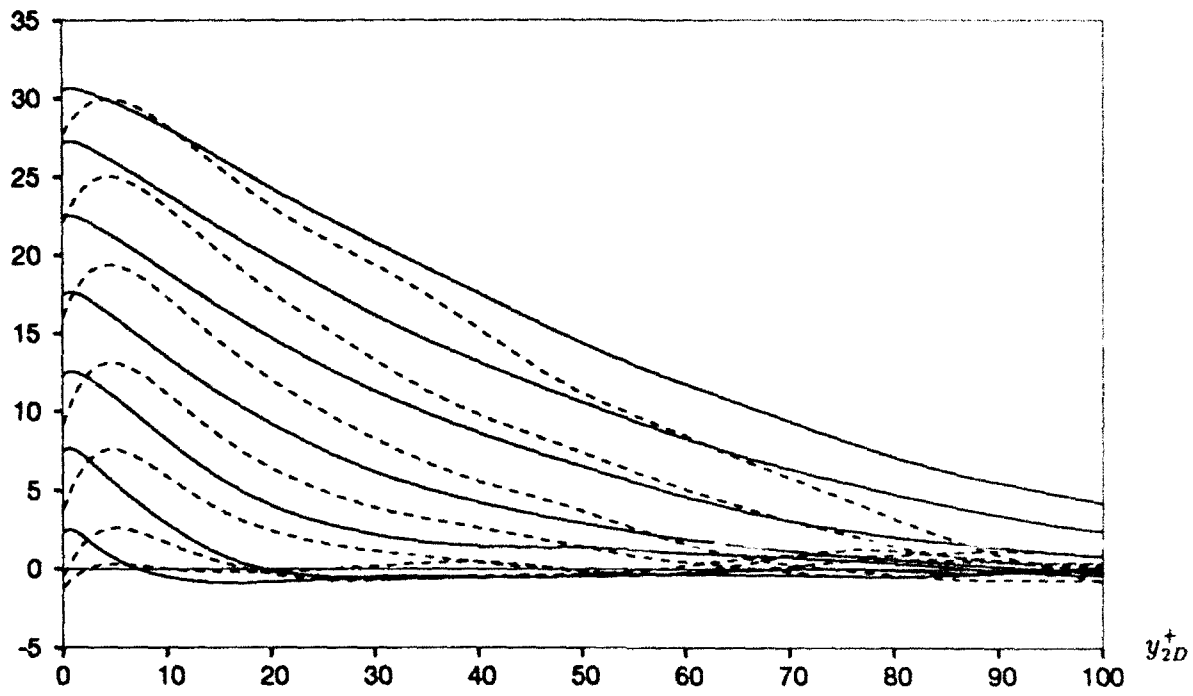


FIGURE 4.29. Angle of maximum Reynolds shear stress (—) and angle of maximum velocity intensity (----). Starting from $t=0.15$ with increments, $\Delta t = 0.15$.

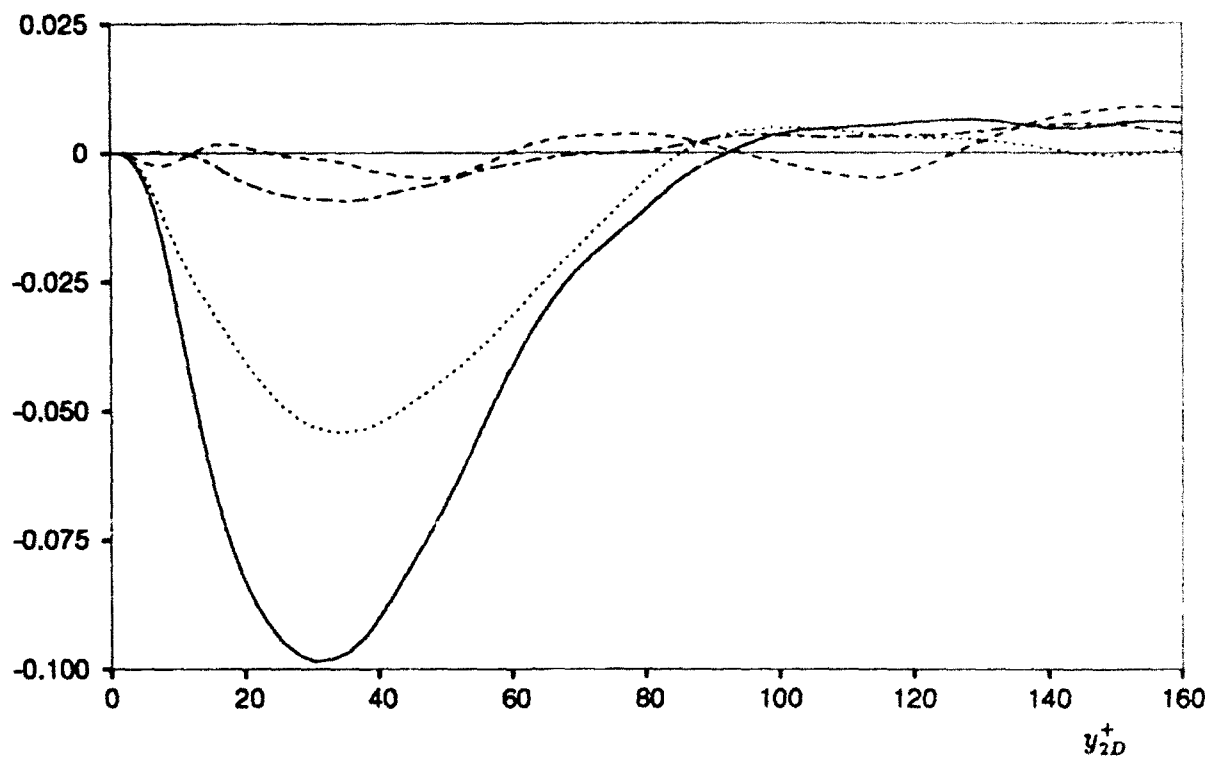


FIGURE 4.30. Change in magnitudes of the contributions from each quadrant for $\overline{u'_2 v'_2}$ in coordinates aligned with the Reynolds shear stress at $t=0.6$. $u' > 0$ and $v' > 0$ (---), $u' < 0$ and $v' > 0$ (—), $u' < 0$ and $v' < 0$ (- - - -), $u' > 0$ and $v' < 0$ (.....).

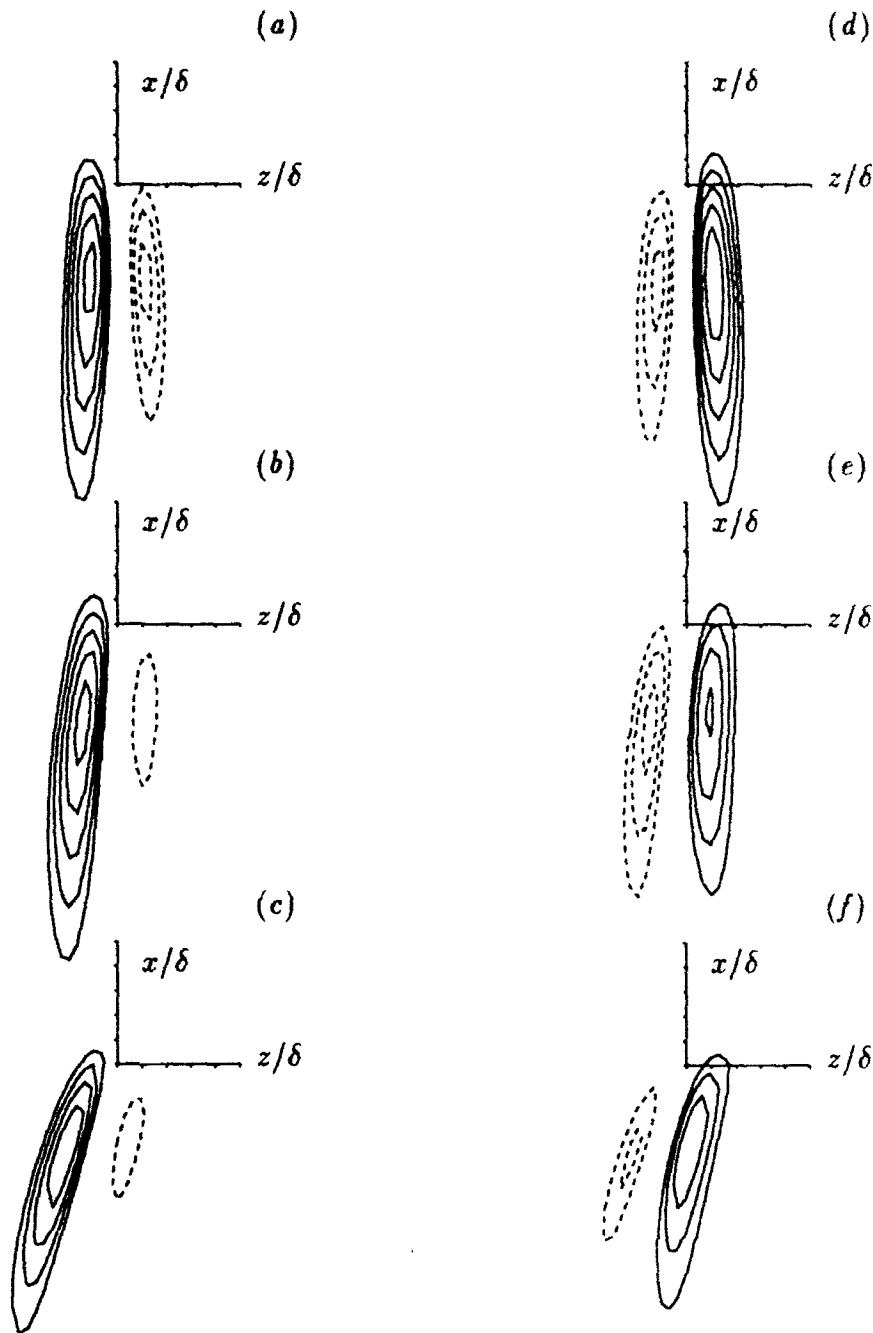


FIGURE 4.31. Conditionally averaged field of u'_* at $y_{2D}^+ = 5$ around $20 < \frac{\partial w'_*}{\partial y} < 50$ in a, b, c and $-50 < \frac{\partial w'_*}{\partial y} < -20$ in d, e, f at the wall. $t=(0., 0.3, 0.6)$ in (a, b, c) and (d, e, f) respectively. The positive contours (—) start from 0.5 with increment 0.1 and negative contours (- - -) from -0.5 with increment -0.1. u'_* , w'_* are unrotated for $t=0.0, 0.3$ and rotated with the intensity angle (eqn. 2.1d) for $t=0.6$. Tic marks are separated by 0.1.

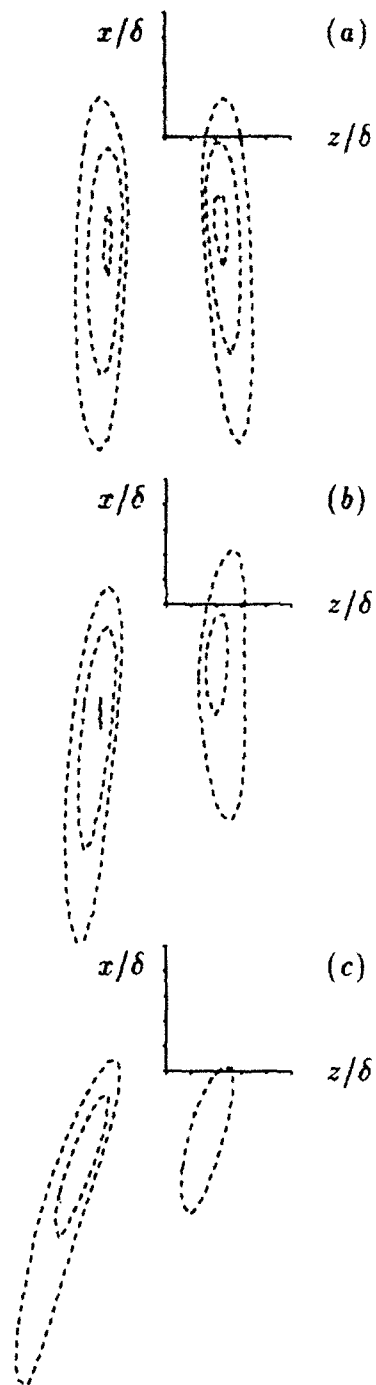


FIGURE 4.32. Top view of the average field of negative u'_* (rotated with the intensity angle, eqn. 2.1*d*) at $y_{2D}^+ = 5$ around $-0.25 < v < -0.2$ at $y_{2D}^+ = 10$. Starting with $u'_* = -0.2$, the increment is $\Delta u'_* = -0.1$. (a) $t=0.0$, (b) $t=0.3$. Tic marks are 0.1 apart, and (c) $t=0.6$.

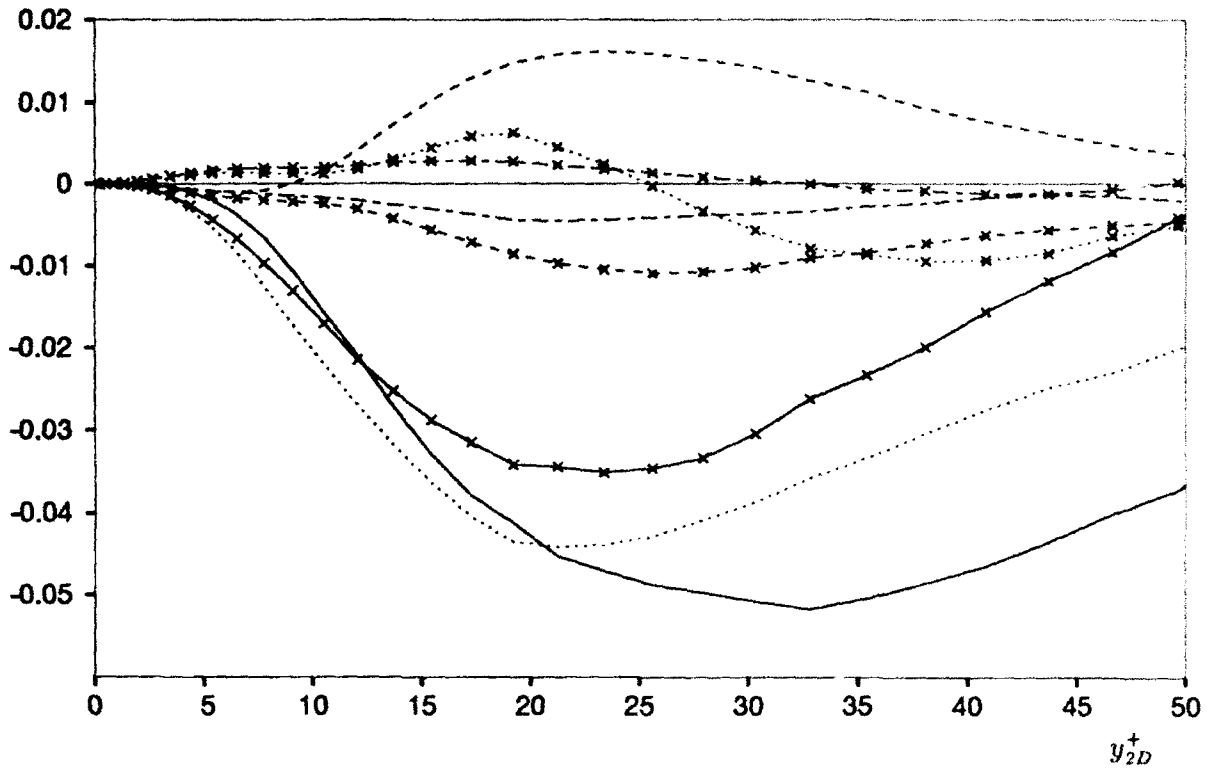


FIGURE 4.33. Change in magnitude of the contribution from each octant to $\overline{u'_* v'}$ at $t=0.6$ in coordinates aligned with the Reynolds shear stress. $u'_* > 0$ and $v' > 0$ (---), $u'_* < 0$ and $v' > 0$ (—), $u'_* < 0$ and $v' < 0$ (-.-.-), $u'_* > 0$ and $v' < 0$ (.....). Symbols (x) represents $w'_* < 0$ and no symbols represents $w'_* > 0$.

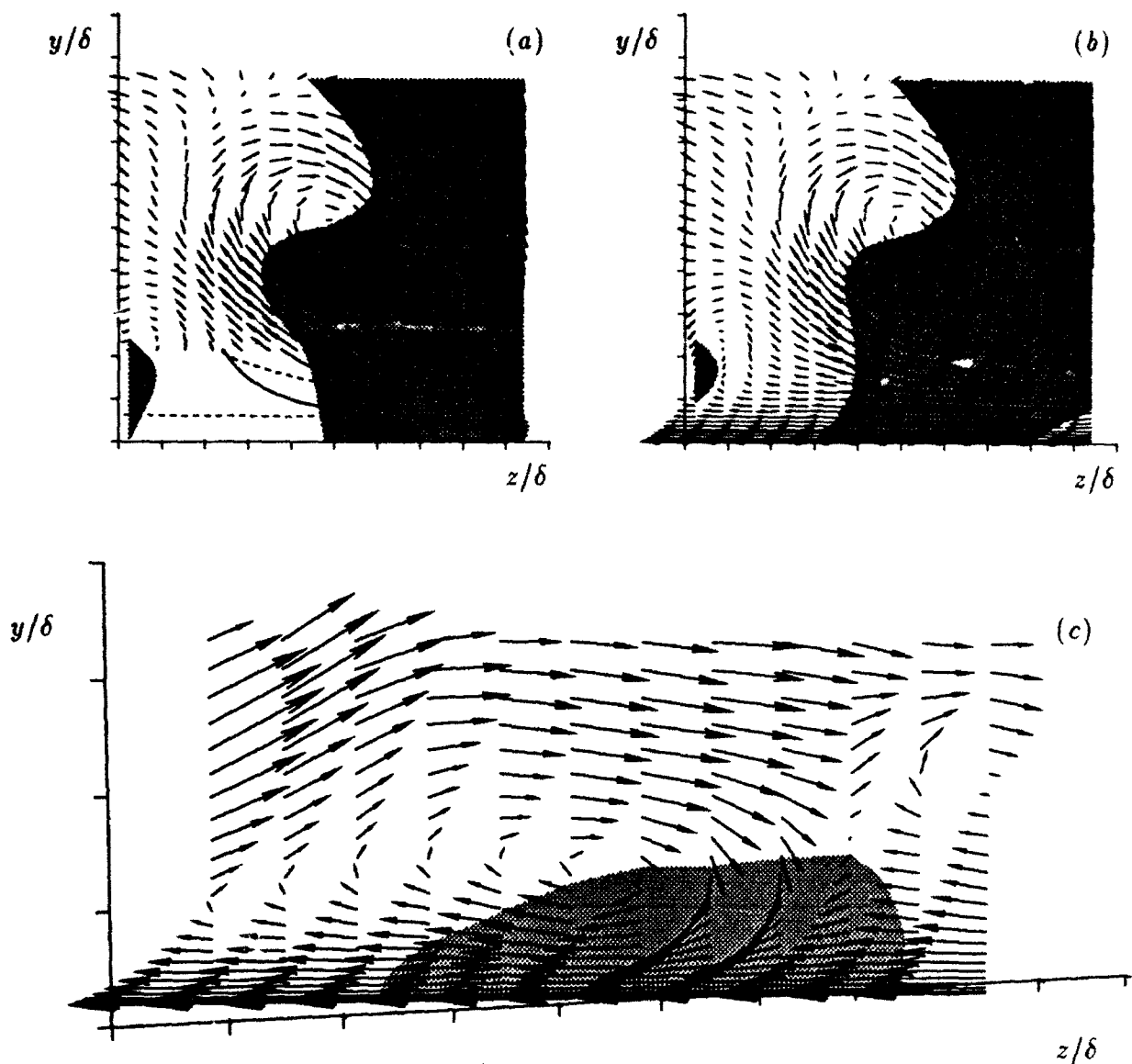


FIGURE 4.34. Regions of $u' > 0$ (grey) extend toward the ejection-region in 3D. This effect is weak during the initial period as seen by comparing the 2D (a) and the 3D (b) companion flows at $t=0.3$. At $t=0.6$ (c) the effect is much stronger. In addition, the particle trajectories will be altered by the cross-flow. This effect is seen in (a) where some "streamlines" for both the 2D (—) and the 3D (----) companion flows are shown traced from common starting points. This effect will increase in importance with increasing spanwise boundary layer thickness.

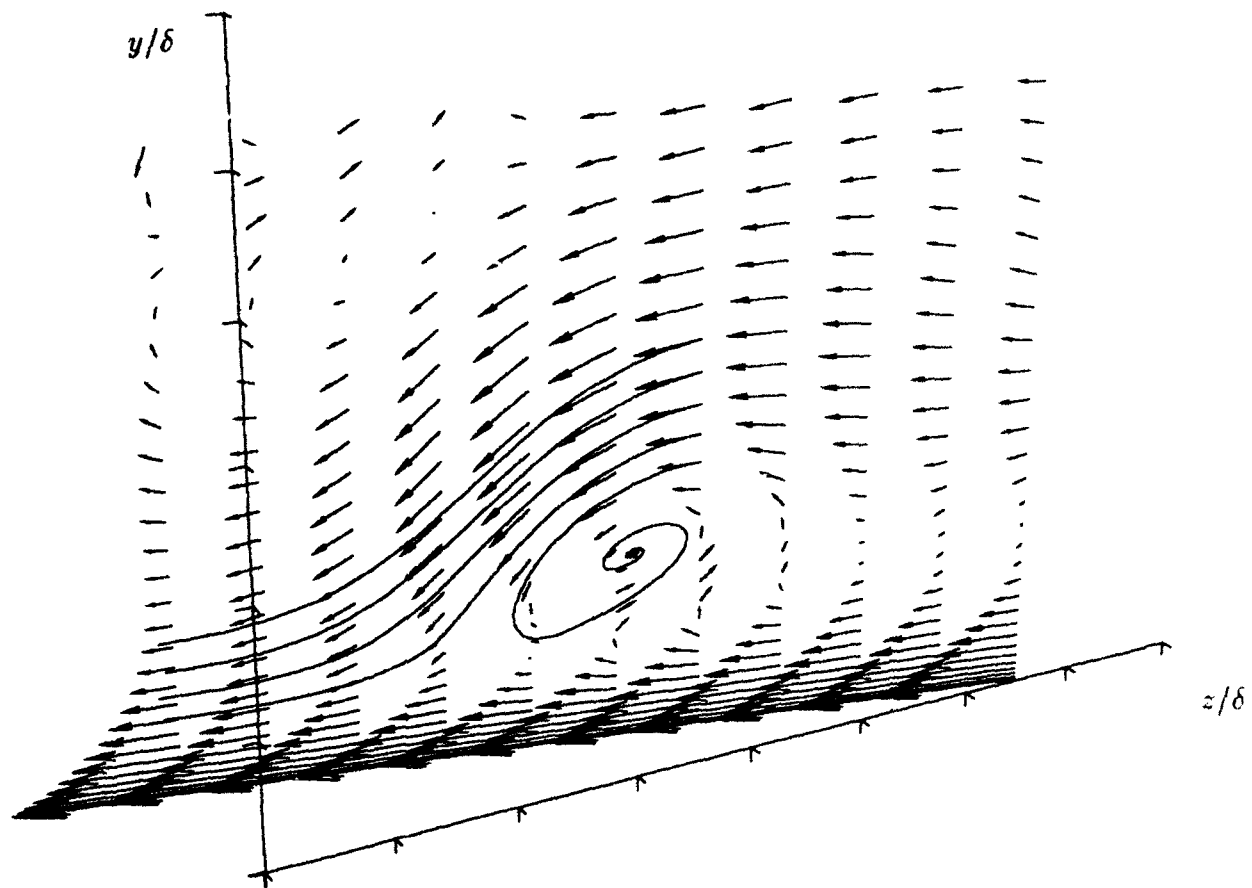


FIGURE 4.35. "Streamlines" for a sample-vortex at $t=0.6$ in a vertical plane rotated 12° .

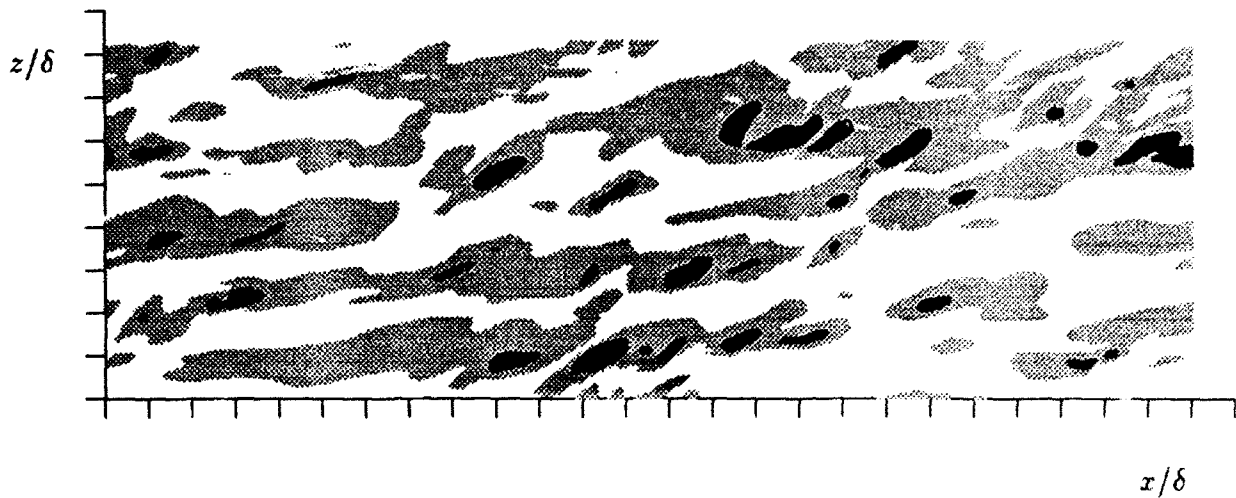


FIGURE 4.36. Contours of $u' > 0$ (grey) and $u' > 3.5$ (black) at $y_{2D}^+ = 10$ with $\frac{\partial P}{\partial z} = -100$.

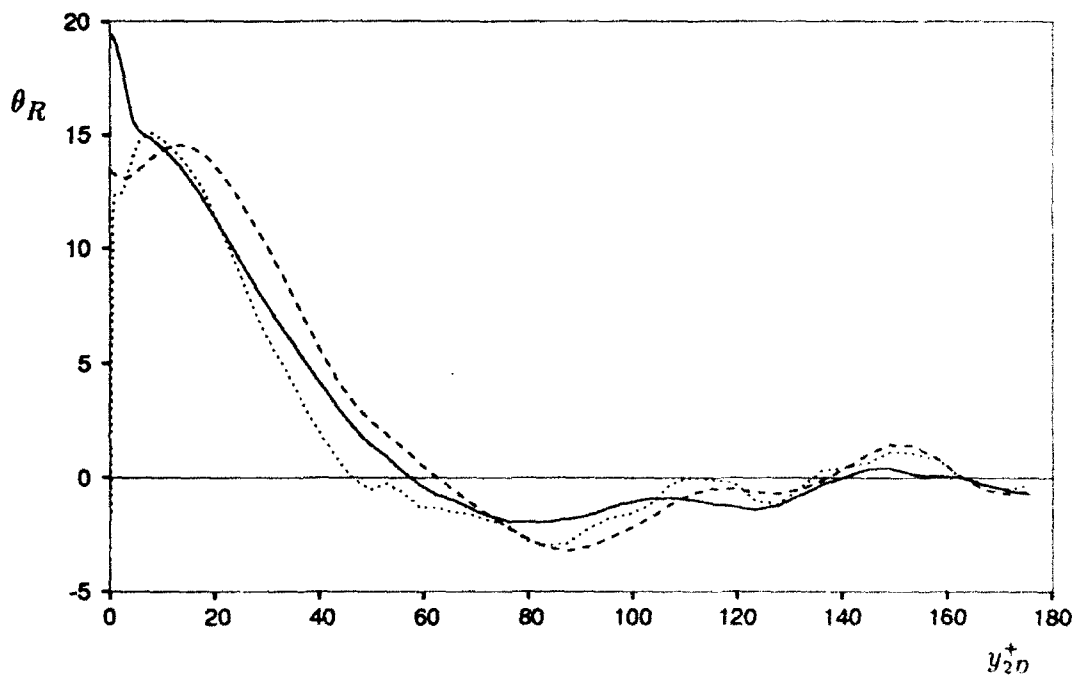


FIGURE 4.37. Estimated vortex-angles at $t=0.6$ from two-point correlations for ω'_{x*} (—) rotated with this angle, p' (----) and $\nabla^2 p'$ (.....).

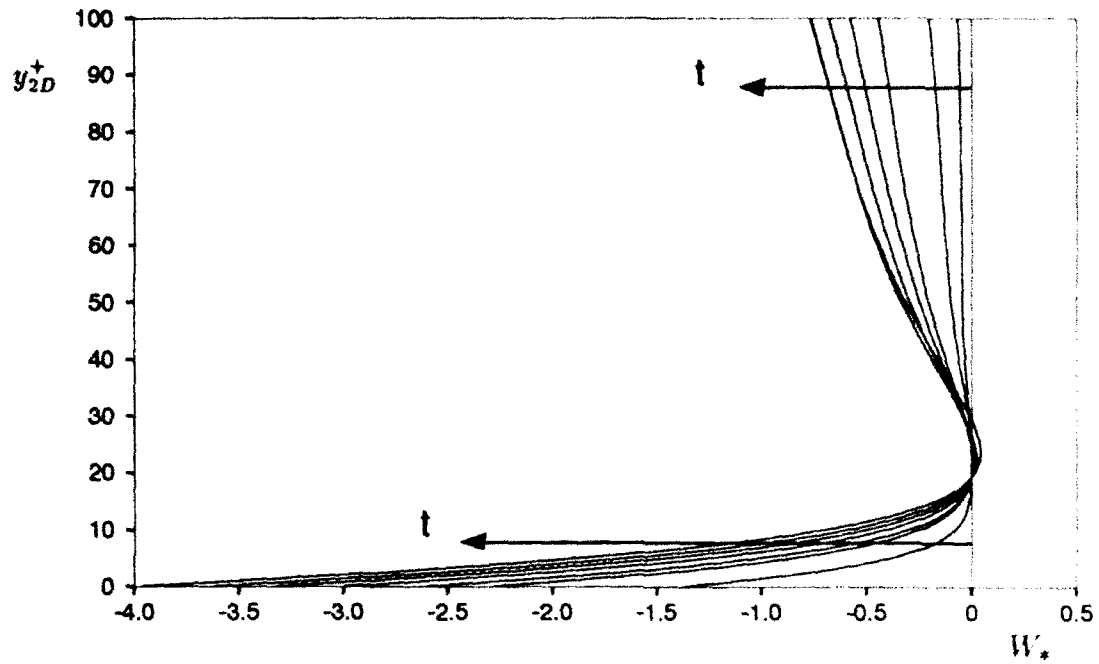


FIGURE 4.38. Spanwise mean velocity evolution in coordinates which are rotated with the average vortex-angle at $y_{2D}^+ = 20$ and move with the mean flow at this location.

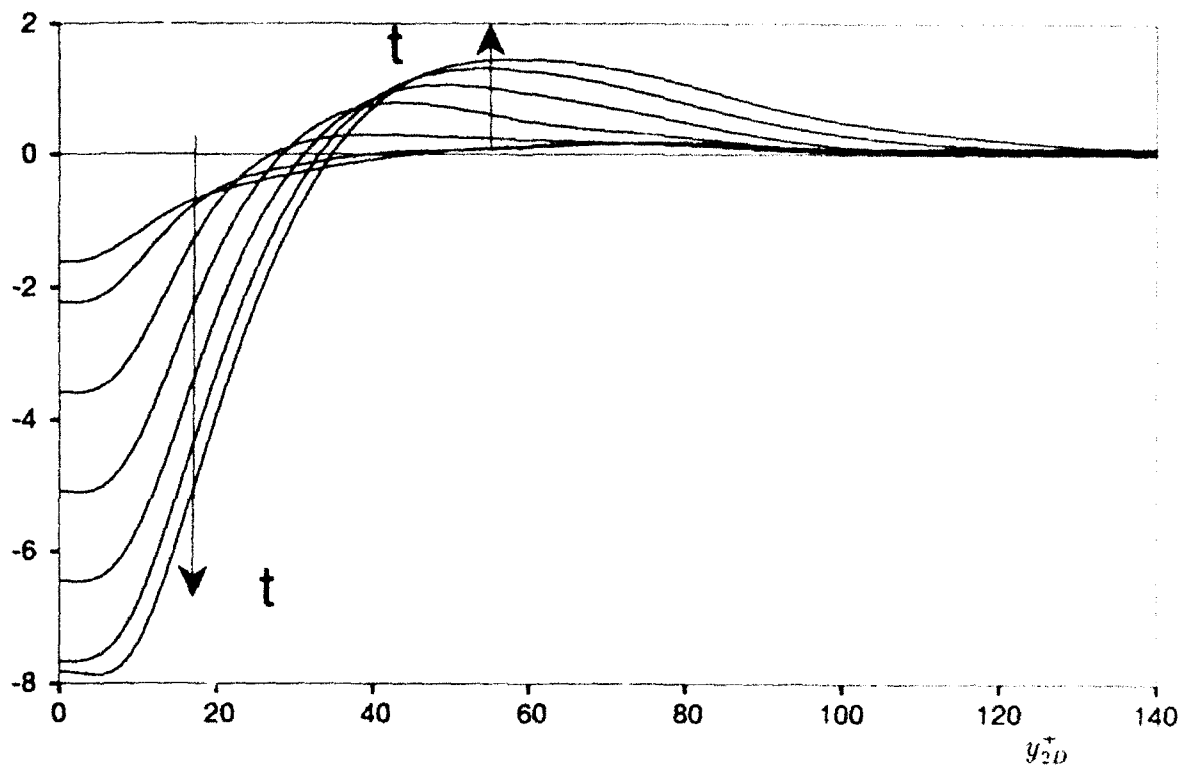


FIGURE 4.39. Percentage reduction in the x -component of the mean velocity, U , starting from $t=0.15$ with increments, $\Delta t = 0.15$.

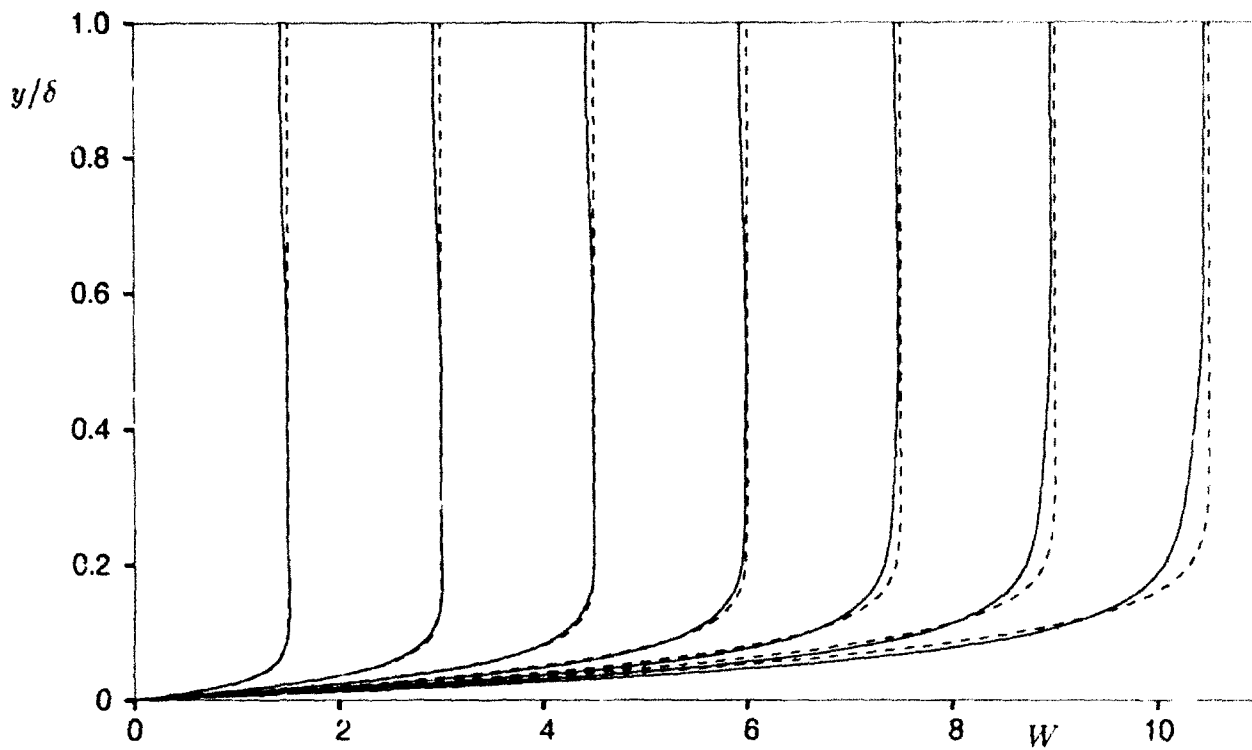


FIGURE 4.40. Evolution of laminar (----) and turbulent (—) spanwise mean velocity profiles, W , starting from $t=0.15$ with increments, $\Delta t = 0.15$.

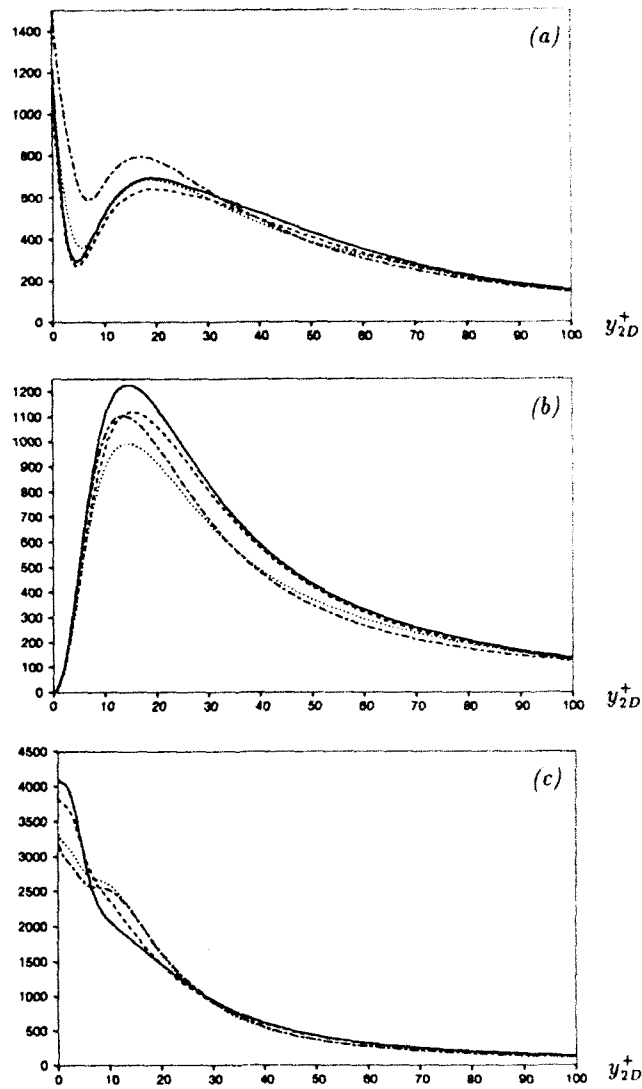


FIGURE 4.41. Profiles of (a) $\overline{\omega_x'^2}$, (b) $\overline{\omega_y'^2}$ and (c) $\overline{\omega_z'^2}$, at $t=0.0$ (—), $t=0.3$ (----), $t=0.6$ (.....) and $t=0.9$ (-.-.).

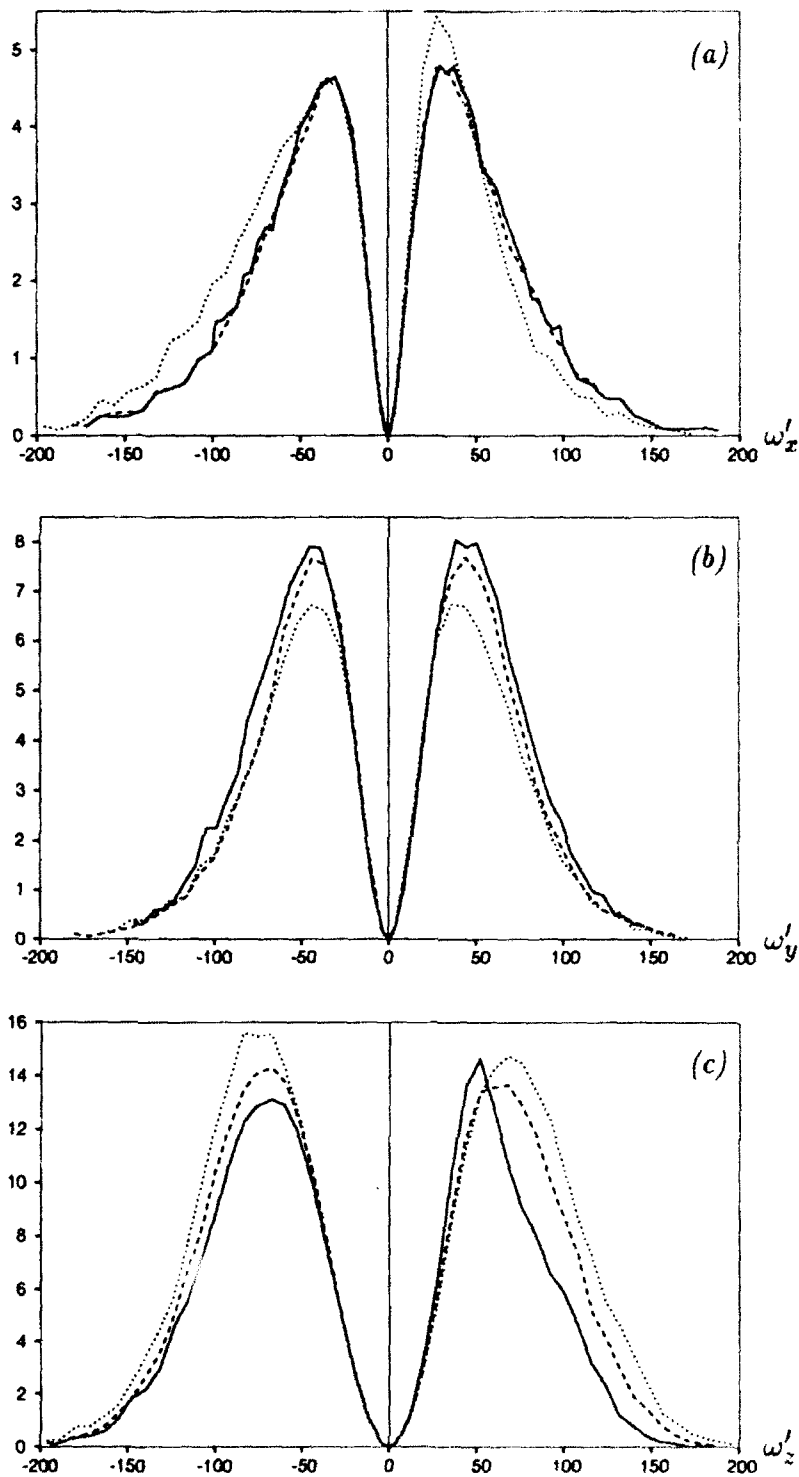


FIGURE 4.42. Intensity-weighted PDF for (a) ω_x , (b) ω_y , and (c) ω_z at $y_{2D}^+ = 20, 10, 10$ respectively. $t=0.0$ (—), $t=0.3$ (----) and $t=0.6$ (.....).

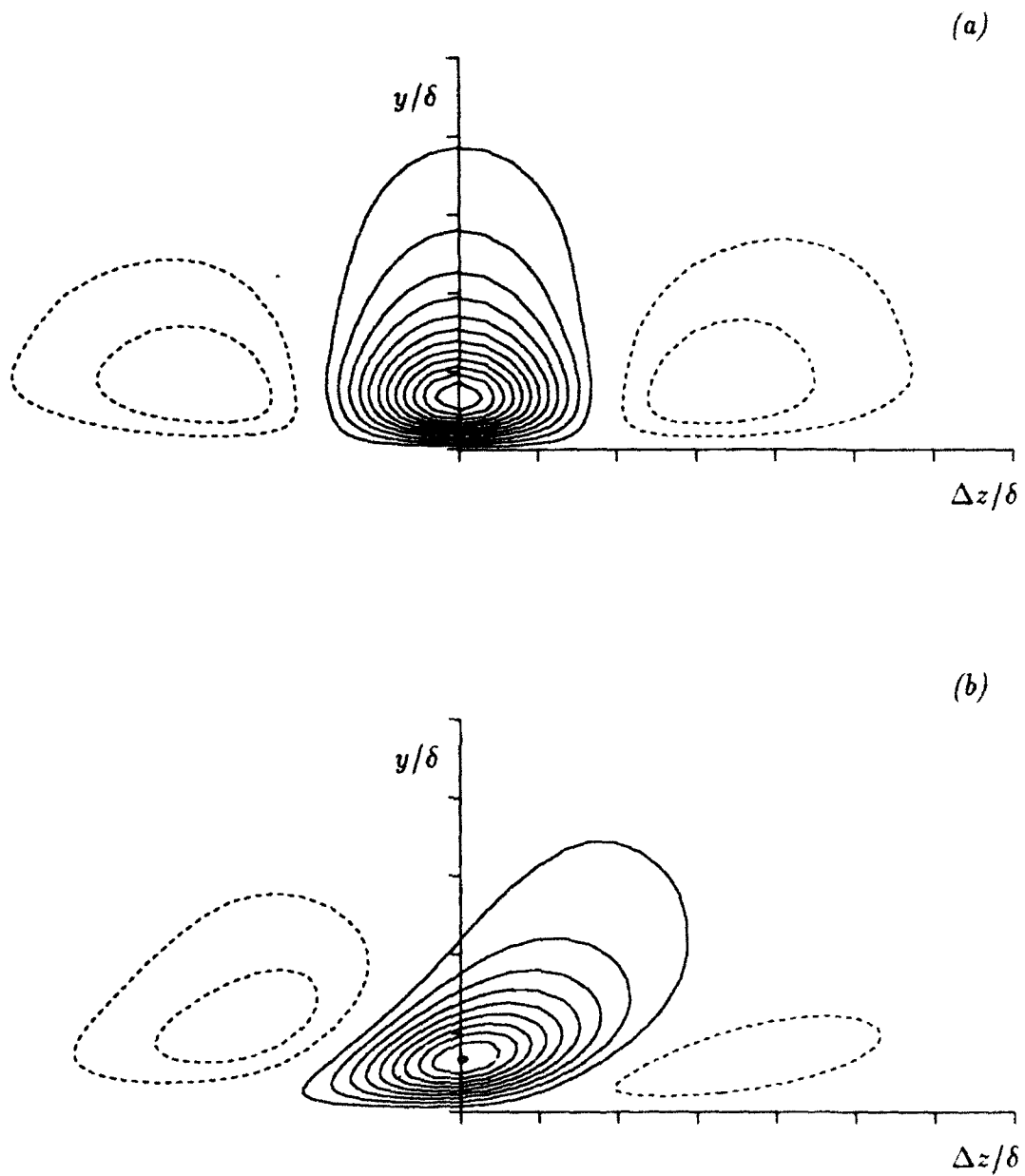


FIGURE 4.43. R_{11} at (a) $t=0$. and (b) $t=0.6$ around $y_{2D}^+ = 10$. Positive contour levels are incremented by 0.5, starting from 1 (—) and negative contours are incremented by -0.5 , starting from -0.5 (----). Tic marks are 0.1 apart.

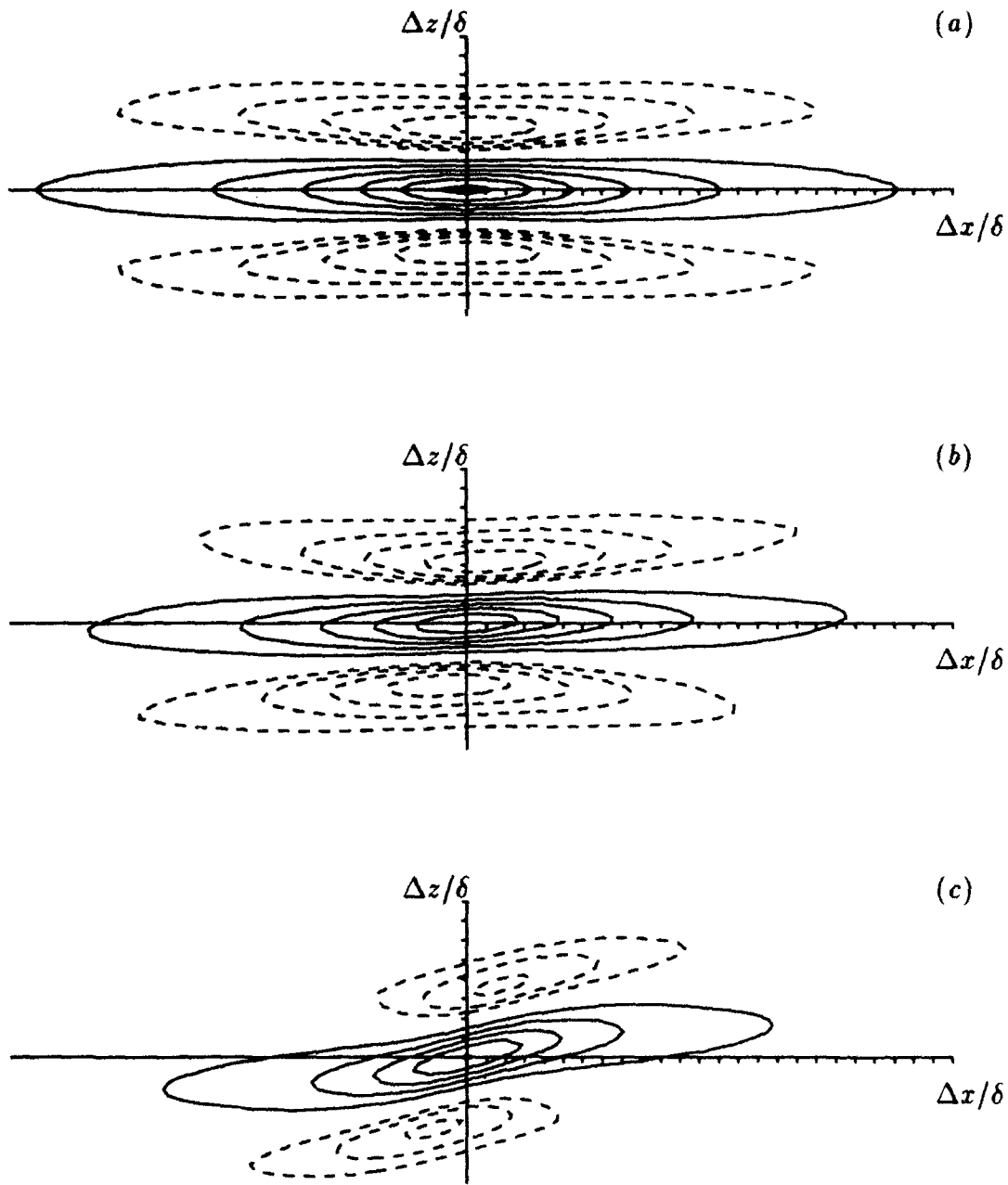


FIGURE 4.44. R_{11*} (based on the velocity components in the direction of maximum intensity) at $y_{2D}^+ = 10$ for (a) $t=0.0$, (b) $t=0.3$ and (c) $t=0.6$. Positive contour levels are incremented by 1, starting from 1 (—) and negative contours are incremented by -0.25 , starting from -0.5 (----). Tic marks are 0.1 apart.

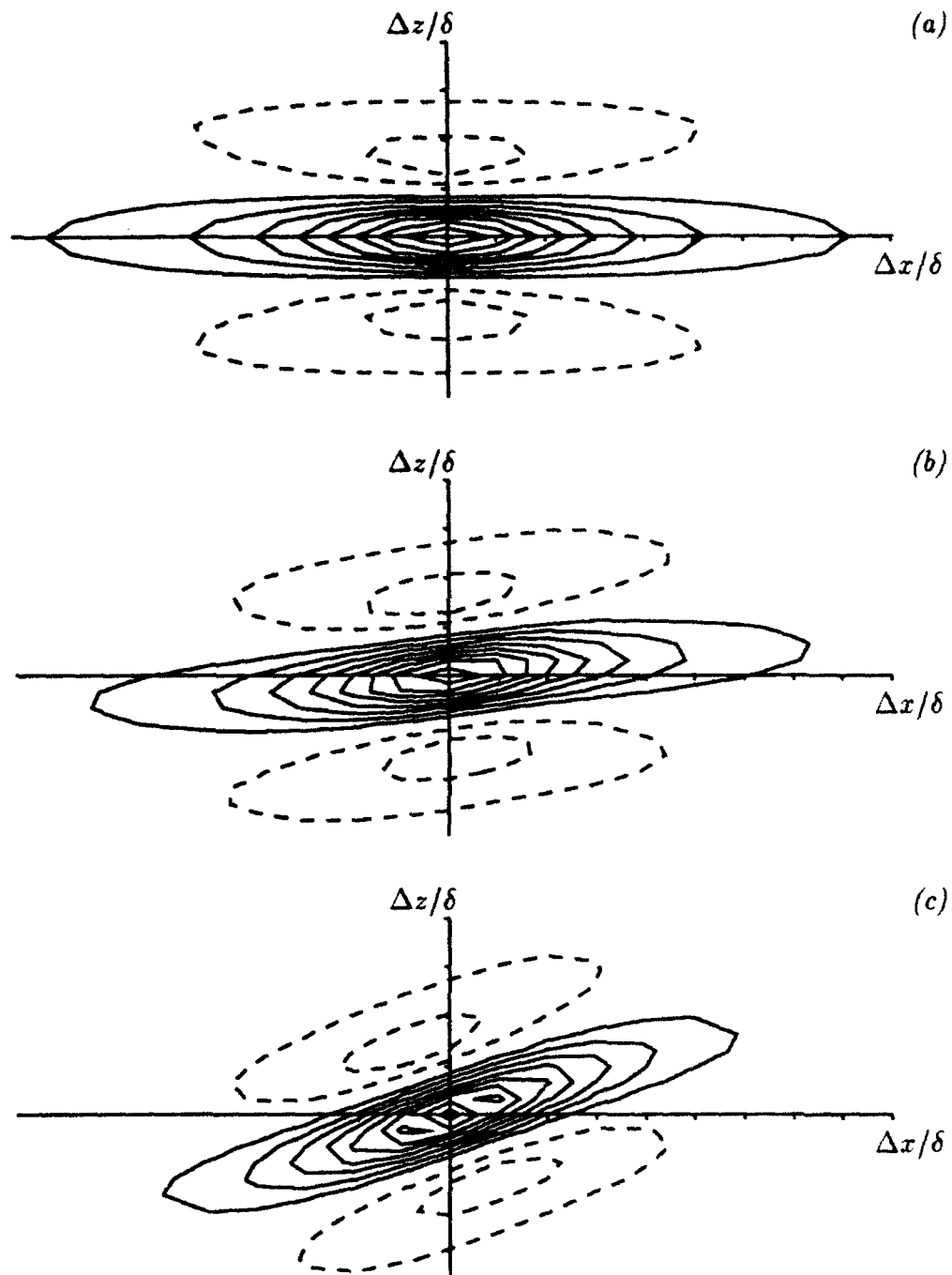


FIGURE 4.45. R_{22} at $y_{2D}^+ = 10$ for (a) $t=0.0$, (b) $t=0.3$ and (c) $t=0.6$. Positive contour levels are incremented by 0.01, starting from 0.01 (—) and negative contours are incremented by -0.01 , starting from -0.01 (- - -). Tic marks are 0.1 apart.

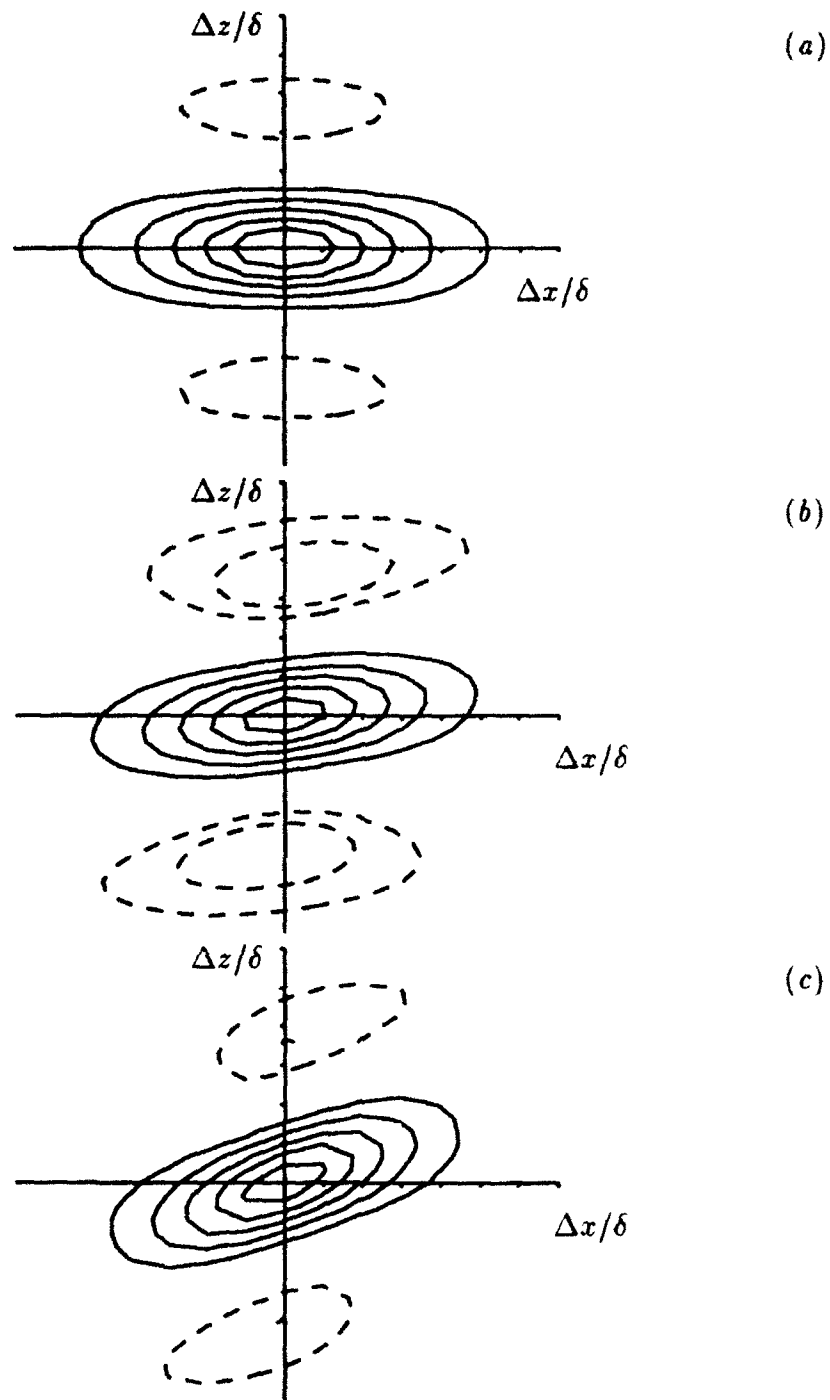


FIGURE 4.46. R_{33*} (based on the velocity components in the direction of maximum intensity) at $y_{2D}^+ = 10$ for (a) $t=0.0$, (b) $t=0.3$ and (c) $t=0.6$. Positive contour levels are incremented by 0.1, starting from 0.2 (—) and negative contours are incremented by -0.005 , starting from -0.025 (----). Tic marks are 0.1 apart.

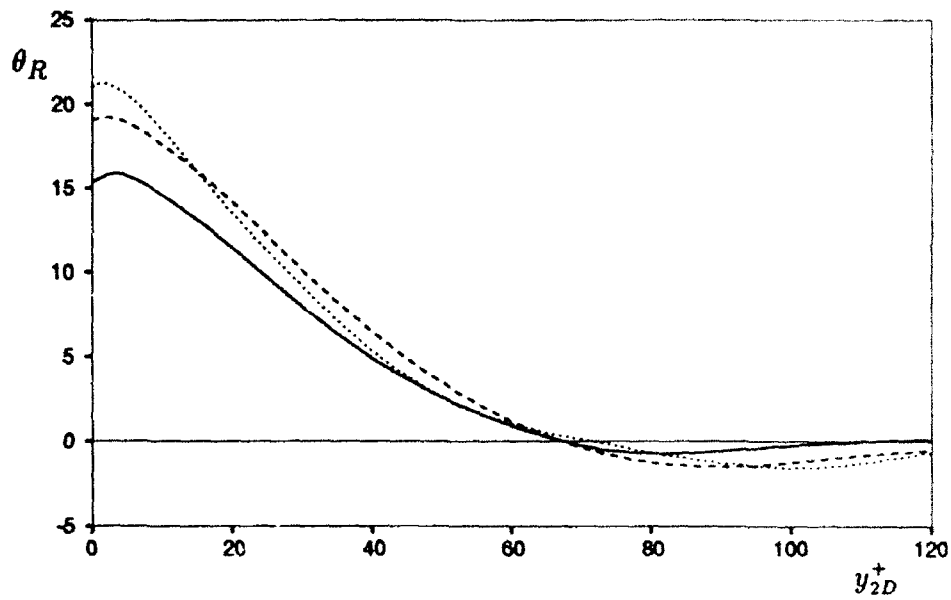


FIGURE 4.47. Angles of maximum correlation in the horizontal plane for (—) R_{11*} ; (----) R_{22} and (.....) R_{33*} at $t=0.6$. The velocity fluctuations are rotated to the direction of maximum streamwise intensity.

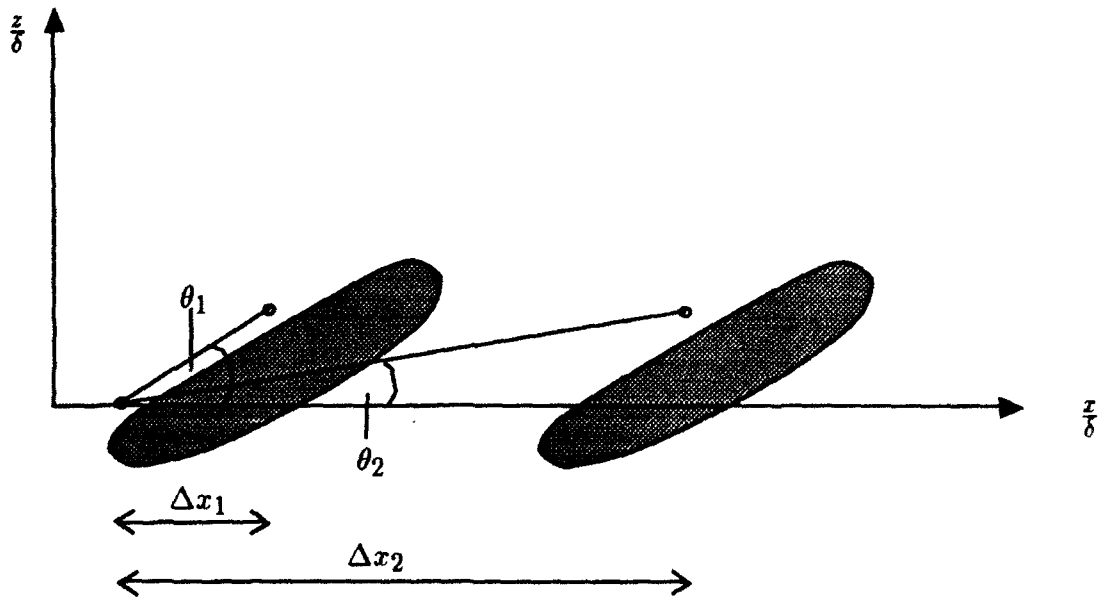


FIGURE 4.48. View of two vortices from below (grey) in 3D flow. Angle for short streamwise separation (θ_1) is larger than the angle for large separations (θ_2).

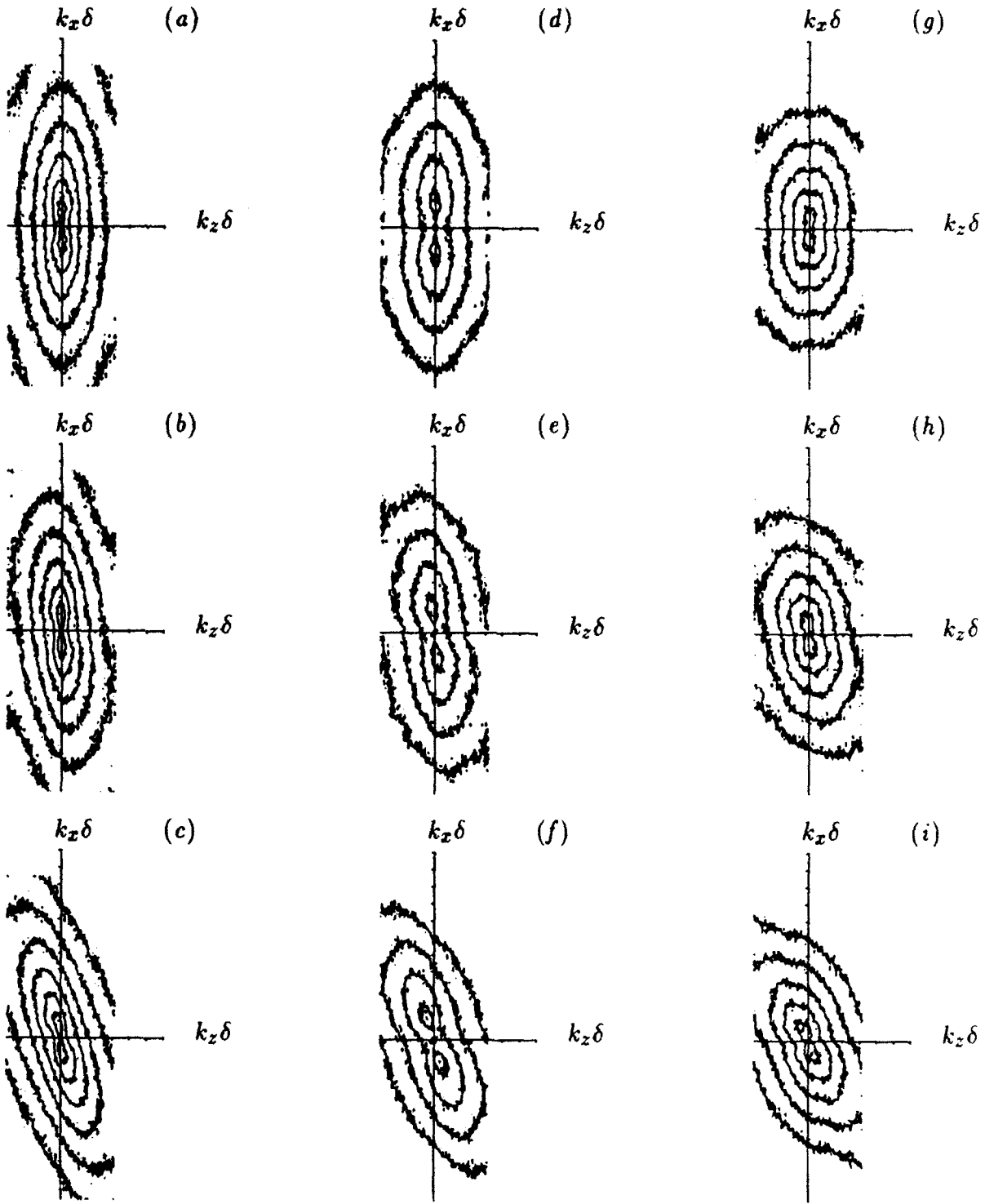


FIGURE 4.49. $E_{11^*}, E_{22}, E_{33^*}$ (left to right) for $t=0, 0.3, 0.6$ (top to bottom) at $y_{2D}^+ = 10$. Contour levels: 0.1, 0.01, 0.001... Spacing between tic marks is 10.

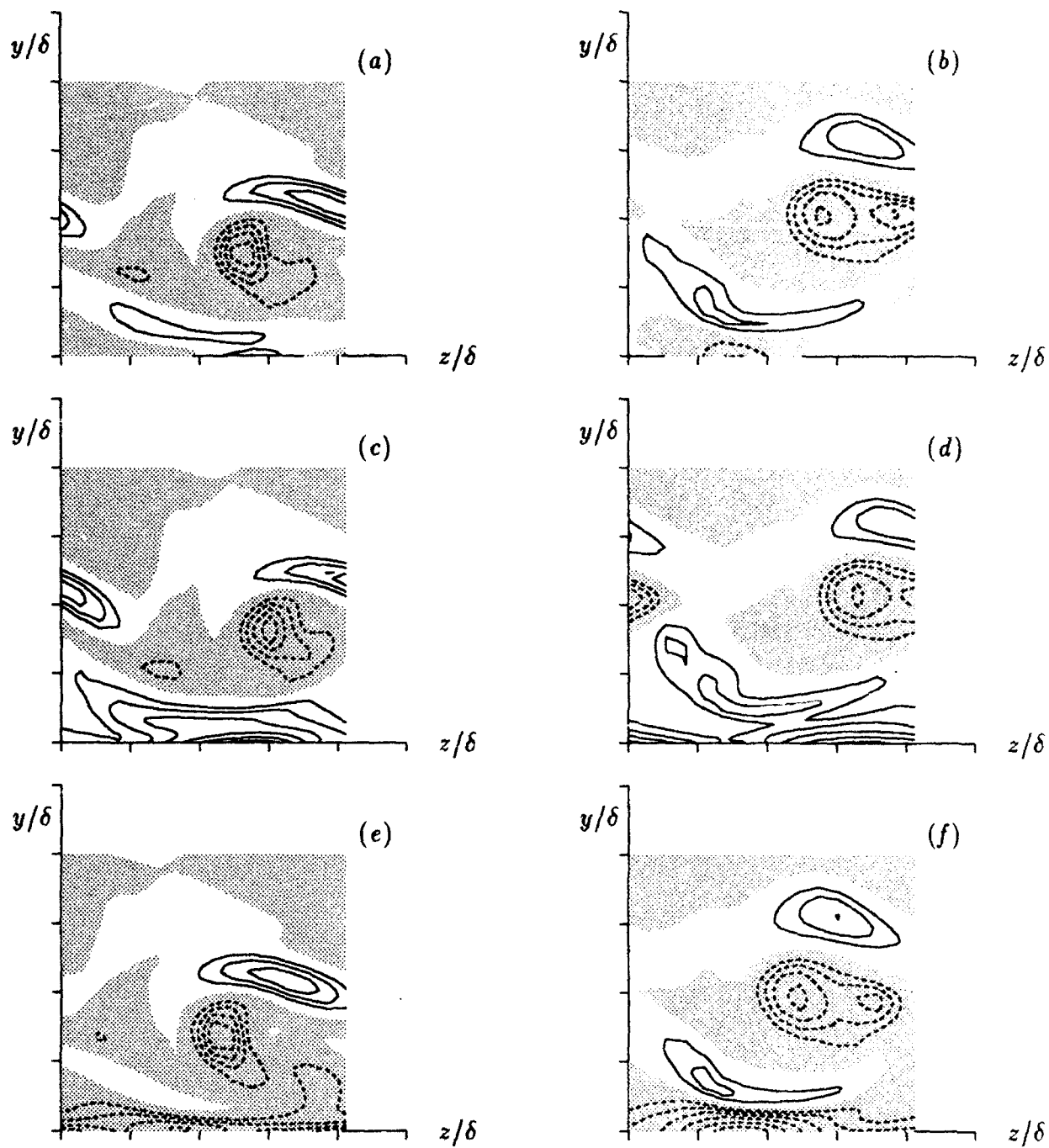


FIGURE 4.50. Formation of a vortex sheet with $\omega_x > 0$ in flow with $\Omega_x = 0$ (a, b), $\Omega_x > 0$ (c, d), $\Omega_x < 0$ (e, f). Figures to the left show plane across aft of the sheet and figures to the right show a plane across the front part of the sheet. Contour lines represents ω_x with increment 0.25 starting with 0.5 (—) and with increment -0.25 starting with -0.5 (----). Grey regions show areas with $\omega_x < 0$.

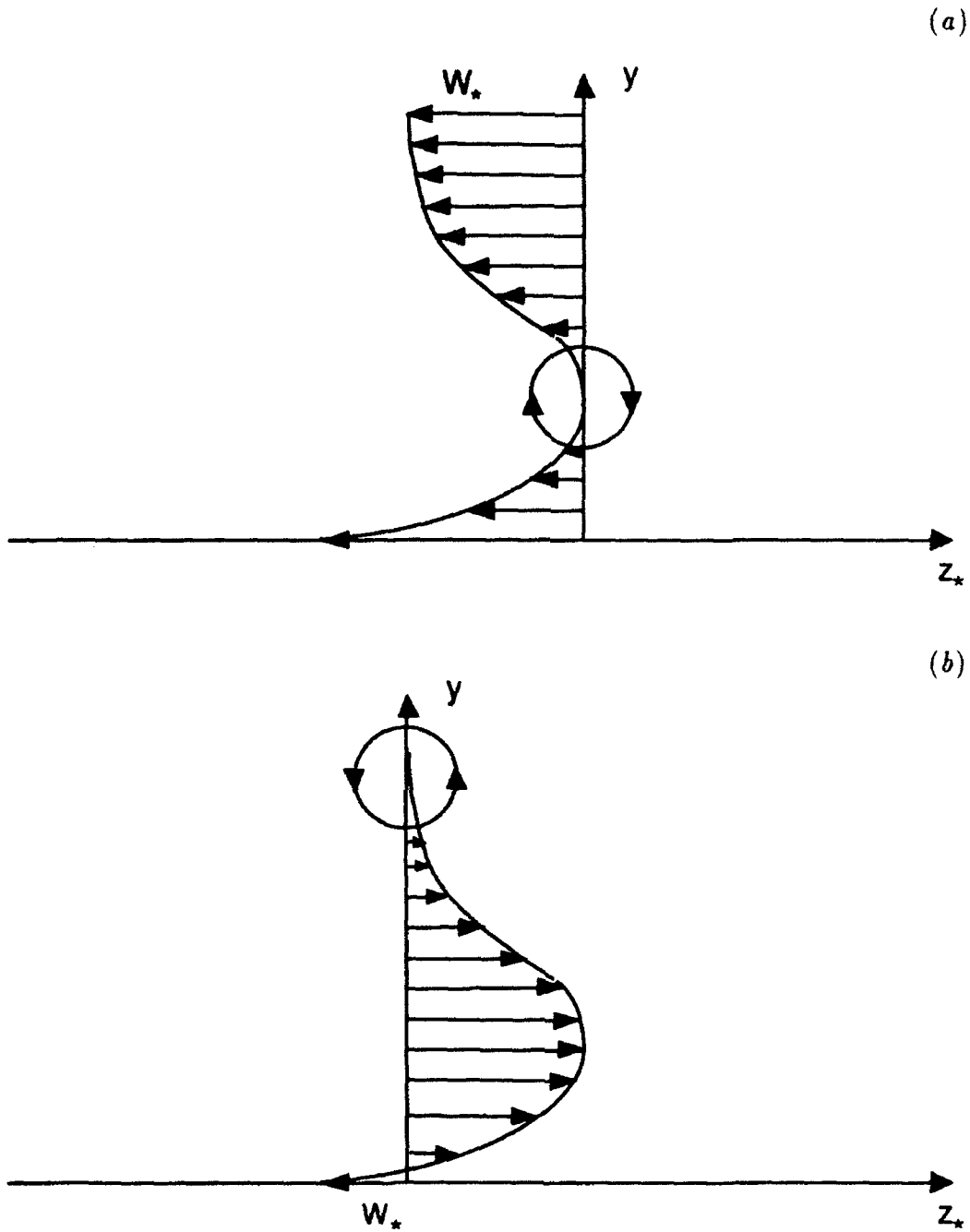


FIGURE 4.51. Schematics showing the spanwise mean velocity profile in coordinates aligned and moving with a vortex which is (a) above and (b) near the location of maximum cross-flow. Even though the profile is the same in coordinates fixed to the wall, the spanwise mean velocity below the two vortices are of opposite sign.

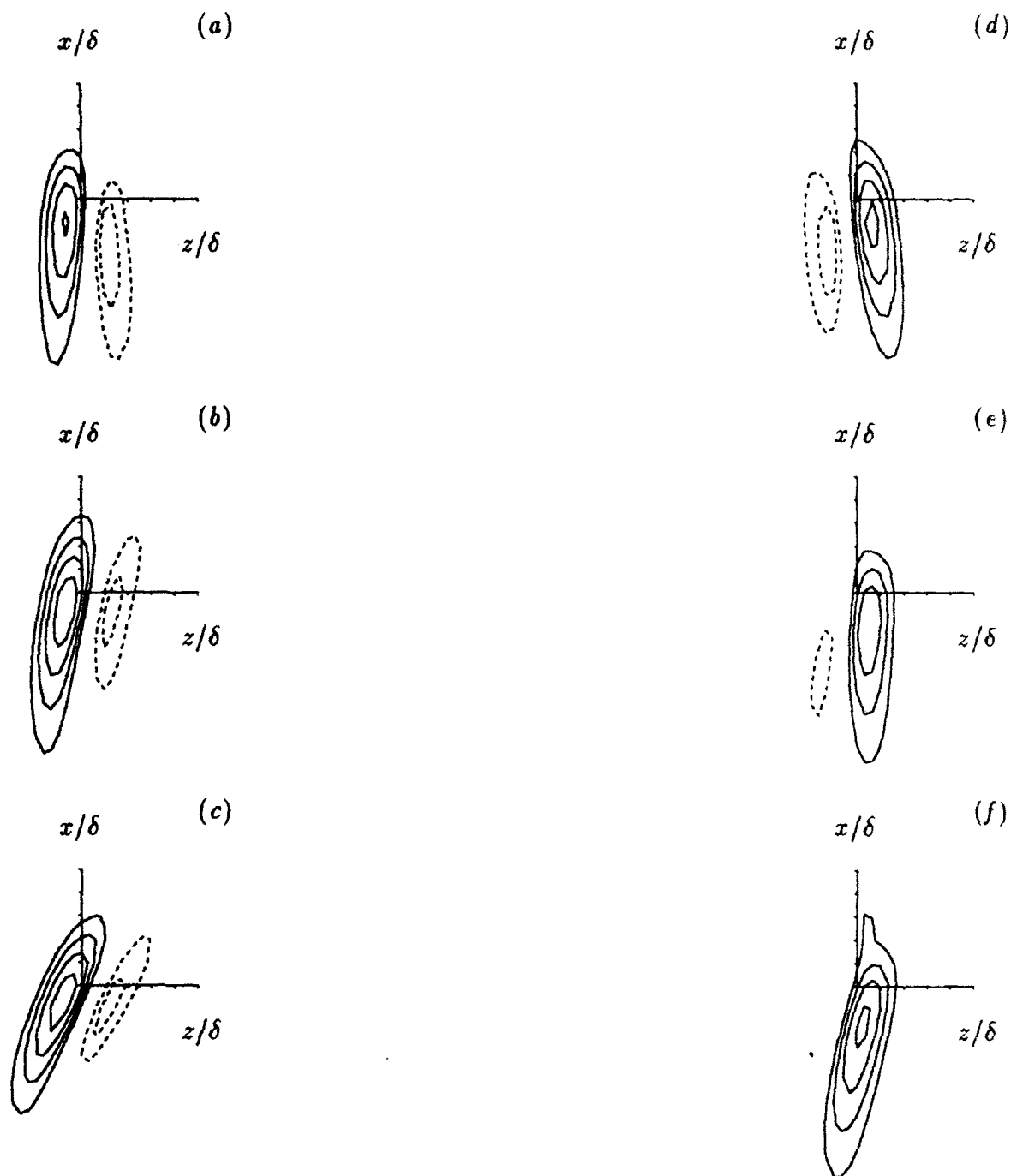


FIGURE 4.52. Top view of average field of u'_* (aligned with maximum streamwise intensity) at $y_{2D}^+ = 5$ around $\frac{\partial w'}{\partial y} > 100u_\tau/\delta$ (a, b, c) and $\frac{\partial w'}{\partial y} < 100u_\tau/\delta$ (d, e, f). $t = 0, 0.3$ and 0.6 (top to bottom). The increment is 0.5 starting with 1.5 (—) and -0.25 starting with -0.5 (----).

CHAPTER 5

CONCLUSIONS

The effect of an impulsively started transverse pressure gradient on turbulence structures in a planar channel flow was studied using direct numerical simulation. In agreement with experiments, the simulation showed a reduction in the Reynolds shear stress. It also showed a drop in the turbulent kinetic energy. To understand the underlying mechanisms for these seemingly counter-intuitive observations we focused our study on the effects of three-dimensionality on the wall layer structures. To this end we performed a detailed study of the *dynamics* of the energy producing structures in both 2D and 3D channel flows. This study included detailed examination of the instantaneous flow fields, probability density functions, two-point statistics and conditional averaged fields. The mechanisms described are consistent with all statistical data as well as observations of instantaneous fields.

In the 2D channel flow our study of the near wall structures revealed a mechanism for the generation of streamwise vortices. The cycle of events begins as follows. An inclined sheet of streamwise vorticity is generated below an existing inclined streamwise vortex through tilting of normal vorticity. The sheet is unstable and rolls up into an inclined streamwise vortex which will grow due to stretching. The key element for the stretching is the inclination of the vortex and the transport of fluid by the vortex in the wall-normal direction. The extent of streamwise vortices in the channel were rarely more than $\Delta x^+ = 350$. Near-wall streaks are generated and maintained by a string of these vortices. Low-speed streaks are longer than high-speed streaks because the magnitude of negative u' generated by a vortex is fairly independent of the distance of the vortex from the wall and hence vortices at various locations contribute to a low speed streak. On the other hand an increase in the height of a vortex above the wall tends to decrease the magnitude of positive u' it generates near the wall.

In the 3D channel the reduction in total Reynolds shear stress and turbulent kinetic energy were shown to be due to changes in the particle trajectories associated with streamwise vortices. Most affected are trajectories on the sweep-side of vortices which move fluid below them in the same direction as the spanwise mean velocity in coordinates moving with the vortex, and on the ejection-side of vortices of opposite

sign. These sweeps are weakened because the fluid moving toward the wall is convected toward the vortex-center where the vertical vortex-induced motion is low. The fluid will therefore not reach as close to the wall in 3D and hence its contribution to the Reynolds stresses is reduced. The Reynolds stresses generated by ejections due to vortices of opposite sign are reduced because the lifted fluid originates further away from the wall in 3D. In addition these ejections are reduced due to increased viscous dissipation when low-speed fluid is convected sideways above high-speed fluid. Reynolds stresses generated by other sweep and ejection motions are also reduced due to changes in particle trajectories.

Among the other observed phenomena of interest were the break-up of the wall layer streaks during the later period of three-dimensionality. This break-up was attributed to the differential turning of the streamwise vortices according to their distance from the wall and with respect to the streaks.

In summary, our numerical study of the various stages of development of a 3D flow driven by a spatially homogeneous spanwise pressure gradient has illuminated the reasons why the extra increase in the total shear rate leads to decreases in turbulent kinetic energy and total shear stress. Future work should include experimental verification of this study. In most cases experimental verification is feasible only through novel conditional averages and two-point correlations. Direct numerical simulations of a spatially developing 3D turbulent boundary layer is highly desirable. Such a computation will include inviscid skewing effects which is an important feature of many of the experimentally studied 3D flows.

REFERENCES

- ANDERSON, S. D. & EATON, J. K. 1987 An experimental investigation of pressure driven three-dimensional boundary layers. MD-49. *Stanford Univ., Dept. Mech. Eng. Thermosciences Div. Rep.*
- ANDERSON, S. D. & EATON, J. K. 1989 An experimental investigation of pressure driven three-dimensional boundary layers. *J. Fluid Mech.* **139**, 325.
- VAN DEN BERG, B. & ELSENAAR, A. 1972 Measurements in a three-dimensional incompressible turbulent boundary layer in an adverse pressure gradient under infinite swept wing conditions. *NLR TR 72092 U.*
- VAN DEN BERG, B. ELSENAAR, A., LINDHOUT, J. P. F. & WESSELING, P. 1975 Measurements in an incompressible three-dimensional turbulent boundary layer, under infinite swept wing conditions, and comparison with theory. *J. Fluid Mech.* **70**, 127.
- BISSONNETTE, L. R. & MELLOR, G. L. 1974 Experiments on the behaviour of an axisymmetric turbulent boundary layer with a sudden circumferential strain. *J. Fluid Mech.* **63**, 369.
- BLACKWELDER, R. F. & KAPLAN, R. E. 1976 On the wall structure of the turbulent boundary layer. *J. Fluid Mech.* **76**, 89.
- BRADSHAW, P. 1987 Turbulent secondary flows. *Ann. Review of Fluid Mech.* **1987**, **19**: 53.
- BRADSHAW, P. & PONTIKOS, N. S. 1985 Measurements in the turbulent boundary layer on an 'infinite' swept wing. *J. Fluid Mech.* **159**, 105.
- BRADSHAW, P. & TERRELL, M. C. 1969 The response of a turbulent boundary layer on an 'infinite' swept wing to the sudden removal of pressure gradient. *NPL Aero Report* no. 1305.
- CEBESI, T. 1984 Problems and opportunities with three-dimensional boundary layers. Presented at *AGARD Fluid Dynamics Panel discussions*, Von Karman Institute, May 1984.
- CLARK, J. A. & MARKLAND, E. 1971 Flow visualization in turbulent boundary layers. *Proc. Am. Soc. Civil Eng., J. Hydraulics Div.* **97**, 1635.

- COLEMAN, G. N., FERZIGER, J. H. & SPALART, P. R. 1990 A numerical study of the turbulent Ekman layer. *J. Fluid Mech.* **213**, 313.
- DECHOW, R. & FELSCH, K. O. 1977 Measurements of the mean velocity and of the Reynolds stress tensor in a three-dimensional turbulent boundary layer induced by a cylinder standing on a flat wall. *Proc. 1st Turbulent Shear Flows Symposium*, University Park, Pennsylvania, Apr. 18-20, 1977.
- DRIVER, D. M. & HEBBAR, S. 1989 Three-dimensional shear driven boundary layer flow with streamwise adverse pressure gradient. *AIAA J.* **27**, 1689.
- DRIVER, D. M. & JOHNSTON, J. P. 1990 Experimental study of a three-dimensional shear-driven turbulent boundary layer with streamwise adverse pressure gradient. *NASA TM 102211*.
- EATON, J. K. 1992 Turbulence structure and heat transfer in three-dimensional boundary layers. *Proceedings of the 6th symposium on energy engineering sciences* DOE Publication CONF-9105116, 262.
- ELSENAAR, A. & BOELSMA, S. H. 1974 Measurements of the Reynolds stress tensor in a three-dimensional turbulent boundary layer under infinite swept wing conditions. *NLR TR74095 U*.
- FANNELØP, T.K. & KROGSTAD, P. A. 1975 Three-dimensional turbulent boundary layers in external flows: a report on Euromech 60. *J. Fluid Mech.* **71**, 815.
- FURUYA, Y., NAKAMURA, I., YAMASHITA, S. & ISHII, T. 1977 Experiments on the relatively thick, turbulent boundary layer on a rotating cylinder in Axial flows (2nd Report, Flows under pressure gradients). *Bulletin of the Japan Society of Mech Eng.* **20**, no 140, 191.
- GOTTLIEB, D. & ORSZAG, S. A. 1977 *Numerical Analysis of Spectral Methods: Theory and Applications*. CBMS-NSF, Society for Industrial and Applied Mathematics. Philadelphia, PA, USA.
- HUNT, J. C. R., WRAY, A. A., MOIN, P. 1988 Eddies, streams, and convergence zones in turbulent flows. *Proceeding of the 1988 Summer Program*, Report CTR-S88, Stanford University.
- JIMENEZ, J. & ORLANDI, P. 1992 The rollup of a vortex layer near a wall. *CTR Manuscript 129*, Stanford University.

- JIMENEZ, J. & MOIN, P. 1990 The Minimal flow unit in near-wall turbulence. *J. Fluid Mech.* **225**, 213.
- JIMENEZ, J., MOIN, P., MOSER, R. & KEEFE, L. 1988 Ejection mechanism in the sublayer of a turbulent channel. *Phys. Fluids* **31**, 109.
- JOHANSSON, A.V., HER, J.-V. & HARITONIDIS, J. H. 1987 On the generation of high-amplitude wall-pressure peaks in turbulent boundary layers and spots. *J. Fluid Mech.* **175**, 119.
- JOHNSTON, J.P. 1970 On the three-dimensional turbulent boundary layer induced by a swept, forward-facing step. *J. Fluid Mech.* **42**, 823
- JOHNSTON J.P. 1984 Experimental Studies in three-dimensional boundary layers. Stanford Univ., Dept. Mech. Eng. Thermosciences Div. Rep. MD-34.
- KIM, J., MOIN, P. & MOSER, R. K. 1987 Turbulence statistics in fully developed channel flow at low Reynolds number. *J. Fluid Mech.* **177**, 133.
- KIM, J. & MOIN, P. 1986 The structure of the vorticity field in turbulent channel flow. Part 2. Study of ensemble-averaged fields. *J. Fluid Mech.* **162**, 339.
- LITTELL, H. S. & EATON, J. K. 1992 An experimental investigation of the three-dimensional boundary layer on a rotation disk. MD-60. *Stanford Univ., Dept. Mech. Eng. Thermosciences Div. Rep.*
- LOHMANN, R. P. 1976 The response of a developed turbulent boundary layer to local transverse surface motion. *ASME J. Fluids Eng.* **98**, 354.
- MOIN, P. 1987 Analysis of turbulence data generated by numerical simulations. *AIAA-87-0194*
- MOIN, P., SHIH, T.-H., DRIVER, D. M. & MANSOUR, N.N. 1990 Direct numerical simulation of a three-dimensional turbulent boundary layer. *Phys. Fluids* **2**, 1846.
- ROBINSON, S. K. 1991 Coherent Motions in the turbulent boundary layer. *Ann. Review of Fluid Mech.*, **23**: 601.
- SHIZAWA, T. & EATON, J. K. 1990 Interaction of an embedded longitudinal vortex with an attached, three-dimensional turbulent boundary layer. MD-56. *Stanford Univ., Dept. Mech. Eng. Thermosciences Div. Rep.*

- SIEBERS, D. L. 1983 Experimental mixed convection heat transfer from a large, vertical surface in a horizontal flow. *HMT-36, Thesis, Stanford Univ., Dept. Mech. Eng. Thermosciences Div.*
- SIMPSON, R. L. & DEVENPORT, W. J. 1990 A conceptual model for the near wall region of three-dimensional turbulent boundary layers. *Boundary-layer structure WORKSHOP* August 28-30, 1990. Langley Research Center Hampton, Virginia 23665.
- SPALART, P. R. 1989 Theoretical and numerical study of a three-dimensional turbulent boundary layer. *J. Fluid Mech.* **205**, 319.
- WALLACE, J. M., ECKELMANN, H. & BRODKEY, R.S. 1972 The wall region in turbulent shear flow. *J. Fluid Mech.* **54**, 39.
- WILLMARTH, W. W. & LU, S. S. 1972 Structure of the Reynolds stress near the wall. *J. Fluid Mech.* **55**, 65.